

TESIS DOCTORAL
ALEJANDRO GODINO MOYA

**Contributions on Groupwise
Registration for Cardiac CINE
Magnetic Resonance Reconstruction**

Directores de tesis
Dr. Marcos Martín Fernández
Dr. Carlos Alberola López

Doctorado en Tecnologías de la Información y las Telecomunicaciones
Escuela Técnica Superior de Ingenieros de Telecomunicación
Universidad de Valladolid



Universidad de Valladolid

UNIVERSIDAD DE VALLADOLID
ESCUELA TÉCNICA SUPERIOR DE INGENIEROS DE TELECOMUNICACIÓN
DEPARTAMENTO DE TEORÍA DE LA SEÑAL Y COMUNICACIÓN
E INGENIERÍA TELEMÁTICA
PROGRAMA DE DOCTORADO EN TECNOLOGÍAS DE LA INFORMACIÓN
Y LAS TELECOMUNICACIONES

TESIS DOCTORAL

CONTRIBUTIONS ON GROUPWISE
REGISTRATION FOR CARDIAC CINE
MAGNETIC RESONANCE
RECONSTRUCTION

Presentada por
Alejandro Godino Moya
para optar al grado de doctor por la Universidad de Valladolid

Dirigida por
Marcos Martín Fernández
Carlos Alberola López

JUNIO 2021

TÍTULO: Contributions on Groupwise Registration for Cardiac CINE Magnetic Resonance Reconstruction
Title:

AUTOR: Alejandro Godino Moya
Author:

DIRECTORES: Marcos Martín Fernández y Carlos Alberola López
Advisors:

DEPARTAMENTO: Teoría de la Señal y Comunicaciones e Ingeniería Telemática
Department:

TRIBUNAL / *Commitee:*

PRESIDENTE: Begoña Acha Piñero
President:

VOCAL: Alberto Gómez
Vocal:

SECRETARIO: Juan Pablo Casaseca de la Higuera
Secretary:

acuerda otorgarle la calificación de

En Valladolid, a

“It’s the questions we can’t answer that teach us the most. They teach us how to think. If you give a man an answer, all he gains is a little fact. But give him a question and he’ll look for his own answers.”

— From “The Wise Man’s Fear”
(Patrick Rothfuss, 2011)

Acknowledgements

It is difficult for me to find the right words to express all the gratitude that so many people deserve for helping me during all the exhausting process to finally get this Thesis complete.

In the first place, I would like to express my deepest gratitude to Marcos and Carlos for their unconditional dedication, for their trust placed in me and for always transmitting their optimistic point of view, even though I was not able to see it. It has been a real pleasure to work at their side. Somehow, I guess that we might be, under certain extremely odd conditions, a little bit *contentos*.

I would also like to extend my gratitude to Pablo Irrázabal and Sergio Uribe for their warm welcome in their research group at the Pontifical Catholic University of Chile and showing me other points of view for understanding research. I should give special recognition to Ronal, Katy and Hernán, as well. I am also in debt to Señora Antonia and Señor Matías for their help in finding a little bit of order within the chaos and, of course, to Vito for always being there despite of the passage of time.

Many thanks to Dr. David Filgueiras-Rama, from the Spanish National Center for Cardiovascular Research (CNIC), for his collaboration in analyzing the images.

Я хотел бы поблагодарить the people of the LPI, present and past members, for the huge amount of good moments we shared in coffee breaks, discussing and planning a better world under the watchful and silent gaze of Ivanka. I would like to especially mention the magnificent *Equipo Cardio*: without you these years would have been much harder.

그라시아스 to the people of *Drama* and *Comedia*, for making me feel one of them, despite being a complete *ifak*.

To my friends, in particular to all the inhabitants of the Kingdom of Jalem, *kirimvos* for being the light that guide me in the darkest moments. *Takk kærlega* to my favourite step-aunt Marien and my beloved *Jinetes* for their unconditional support. *Und ich sollte alle Nächte von Therapie mit Chelo —mit der Erlaubnis von Herrn Schwarz, natürlich— in Begleitung Bachs nicht vergessen. Danke schön.*

Moltes gràcies to Valentí Ponsa for helping me with the design of this book, and teaching me that there are plenty of things to do on a rainy day. I tolerate you enough.

Dzac nit vodzorsi nitru vultas lüfä? Êstájrofäté tümánwa, molté dzacä vultasuté, dzacwa nit lemviné, lex dotwaçeté-minsä nestalüshahn árgul mamdärose nit, dorusna nitsi liyää rup ôtlavurrä dotwaruté sülle ets ñasvultasjölshaté shahnuté riênwaté.

I would like to thank the Spanish Ministry of Economy and Competitiveness for their financial support through the grant BES-2015-073064.

Finally, it would not be me if I do not thank the Russians, who are marvelous people that have had political changes, and cows, who provide us nutritious breakfasts without expecting anything in return.

Resumen

La imagen por resonancia magnética (MRI) es una técnica que se utiliza para obtener, en forma de imagen, información sobre la estructura y la composición de un objeto, así como datos sobre su funcionalidad. Entre las ventajas de la MRI se encuentran sus altas reproducibilidad, precisión y versatilidad, además de que ofrece alta resolución espacial, amplio campo de visión y un buen contraste entre tejidos blandos. Sin embargo, la MRI también presenta algunas desventajas: es una técnica lenta en comparación con algunos procesos fisiológicos comunes, como el flujo sanguíneo, los latidos del corazón o la apnea, y, en consecuencia, es muy sensible al movimiento.

Una forma de acelerar las adquisiciones de MRI consiste en adquirir solo una porción del espacio k (submuestreo) y aplicar después técnicas avanzadas de procesamiento de imagen para su reconstrucción. Sin embargo, el problema de reconstrucción resultante deriva en un sistema indeterminado y mal condicionado. Por esta razón, se suele incorporar en el modelo de imagen cierta información, restricciones y asunciones conocidas a priori para definir una función de coste, cuya optimización proporciona una solución regularizada a dicho problema.

Esta Tesis aborda el problema computacionalmente exigente de la reconstrucción dinámica de MRI a partir de datos altamente submuestreados. El movimiento presente en la secuencia dinámica de MRI se utiliza como fuente de información adicional para aprovechar convenientemente la redundancia que existe tanto en las dimensiones espaciales como en la temporal.

Por un lado, en esta Tesis se exploran términos de regularización espacialmente variantes que tienen en cuenta la cantidad de movimiento presente

en la imagen para ponderar pixel a pixel la cantidad de regularización que se necesita.

Por otro lado, se propone la técnica denominada como *elastic aligned-SENSE* (EAS), con la que se obtiene, como resultado del proceso de optimización propuesto, una imagen patrón libre de movimiento, junto con una serie de deformaciones no rígidas. Estas deformaciones se aplican sobre la imagen patrón hasta alcanzar cada uno de los estados del ciclo cardiaco que conforman la secuencia CINE completa. En términos de carga computacional, los resultados obtenidos muestran que este método es menos exigente que otros que utilizan muestreo compresivo (*compressed sensing*) y utilizan el movimiento para favorecer la representación de las imágenes con un número reducido de coeficientes (*sparsity*). Sin embargo, en ocasiones con EAS se pierde el movimiento en algunas áreas de la imagen. Esto se debe a que este método es altamente dependiente del modelo de imagen empleado y, en este tipo de metodologías, el rendimiento es satisfactorio en tanto en cuanto el modelo de imagen utilizado describe con precisión el movimiento que se está tratando. De hecho, el movimiento fuera del plano de observación de la imagen (*through-plane*) hace que el movimiento estimado por EAS no represente de forma precisa las deformaciones reales que sufre el corazón y, por tanto, la calidad de las reconstrucciones se ve afectada. Por esta razón, la extensión al caso 3D, donde el movimiento fuera de plano no existe, parece la línea futura de investigación más natural.

La reducción en el coste computacional de la solución EAS, así como en los tiempos de ejecución hacen que ésta sea especialmente adecuada como etapa inicializadora para otros métodos que utilizan muestreo compresivo y hacen uso del movimiento para obtener una regularización inteligente. En este nuevo escenario, el movimiento no es ya un elemento tan crítico como cuando se utiliza el modelo directo —como en el caso de EAS—, sino que EAS proporciona a estos otros métodos una estimación de movimiento inicial más conveniente y con una carga computacional más asequible. De ahí que se mantenga la calidad de las reconstrucciones finales, mientras

que el tiempo de ejecución total se reduce considerablemente.

Adicionalmente, se ha propuesto una metodología basada en validación cruzada para establecer el valor de los parámetros de regularización, junto con una generalización de un esquema de muestreo 3D con ordenamiento en espiral según el ángulo áureo. Este esquema de muestreo permite seleccionar, por medio de un determinado parámetro α , desde un patrón de muestreo uniforme del espacio k hasta un esquema de muestreo más denso en el centro. Los experimentos realizados han demostrado que las configuraciones con $\alpha \approx 1$ son preferibles, pero en presencia de altos niveles de ruido, las configuraciones intermedias con $\alpha \approx 0.7$ proporcionan mejores resultados.

Abstract

Magnetic Resonance Imaging (MRI) is a technique used to obtain, in the form of a picture, information about structure, composition and even functionality of an object. It is characterized by its high reproducibility, accuracy and versatility, and it offers high spatial resolution, wide field-of-view and good contrast between soft tissues. However, MRI presents some disadvantages: it is slow compared to common physiological processes such as blood flow, heartbeat or breath hold and, in addition, it is very sensitive to motion.

A common approach to accelerate MRI acquisitions is to collect only a portion of k-space (subsampling) and to apply advanced image processing techniques for image reconstruction. Nevertheless, the problem to be solved becomes undetermined and ill-conditioned. Thus, some knowledge, constraints and assumptions are added to the information of the image model to define a cost function, the optimization of which provides a regularized solution.

This Thesis deals with the computationally demanding problem of dynamic MRI reconstruction from highly undersampled data. The motion present in the dynamic sequence is used as a complementary source of knowledge to exploit conveniently the redundancies existing in both temporal and spatial dimensions.

On one hand, this Thesis explores spatially varying regularization terms that take into account motion to weight pixelwise the amount of regularization needed.

On the other hand, we have proposed what we call the elastic aligned-SENSE (EAS) solution, in which a motion-free pattern image, together with a set of nonrigid deformations, are the results of our optimization.

The pattern image is deformed to the corresponding phase of the cardiac cycle to build the CINE sequence. In terms of computational needs, our results are less demanding than other methods that make use of motion to foster sparsity. However, occasionally motion is lost in some areas of the image. This is due to the fact that the method is model-based and in such methodologies performance is satisfactory as long as the model describes accurately the motion that is being dealt with. In fact, through-plane movement makes estimated motion not represent the real deformations that the heart undergoes and thus quality of reconstructions is compromised. Therefore, the extension to 3D seems a natural future line of research.

EAS computational performance makes it specially suitable as a fast initializer for other data-driven motion-compensated compressed sensing methods that make use of motion for smart regularization. This makes motion not as critical as when it is used in the image forward model—as it is the case of EAS—but EAS does provide those methods with a convenient initial motion estimation with affordable computational load. Hence, in this new scenario, the quality of final reconstructions is maintained while execution time is considerably reduced.

Additionally, a methodology based on cross validation to establish the value of the regularization parameters has been proposed, together with a generalization of a 3D sampling scheme with spiral golden angle ordering. This sampling scheme allows the practitioner to select, by means of a certain parameter α , from a uniform sampling pattern of k-space to a denser sampling scheme in its center. The conducted experiments have shown that configurations with $\alpha \approx 1$ are preferable, but in presence of high levels of noise, intermediate configurations with $\alpha \approx 0.7$ draw better results.

Contents

Acknowledgements	vii
Resumen	ix
Abstract	xiii
Contents	xv
List of Acronyms	xix
List of Figures	xxv
List of Tables	xxviii
1 Introduction	1
1.1 Motivation	1
1.2 Objectives	5
1.3 Methodology	6
1.4 Publications	7
2 Background	11
2.1 Nuclear Magnetic Resonance	11
2.2 Signal localization	15
2.2.1 k-Space sampling	17
2.3 Image reconstruction	20
2.3.1 Parallel Imaging	21
2.3.2 SENSE	22
2.3.3 Compressed Sensing	24
2.3.4 k-t SPARSE-SENSE	25

2.3.5	Groupwise motion compensated compressed sensing	27
2.3.5.1	Motion Estimation	29
2.3.5.2	B-Spline Free Form Deformation model . .	30
2.3.5.2.1	Forward model	31
2.3.5.2.2	Backward model: inversion	32
2.3.5.2.3	Composition	33
2.3.6	Other image reconstruction methods	34
2.3.6.1	Methods with PI and CS	34
2.3.6.2	Methods with motion estimation and mo- tion compensation	35
2.3.6.3	Methods with low-rank decomposition . . .	37
2.3.6.4	Methods with manifold learning	38
2.3.6.5	Methods with FB acquisitions	39
2.3.6.6	Methods with Deep Learning	40
2.3.6.7	Conclusion	42
3	Methods	43
3.1	Space-time variant weighted regularization	43
3.1.1	Weighting matrix	45
3.1.1.1	Plateau regularization	45
3.1.1.2	Motion weighted regularization	46
3.2	Elastic alignedSENSE	48
3.2.1	Regularization terms in elastic alignedSENSE	52
3.2.1.1	Fixed regularization terms in elastic aligned- SENSE	52
3.2.1.2	Variant regularization terms in elastic aligned- SENSE	54
3.2.2	Combination of elastic alignedSENSE and groupwise motion-compensated compressed sensing	54
3.2.3	Radial extension of elastic alignedSENSE	55
3.3	Experiments	56

3.3.1	Space-time variant weighted regularization	56
3.3.1.1	2D experiments	58
3.3.1.2	3D experiments	59
3.3.2	Elastic alignedSENSE	59
3.3.2.1	Fixed regularization terms	59
3.3.2.2	Variant regularization terms	62
3.3.2.3	Combination of elastic alignedSENSE and groupwise motion-compensated compressed sensing	63
3.3.2.4	Radial extension of elastic alignedSENSE	64
4	Results	67
4.1	Space-time variant weighted regularization	67
4.1.1	2D Results	67
4.1.2	3D Results	71
4.2	Elastic alignedSENSE	78
4.2.1	Fixed regularization terms	78
4.2.2	Variant regularization terms	80
4.2.3	Combination of elastic alignedSENSE and groupwise motion-compensated compressed sensing	94
4.2.4	Radial extension of elastic alignedSENSE	99
5	Conclusions and future work	103
5.1	Conclusion	103
5.2	Contributions	104
5.3	Future work	106
A	Generalized 3D Cartesian sampling scheme with spiral golden angle ordering	109
A.1	Introduction	109
A.2	Description of the sampling scheme	110

B	Regularization parameter selection	113
B.1	Introduction	113
B.2	Description of the procedure	114
C	Gradient calculation of the cost function for elastic aligned-SENSE	119
C.1	Introduction	119
C.2	Calculation	120
D	Recovering a cardiac synchronism signal from k-space data in cardiac CINE MRI	123
D.1	Introduction	123
D.2	Theory	124
D.2.1	Coil selection	125
D.3	Materials and Methods	125
D.3.1	Cartesian, breath-hold acquisition	125
D.3.2	Golden-radial breath-hold acquisition	126
D.3.3	Golden-radial free breathing acquisition	126
D.4	Results	127
D.5	Discussion	130

List of Acronyms

ACS	Autocalibration signal region
ADMM	Alternating direction method of multipliers
AF	Acceleration factor
BH	Breath hold
BLAST	Broad-use linear acquisition speed-up technique
bSSFP	Balanced steady state free precession
bTFE	Balanced turbo field echo
CASPR-Tiger	Cartesian trajectory with spiral profile ordering and tiny golden angle step for eddy current reduction
CG	Conjugate gradient
CNIC	Spanish National Center for Cardiovascular Research
CNN	Convolutional neural network
CPU	Central processing unit
CRNN	Convolutional recurrent neural network
CS	Compressed sensing
CT	Computed tomography
DAGAN	Deep de-aliasing generative adversarial network
DICOM	Digital imaging and communication on medicine
DL	Deep Learning
DSP	Digital signal processor
DTF	Double tight frame
EAS	Elastic alignedSENSE
ECG	Electrocardiogram
EDV	End diastolic volume
EF	Ejection fraction
EPI	Echo-Planar Imaging

ESV	End systolic volume
FB	Free breathing
FFD	Free form deformation
FFT	Fast Fourier transform
FOCUSS	Focal underdetermined system solver
FOV	Field of view
FPGA	Field-programmable gate array
FT	Fourier transform
G-CASPR	Golden angle Cartesian acquisition with spiral profile ordering
GPU	Graphics processing unit
gpuNUFFT	Non uniform fast Fourier transform for graphics processing unit
GRAPPA	Generalized autocalibrating partially parallel acquisitions
GW	Groupwise
GWCS	Groupwise motion compensated compressed sensing
HFSE	High frequency signal-to-error ratio
iGRASP	Iterative golden-angle radial sparse parallel MRI
kt-SS	k-t SPARSE-SENSE
LDMM	Low-dimensional manifold model
LoG	Laplacian of Gaussian filter
LPI	Image Processing Lab (Valladolid, Spain)
L+S	low-rank and sparse component
MALLRT	Motion aligned locally low rank tensor
MASTeR	Motion-adaptive spatio-temporal
MC	Motion compensation
ME	Motion estimation
MIX	Combination of elastic alignedSENSE and groupwise motion compensated compressed sensing
ML	Manifold learning

MoDL	Model-based deep learning
MRI	Magnetic resonance imaging
NCC	Normalized crossed correlation
NESTA	Nesterov's algorithm
NUFFT	Non uniform fast Fourier transform
PCA	Principal component analysis
PET	Positron emission tomography
PI	Parallel imaging
PPG	Pulse photoplethysmography
PPU	Peripheral pulse unit
<i>R</i>	Reduction factor
RF	Radiofrequency
RIP	Restricted isometry property
RKHS	Reproducing kernel Hilbert spaces
RMSE	Root mean square error
ROCK	Rotating Cartesian k-space
ROI	Region of interest
RPCA	Robust principal component analysis
SENSE	Sensitivity encoding
SER	Signal-to-error ratio
SNR	Signal-to-noise ratio
sPICS	Simple parallel imaging compressed sensing
spTV	Spatial total variation
SSIM	Structural similarity index
SToRM	Smoothnes regularization on manifolds
SV	Stroke volume
TE	Echo time
TR	Repetition time
tTV	Temporal total variation
UNFOLD	Unaliasing by Fourier-encoding the overlaps in the temporal dimension

VDRad	Variable-density sampling and radial view ordering
VM	Virtual machine
XCAT	Extended cardiac-torso anatomical phantom software
XD-GRASP	Extra-dimensional golden-angle radial sparse parallel MRI

List of Figures

1.1	Graphical outline of the contributions of the Thesis.	9
2.1	Nuclear magnetic moment vectors.	12
2.2	Displacement of the net magnetization after the application of a RF pulse.	13
2.3	Magnetic resonance relaxation.	15
2.4	Different trajectories for k-space subsampling.	19
2.5	Parallel imaging scheme.	22
2.6	Relation between area changes and the Jacobian of the transformations	28
2.7	Design of the control point grid for FFD B-Spline transfor- mations	33
3.1	Effect of the regularization parameter in the reconstructed images.	44
3.2	Space-time variant weighting matrices.	46
3.3	Space-time variant regularization reconstruction model.	47
3.4	Scheme of the elastic alignedSENSE reconstruction.	50
3.5	Scheme of spatial transformations in GWCS and EAS.	51
3.6	Scheme of the MIX reconstruction method.	55
3.7	Scheme of the registration methods performed for motion quality assessment.	60
3.8	NCC between temporal profiles.	61
3.9	Example of landmarks for motion assessment.	63
4.1	SER and HFSER values for 2D datasets.	68
4.2	Bland-Altman plots for ejection fraction.	69

4.3	Normalized error images in 2D reconstructions.	70
4.4	SER and HFSER values for 3D datasets, $R = 5$ and $SNR = 18$	72
4.5	SER and HFSER values for 3D datasets, $R = 20$ and $SNR = 18$	73
4.6	SER and HFSER values for 3D datasets, $R = 20$ and $SNR = 18$	76
4.7	Normalized error images in 3D reconstructions.	77
4.8	Results on real data, using 2D Cartesian pseudorandom undersampling.	79
4.9	Results for EAS reconstructions with four different regularization operators for the EAS image sub-problem.	81
4.10	EAS reconstructions.	84
4.11	Results for EAS reconstructions with both fixed and variant regularization terms.	85
4.12	Comparison of EAS reconstructions with other methods from the literature, part 1.	89
4.13	Comparison of EAS reconstructions with other methods from the literature, part 2.	90
4.14	EAS compared to other methods from the literature (HFSER, SSIM, NCC).	91
4.15	EAS compared to other methods from the literature (RMSE, Landmarks RMSE, time).	92
4.16	Example of the questionnaire for subjective image quality assessment.	95
4.17	Comparison of MIX methods with GWCS and EAS.	97
4.18	MIX compared with EAS and GWCS (HFSER, SSIM, NCC).	98
4.19	MIX compared to EAS and GWCS (RMSE, time).	99
4.20	Comparison of EAS radial with iGRASP, GWGS and MIX methods.	100

A.1	Generalized 3D Cartesian sampling scheme with spiral golden-angle ordering.	110
B.1	Regularization parameter selection: division of datasets. . .	114
B.2	Regularization parameter selection: pre-training phase. . . .	115
B.3	Regularization parameter selection: training phase.	116
B.4	Regularization parameter selection: test phase.	117
D.1	Relation of cardiac motion with average image intensity. . .	124
D.2	Coil selection for recovering cardiac synchronism signal. . .	126
D.3	Cardiac synchronism signal for Cartesian real data.	128
D.4	Cardiac synchronism signal for golden-radial real data. . . .	129

List of Tables

4.1	EF values calculated in 2D reconstructions using space-time variant weighted regularization strategies	70
4.2	p-Values of SER distributions of 3D reconstructions using space-time variant weighted regularization strategies.	74
4.3	p-Values of HFSER distributions of 3D reconstructions using space-time variant weighted regularization strategies.	74
4.4	p-Values for the Mann-Whitney test on samples of HFSER for reconstructions using EAS with different regularization operators for the EAS image sub-problem.	82
4.5	p-Values of the Mann-Whitney test on samples of RMSE for reconstructions using EAS with different regularization operators for the EAS image sub-problem.	82
4.6	p-Values of the Mann-Whitney test on samples of average running times for reconstructing one slice using EAS with the different regularization operators for the EAS image sub-problem.	83
4.7	p-Values of the Mann-Whitney test on samples of HFSER for EAS with both fixed and variant regularization terms.	84
4.8	p-Values of the Mann-Whitney test on samples of RMSE for EAS with both fixed and variant regularization terms.	86
4.9	p-Values of the Mann-Whitney test on samples of execution times for reconstructing one slice using EAS with the different regularization operators for the EAS image sub-problem.	87
4.10	Mean value \pm standard deviation of the scores given by the expert for each reconstruction method.	94

4.11 Mean values of execution times for reconstructing one slice using radial trajectories.	101
D.1 Error comparison between the different methods for recov- ering the cardiac synchronism signal.	130

Chapter 1

INTRODUCTION

1.1 Motivation

Magnetic Resonance Imaging (MRI) is a technique used to obtain, in form of an image, information about the structure, composition and even functionality of an object. This technique is based in the phenomenon of nuclear magnetic resonance, described in the mid-20th century by Bloch [1], but it was not included in the clinical routine until some decades later [2].

As opposed to other imaging techniques such as Computed Tomography (CT) and Positron Emission Tomography (PET), MRI does not make use of ionizing energy, but of electromagnetic radiation, a fact that makes it an innocuous technique, since this kind of radiation does not affect the molecular structure of the object being examined. In addition, MRI is characterized by its high reproducibility, accuracy and versatility [3] and offers high spatial resolution, wide Field-of-View (FOV) and good contrast between soft tissues [4, 5]. All these characteristics have led MRI to progressively acquire more importance within the clinical routine, to the point that it has become one of the most used radiological techniques nowadays [6, 7] and, specifically, in the field of cardiology, it is considered the gold standard procedure to assess cardiac function and anatomy [8].

However, MRI presents some disadvantages. An MRI scan takes long

compared to common physiological processes such as blood flow, heartbeat or breath hold (BH). In addition, it is relatively expensive and requires well-trained staff, long examination times and elaborated setups, due to the complex underlying physical phenomena [3]. Furthermore, the main source of artifacts and image quality degradation of this technique is due to its high sensitivity to motion, showing up adverse effects in the images, like blurring or ghosting, among others [9].

In the field of cardiology the cardiac CINE MRI modality is commonly used. This modality consists of different images of the heart throughout the cardiac cycle, so that a dynamic sequence is created in which both anatomical structure and movement can be observed as a function of time, as if it were a movie. This is quite challenging, as stated before, since cardiac CINE MRI is affected by motion, in particular, the movement introduced by the heart itself and the movement induced by the patient's breathing.

In order to obtain this kind of images, the cardiac cycle is divided into different phases of short duration (typically ≈ 30 ms) to minimize heart motion effects. Since cardiac movement is quasi-periodic, data can be acquired along several cardiac cycles to complete k-space for each phase. For this reason, synchronism is needed, which is achieved by means of external devices like electrocardiogram (ECG) or pulse photoplethysmography (PPG) (gated approaches), or by estimating such synchronism signals from the acquired data themselves (self-gating approaches). The synchronism can be made prospectively or retrospectively. In the first case, taking the R-wave from the ECG signal as a temporal reference, k-space samples are collected during 80-90% of the RR interval —the time between two consecutive R-waves— and the procedure makes use of as many cycles as needed to complete the k-space. The main drawback of this technique is that there are some instants of the cardiac cycle that are not represented. In the second case, k-space samples are collected continuously and a timestamp label is assigned to each of them, so that synchronism can be made

at reconstruction time using the ECG signal as a reference.

As far as breathing is concerned, both the diaphragm and the thoracic cage make the heart move fairly rigidly along the longitudinal axis. Movement induced by respiration is different in inspiration and expiration stages as a result of lung hysteresis. However, breath-induced motion is usually considered periodic and the relationship between the displacement of the diaphragm and heart motion is approximately linear [9, 10]. The simplest solutions to overcome the adverse effects derived from respiratory motion perform acquisitions in apnea or by means of navigators, such as chest belts with pressure sensors. Both alternatives reduce the efficiency of the acquisition process, as data are not acquired during a long part of the total time needed to perform a complete study. For example, several rest periods between apneas are needed for the patient to recover or data are only acquired in a specific time window (usually end expiration). Moreover, apnea is not always possible, especially with non-cooperative patients, such as children or those with a respiratory pathology that prevents them to carry out long apneas, and also misalignment can occur due to the difficulty of having equal apnea states. For this reason, free breathing (FB) approaches in which respiratory motion is estimated and compensated have gained a great interest.

A common approach in FB acquisitions consists in dividing the data into different cardiac and respiratory states (*bins*) depending on the breathing position and cardiac phase at which they were acquired. An image for each bin can be then reconstructed. One of the drawbacks of this double binning technique is that there are less data available for each image to be reconstructed, due to the additional breathing states. Furthermore, the fact of having less data makes the problem worse posed, so that stability might be at stake and hence further processing demands, additional computational needs and higher time consumption may arise. In addition, the diagnostic potential of the additional images may be objectionable. Motion compensation has also been included in a similar reconstruction

pipeline to improve final image quality [11].

Performing acquisitions either in multiple apneas or in FB can result in remarkably long scans, due to temporal inefficiencies in the acquisition process, as stated above. One way to reduce scan times is to acquire only a portion of the k-space (*subsampling*) and to apply later on some advanced image post-processing techniques. The relationship between the total number of samples of the fully sampled k-space and the actual number of acquired samples is known as *acceleration factor* (AF) or *reduction factor*, R . However, subsampling k-space implies *aliasing* in the image domain, which manifest itself as superimposed replicas of the scanned object. Moreover, the reconstruction problem becomes undetermined, due to the missing samples, and ill-conditioned, due to noisy measurements. The problem can be solved as a least square problem, but this method is very sensitive to any data perturbation (for example, noisy measurements). Therefore, some knowledge, constraints and assumptions (regularization terms) may be integrated into the image model to obtain the desired solution.

This Thesis deals with the highly computational demanding problem of dynamic magnetic resonance image reconstruction from largely under-sampled data. In particular, cardiac CINE MRI in both 2D and 3D are considered. To face this problem, the Thesis focuses on the use of motion present in the dynamic sequence as a complementary source of knowledge to be included in the image model. This knowledge is incorporated in two main different ways.

On one hand, artifacts as well as noise amplification may arise during the reconstruction process, due to high subsampling of k-space. Therefore, regularization is included, but this may make the problem even more computationally expensive. Besides, selecting an adequate regularization parameter is crucial: a high value of the regularization parameter gives rise to static sequences with less artifacts, whereas a low value of the regularization parameter results in moving sequences with more artifacts.

This Thesis aims, as one major objective, to explore spatially varying regularization terms that take into account the motion present in the image to weight pixelwise the amount of regularization needed. This may allow a tradeoff between the two previous cases —recovering static sequences with less artifacts and moving sequences with more artifacts due to incorrect regularization parameter selection— to be reached, resulting in higher quality images.

On the other hand, an image needs a relatively high number of parameters to describe itself. Furthermore, a CINE sequence is redundant not only in the spatial dimensions, but also in the temporal one. These features can be exploited, so that a CINE sequence can be interpreted as a free-motion pattern image that is deformed by a set of transformations, which take that pattern image to the corresponding cardiac state. Since transformations need less parameters to be described, the reconstruction problem will be better posed, so higher AF seems achievable and the reconstruction problem should be less computationally demanding. However, this solution would be model-based, so its quality will depend on the precision of the model. Exploring these ideas as a reconstruction methodology is the second major objective of this Thesis.

1.2 Objectives

The main objective of this Thesis is to propose and design a framework for dynamic MRI reconstruction from highly undersampled data that takes the motion information present in the dynamic sequence as complementary source of knowledge, so that computational needs can be reduced without losing image quality.

This main objective can be divided into the following sub-objectives:

- To define a strategy to leverage the regularization parameter, that takes into account the particular properties of the different regions of the image.

- To propose an image model consisting of a free-motion pattern image plus a set of transformations that deform the pattern image to the corresponding cardiac cycle.

Additionally, and as a consequence of the two previous sub-objectives, two secondary objectives appears:

- To define a method for selecting the value of regularization parameters, so that image quality is maximized, not only in terms of intensity, but also in terms of motion preservation.
- To define a variable 3D Cartesian sampling scheme with Golden-angle ordering and determine the conditions under which the image quality is maximized in cardiac CINE MRI applications.

1.3 Methodology

Along the work of this Thesis, comparisons and validations of the proposed framework with respect to related Compressed Sensing (CS) reconstruction methods, with special attention to those that apply motion estimation (ME) and motion compensation (MC), have been carried out. To this end, several datasets have been used, when applicable:

1. Synthetic datasets using the extended Cardiac-Torso anatomical phantom software (XCAT) [12, 13]. In this scenario both the exact image to reconstruct and the motion are known beforehand. Thus, it is possible to evaluate the performance of the proposed methods both in ideal conditions as well as when several sources of degradation are introduced, for different AF. However, it is important to notice that synthetically generated functions are in general simpler than images from real acquisitions.

2. Simulated acquisitions from DICOM images. k-space can be obtained by applying the Fourier transform (FT) to the images and the resulting k-space can be subsampled without constraints. This allows us to test the algorithms in a more realistic scenario, although the original phase information is lost.
3. Acquisitions on sedated swine, kindly provided by the Spanish National Center for Cardiovascular Research (CNIC). The anatomy of a swine is similar to the human being. However, respiratory motion is barely appreciated, due to the physiology of these animals. Nevertheless, synthetically spatio-temporal deformations can be added, if needed, to simulate different respiration positions, so that algorithms can be tested in a more realistic situation, but knowing the exact respiratory motion beforehand.
4. True raw data coming from fully sampled Cartesian acquisitions from the scanner of the Universidad de Valladolid, which the research group has access to, and from King's College London acquisitions, to which our research group has access thanks to past collaborations. This allows us to validate the proposed methods in a more realistic scenario. Data can be retrospectively undersampled to simulate different AF.
5. True raw data using Golden-radial subsampling in single BH acquisitions performed at King's College London. In this case, data are collected continuously and different AF can be obtained by setting the acquisition time or the time resolution window, when applicable.

1.4 Publications

In the course of this Thesis, the following contributions have been produced (Figure 1.1):

- Indexed international journals:
 - Godino-Moya, A., Royuela-del-Val, J., Usman, M., Menchón-Lara, R.M., Martín-Fernández, M., Prieto, C., Alberola-López, C. (2019). Space-time variant weighted regularization in compressed sensing cardiac CINE MRI. *Magnetic Resonance Imaging*. 58:44-55.
 - Godino-Moya, A., Menchón-Lara, R.M., Martín-Fernández, M., Prieto, C., Alberola-López, C. (2021). Elastic alignedSENSE for dynamic MR reconstruction. A proof of concept in cardiac CINE. *Entropy*. 23(5):555.
- Conference presentations:
 - Godino-Moya, A., Cloquell T., Royuela-del-Val, J., Martín-Fernández, M., Alberola-López, C. (2017). Avoiding additional hardware and recovering cardiac information from k-space. In *Proceedings of the 35th Annual Congress of the Spanish Society of Biomedical Engineering (CASEIB 2017)*, pp:45-48, Bilbao, Spain. The work that served as basis for this communication has been included in Appendix D.
 - Godino-Moya, A., Royuela-del-Val, J., Menchón-Lara, R.M., Martín-Fernández, M., Alberola-López, C. (2017). G-CASPR and VDRad: extreme cases of a continuum. Intermediate may be better. In *Proceedings of the 34th European Society for Magnetic Resonance in Medicine and Biology Scientific Meeting (ESMRMB 2017)*, Barcelona, Spain, 30(1):96-78.
 - Royuela-del-Val, J., Godino-Moya, A., Menchón-Lara, R.M., Martín-Fernández, M., Alberola-López, C. (2017). Space-time variant weighted regularization improves motion reconstruction in compressed sensing accelerated cardiac CINE MRI. In *Proceedings of the 34th European Society for Magnetic Resonance*

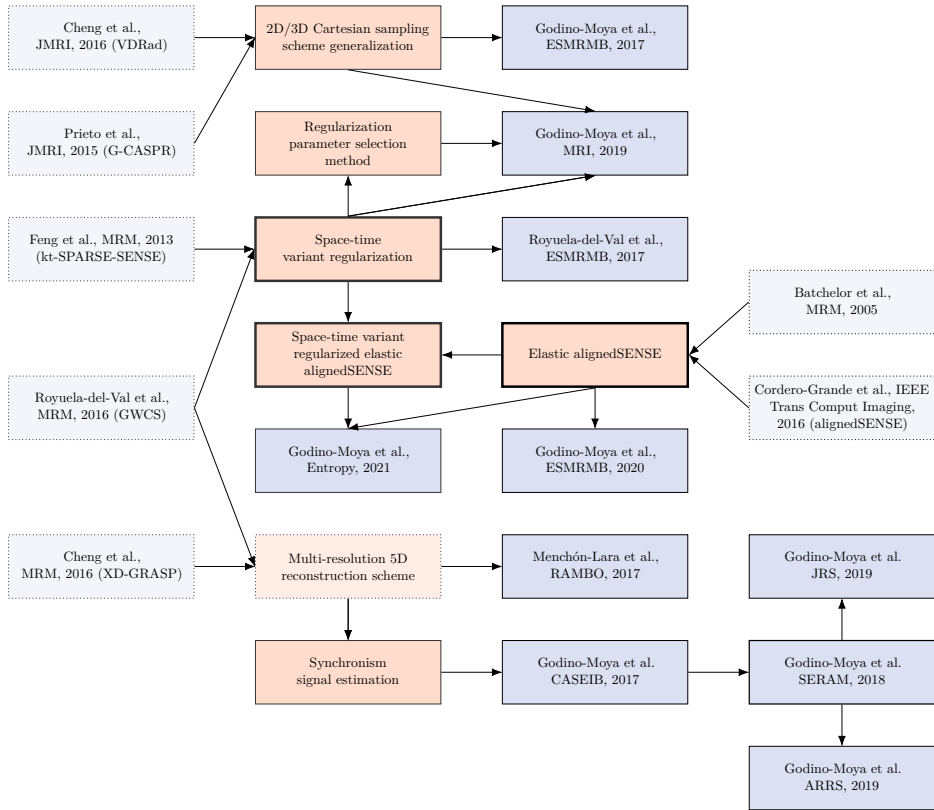


Figure 1.1: Graphical outline of the contributions (orange) and publications (blue) of this Thesis. The main contributions are represented with darker boxes. Some relevant contributions and publications from other authors that inspired or served as an important basis for this work are included and represented with dashed outlined boxes.

in Medicine and Biology Scientific Meeting (ESMRMB 2017),
Barcelona, Spain, 30(1):96-78

- Menchón-Lara, R.M., Royuela-del-Val, J., Godino-Moya, A., Cordero-Grande, L., Simmross-Wattenberg, F., Martín-Fernández, M., Alberola-López, C. (2017). An Efficient Multi-resolution Reconstruction Scheme with Motion Compensation for 5D Free-Breathing Whole-Heart MRI. In: Cardoso M. et al.

- (eds) *Molecular Imaging, Reconstruction and Analysis of Moving Body Organs, and Stroke Imaging and Treatment*. RAMBO 2017, CMMI 2017, SWITCH 2017. *Lecture Notes in Computer Science*, vol 10555. Springer, Cham.
- Godino-Moya, A., Cloquell, T., Royuela-del-Val, J., Martín-Fernández, M., Alberola-López, C. (2018). Obtención de la señal de sincronismo cardiaco a partir de los datos del k-espacio en IRM CINE cardiaca. *34th Congress of the Spanish Society of Medical Radiology (SERAM 2018)*, Pamplona, Spain. The **Magna Cum Laude Award** in Biotechnology was received for this communication.
 - Electronic posters:
 - Godino-Moya, A., Cloquell, T., Royuela-del-Val, J., Martín-Fernández, M., Alberola-López, C. (2019). Recovering cardiac synchronism signal from k-space data in cardiac CINE MRI. *78th Annual Meeting of the Japan Radiological Society (JRS 2019)*, Yokohama, Japan.
 - Godino-Moya, A., Cloquell, T., Royuela-del-Val, J., Martín-Fernández, M., Alberola-López, C. (2019). Recovering cardiac synchronism signal from k-space data in cardiac CINE MRI. *2019 Annual Meeting of the American Roentgen Ray Society (ARRS 2019)*, Honolulu, United States.
 - Godino-Moya, A., Menchón-Lara, R.M., Martín-Fernández, M., Alberola-López, C. (2020). Combination of alignedSENSE and groupwise motion-compensated compressed SENSE for cardiac CINE MRI reconstruction. *37th European Society for Magnetic Resonance in Medicine and Biology Scientific Meeting (ESMRMB 2020)*, Barcelona, Spain. A **Certificate of Merit Award** was received for this communication.

Chapter 2

BACKGROUND

2.1 Nuclear Magnetic Resonance

It is well known that an object is composed by atoms, which can be divided in turn into a nucleus and their orbiting electrons. A fundamental property of nuclei is that those with an odd atomic number, such as the hydrogen, possess an angular momentum, called *spin* [14]. Like any spinning charged object, a nucleus with a non-zero spin creates a magnetic field around it, called *magnetic moment*. Although spin and its interaction represent a quantum effect, in MRI spins do not need to be individually analyzed, but the macroscopic behaviour of spin systems can be fully described with classic magnetic field theory [15].

In the absence of an external magnetic field, spin directions are completely random, so macroscopic magnetization is null. However, when an external magnetic field \vec{B}_0 is applied (by convention it is applied in the \vec{z} direction), the spin directions tend to align along it, but this alignment happens partially, due to the fact that movements and interactions between neighboring nuclei at corporal temperature still play an important role. (Figure 2.1) [16]. In addition, spins start to precess around \vec{B}_0 at a certain angular frequency ω_0 , known as *Larmor frequency*, the expression of which

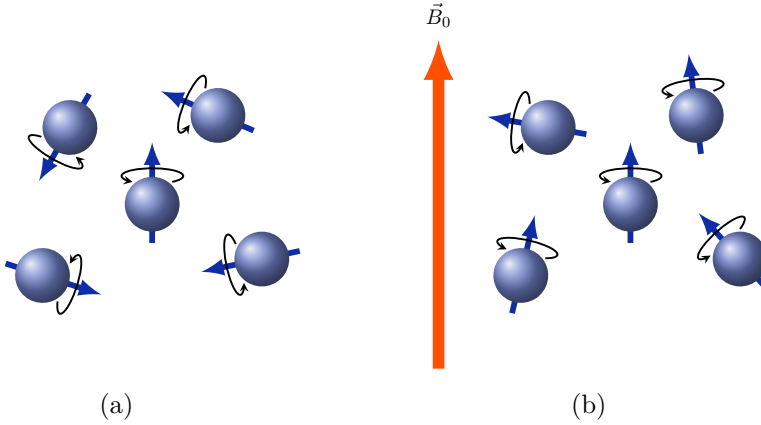


Figure 2.1: Nuclear magnetic moment vectors pointing in random directions (a) and in the presence of an external magnetic field \vec{B}_0 (b).

is given by

$$\omega_0 = \gamma \|\vec{B}_0\| \quad (2.1)$$

where $\|\cdot\|$ denotes the ℓ_2 -norm¹ and γ is a nucleus-specific constant called *gyromagnetic ratio*. In this situation, spins show a slight tendency to point themselves along the direction given by the main magnetic field, creating a net magnetization aligned with \vec{B}_0 .

Nonetheless, the described process is still stationary and, in order to obtain a measurable signal it is necessary to apply a time-varying radio-frequency (RF) pulse, $\vec{B}_1(t)$, during a short period of time. This RF pulse is applied perpendicularly to \vec{B}_0 and its frequency ω_{RF} is tuned to the Larmor frequency, modeled as [14]:

$$\vec{B}_1(t) = B_1^e(t) \cdot [\cos(\omega_{RF} \cdot t) \vec{x} - \sin(\omega_{RF} \cdot t) \vec{y}] \quad (2.2)$$

where $B_1^e(t)$ defines the envelope of the RF pulse. The effect of the net magnetization $\vec{M} = [M_x, M_y, M_z]$ under the application of the RF pulse

¹The ℓ_p -norm of a vector $\mathbf{x} \in \mathbb{C}^n$, $n \in \mathbb{N}$, $p \in \mathbb{R}^+$ is defined as $\|\mathbf{x}\|_{\ell_p} = (\sum_{i=1}^n |x_i|^p)^{\frac{1}{p}}$. Note that when no ℓ_p subscript is specified, it refers to the ℓ_2 -norm ($p = 2$).

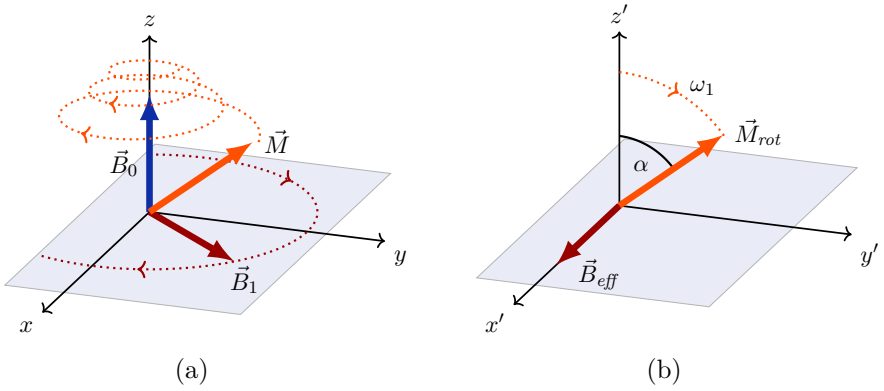


Figure 2.2: Displacement of the net magnetization \vec{M} after the application of a RF pulse \vec{B}_1 along the \vec{x} direction in both a static frame of reference (a) and a rotating frame of reference (b).

$\vec{B}_1(t)$ is modeled by the Bloch equation

$$\frac{d\vec{M}}{dt} = \gamma \vec{M} \times \vec{B} - \frac{M_x \vec{x} + M_y \vec{y}}{T_2} - \frac{(M_z + M_{0z}) \vec{z}}{T_1} \quad (2.3)$$

where \vec{B} denotes the total magnetic field $\vec{B} = \vec{B}_0 + \vec{B}_1$, M_{0z} is the value of the magnetization when only \vec{B}_0 is present (thermal equilibrium value) and T_1 and T_2 are two constants that describe the relaxation process.

A common approach at this time is to define a frame of reference that rotates around the \vec{z} direction at Larmor frequency, to get rid of the effect of the Larmor-precession (Figure 2.2). In this new rotating frame of reference the general Bloch equation (Eq. (2.3)) can be expressed as follows [14]:

$$\frac{d\vec{M}_{rot}}{dt} = \gamma \vec{M}_{rot} \times \vec{B}_{eff} - \frac{M_{x'} \vec{x}' + M_{y'} \vec{y}'}{T_2} - \frac{(M_{z'} + M_{0z}) \vec{z}'}{T_1} \quad (2.4)$$

where \vec{M}_{rot} is the magnetization vector in the new rotating frame of reference and \vec{B}_{eff} is the applied magnetic field, the value of which is given

by

$$\vec{B}_{eff} = \left(B_0 - \frac{\omega_{RF}}{\gamma} \right) \vec{z}' + B_1 \vec{x}' \quad (2.5)$$

The frequency ω_1 at which \vec{M}_{rot} precesses around \vec{B}_{eff} is given by Eq. (2.6) and the so-called flip angle α that depends on the strength and duration of the applied RF pulse can be written as Eq. (2.7).

$$\omega_1 = \gamma \|\vec{B}_{eff}\| = \|\vec{B}_1\| \quad (2.6)$$

$$\alpha = \int_0^{\tau_p} \gamma B_1^e(\tau) d\tau \quad (2.7)$$

After a magnetized spin system has been perturbed from its thermal equilibrium state by an RF pulse, it will return to this original equilibrium after removing the RF pulse, according to the laws of thermodynamics [14]. This process is called *relaxation* (Figure 2.3) and can be described by the Bloch equations given by Eq. (2.3). Specifically, in the rotating frame, we have

$$\begin{cases} \frac{dM_{z'}}{dt} = -\frac{M_{z'} - M_{0z'}}{T_1} \\ \frac{dM_{x'y'}}{dt} = -\frac{M_{x'y'}}{T_2} \end{cases} \quad (2.8)$$

The first term corresponds to the longitudinal or spin-lattice relaxation by whom the longitudinal magnetization recovers in order to realign with the static field \vec{B}_0 :

$$M_{z'}(t) = M_{0z'} \cdot \left(1 - e^{-\frac{t}{T_1}} \right) + M_{z'}(t=0) \cdot e^{-\frac{t}{T_1}} \quad (2.9)$$

The second term corresponds to the transverse or spin-spin relaxation, which refers to the transverse component of the net magnetization due to the dephasing of the spins by the small contributions to the magnetic field that vary from spin to spin:

$$M_{x'y'}(t) = M_{x'y'}(t=0) \cdot e^{-\frac{t}{T_2}} \quad (2.10)$$

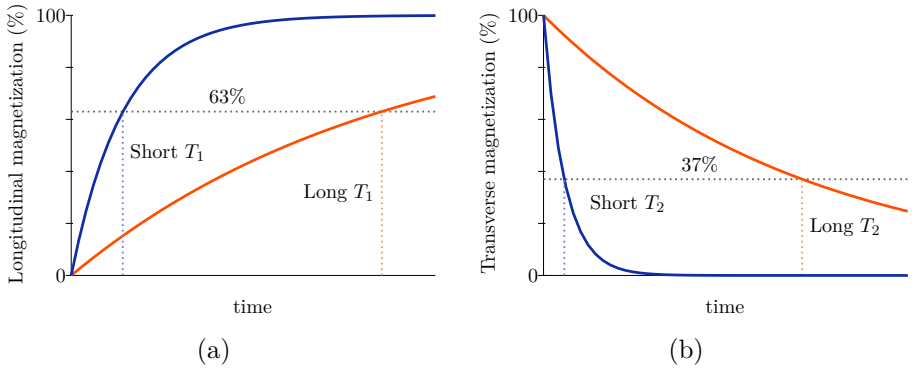


Figure 2.3: Relaxation of both longitudinal (a) and transverse (b) components for different constant decays.

Another aspect that causes spin dephasing is the presence of an inhomogeneous magnetic field, ΔB_{inhom} . The transversal relaxation due to the time independent field inhomogeneities and spin-spin interactions is called T_2^* and is related to T_2 by the following relation [17]:

$$\frac{1}{T_2^*} = \frac{1}{T_2} + \frac{1}{\Delta T_2} \quad (2.11)$$

where $\frac{1}{\Delta T_2} = \gamma \Delta B_{inhom}$ and $\Delta B_{inhom} \geq 0$. Note that T_2^* is always smaller or equal to T_2 , since $\gamma > 0$.

These relaxation constants, as well as the proton density —i.e., the number of protons per volume unit—, are parameters characteristic to each tissue. By properly setting two parameters from the MR acquisition sequence, namely Echo Time (TE) and Repetition Time (TR), images can be weighted to provide contrast sensitive to any of these three parameters (T_1 , T_2 and T_2^*).

2.2 Signal localization

RF pulses give rise to time varying signals in the transverse plane that can be measured. However, the receptor will observe the superposition of the

signals coming from all excited spins and therefore the exact spatial origin of each cannot be determined without additional processing. To this end, a gradient field \vec{B}_G , whose amplitude varies linearly with the position, is applied:

$$\vec{B}_G(\vec{r}) = \langle \vec{G}, \vec{r} \rangle = G_x x + G_y y + G_z z \quad (2.12)$$

The presence of such gradient modifies the precession frequency of the spins of the object along its direction

$$\omega(\vec{r}) = \omega_0 + \gamma B_G(\vec{r}) \quad (2.13)$$

and the received signal $s(t)$ would be

$$s(t) = \int_{\Omega} M_{x'y'}(\vec{r}, t) e^{-i\gamma \int_0^t \langle \vec{G}(\tau), \vec{r} \rangle d\tau} d\vec{r} \quad (2.14)$$

Including the definition of the k -space trajectory as

$$\vec{k}(t) = \frac{\gamma}{2\pi} \int_0^t \vec{G}(\tau) d\tau \quad (2.15)$$

the received signal can be expressed as

$$s(t) = \int_{\Omega} M_{x'y'}(\vec{r}, t) e^{-2\pi i \langle \vec{k}(t), \vec{r} \rangle} d\vec{r} \quad (2.16)$$

It can be seen from Eq. (2.16) that the receive signal $s(t)$ is a three-dimensional Fourier Transform evaluated at locations $\vec{k}(t)$. The reason of spatial encoding is to use different gradients to visit the different k -space locations (phase-encoding steps) while the received signal is sampled. It can be proved that the three-dimensional FT of the RF pulse defined along the visited k -space would define the excitation profile. This is the basis for slice selection.

2.2.1 k-Space sampling

As stated in Section 1.1, time reduction in MRI can be achieved if only a portion of k-space is acquired. According to this, some of the most commonly used sampling schemes are explained below.

Radial sampling of k-space was the first trajectory used in an MRI experiment, which was carried out by Lauterbur in 1973 [18]. However, it was widely substituted in the 1980's by the spin-warp technique [19], which employed Cartesian data sampling. The principal advantage of Cartesian sampling is that k-space data points are regularly spaced on a rectangular grid (Figure 2.4a), so that the Fast FT (FFT) algorithm can be applied directly to the acquired k-space data to recover an image. Radial sampling, however, obtains k-space data points that do not fall on a rectangular grid; k-space is sampled with equally spaced radial lines, all of which traverse the center of k-space (Figure 2.4c). In order to apply the FFT to these non-uniformly sampled data, they must be transformed into a Cartesian grid. This process, known as *gridding*, is computationally complex and time demanding [20].

Cartesian acquisitions show significantly higher sensitivity to motion. Translations in image space lead to phase offsets in k-space. Thus, image copies appear from aliasing that contaminate the FOV along the phase-encoding direction, which often give rise to images that do not allow diagnostic tasks. Radial acquisitions, in contrast, show higher robustness to motion due to the following facts: the overlap of spokes in the k-space center creates a time-averaging effect and, since the readout direction has variable orientations, object movements do not translate into shifted image copies. These resulting artifacts appear as streaks, that radiate from the motion affected regions. Therefore, they are easy to identify and rarely hide diagnostic information, since they tend to merely add texture-like patterns [21].

The use of efficient k-space sampling strategies has been largely inves-

tigated to reduce acquisition time and to generate high Signal-to-Noise Ratio (SNR) images. Echo-Planar Imaging (EPI) [22] is one of the fastest MRI pulses sequences and can be used for both 2D and 3D imaging. It is designed to collect multiple lines of k-space after a single RF excitation, resulting in a zig-zag traversal of k-space (Figure 2.4b).

Azimuthal undersampling may speed up image acquisition without sacrificing spatial resolution. Since each profile incorporates data from the center of k-space, the global image structure is maintained and potentiates an increase of the image update rate in dynamic MRI [23, 24]. However, uniform radial sampling scheme is restricted to a constant length of the acquisition window and requires a new scan for each desired temporal resolution. Golden-radial acquisition uses a constant azimuthal profile spacing based on the Golden Ratio, known as *golden angle* ($111,246^\circ$). In contrast to uniform radial sampling, where profiles may not be distributed over the entire radial space or may be sampled more than once, golden angle guarantees an optimal profile distribution for any arbitrary number of profiles used in reconstruction (Figure 2.4c and 2.4d) [24].

Spiral sampling is one of the most efficient sampling schemes [25–27], where k-space data are collected along a spiral curve and it is very often that spirals are interleaved, providing more densely coverage of k-space (Figure 2.4e). Like radial k-space sampling, spiral sampling is relatively robust to motion artifacts, but it is less robust to undersampling than radial schemes [28]. For spiral scanning, it is desirable to perform a one-time calibration for gradient delays and eddy currents [29–31].

Stack of Stars [21] is a 3D acquisition scheme, which acquires the k_x - k_y plane along radial spokes and the k_z direction with Cartesian sampling. The angle of the radial spokes can be ordered using an equidistant scheme (uniform radial) or using the golden angle scheme (Figure 2.4f). Spiral phyllotaxis [32] is another 3D sampling pattern, consisting of several *interleaves*. Each interleave is formed by a spiral in the upper hemisphere and its complementary spiral in the lower hemisphere, which are joined by spokes,

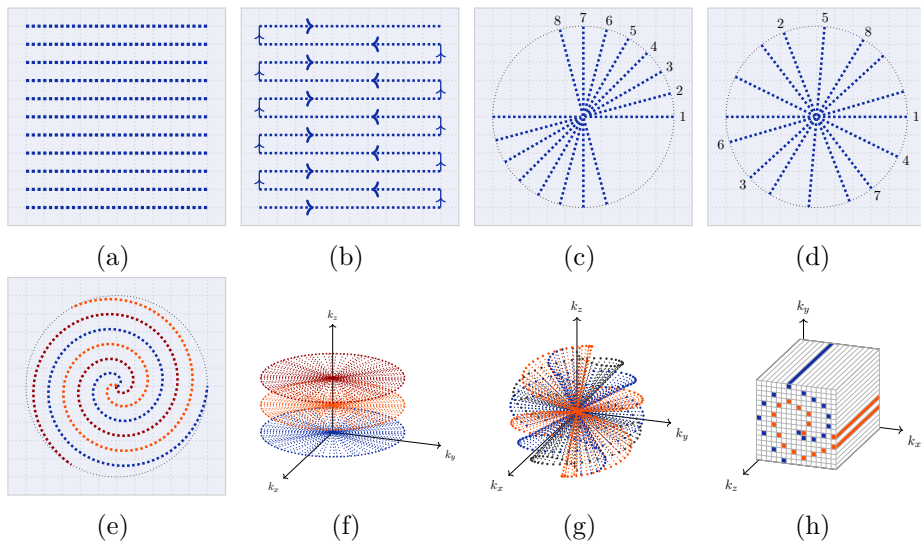


Figure 2.4: Different trajectories for k-space subsampling: Cartesian (a), EPI (b), uniform radial (c), Golden-radial (d), spiral (e), Stack of Stars (f), spiral phyllotaxis (g) and G-CASPR sampling (h).

forming a lattice. This gives rise to an overall uniform distribution of the readouts and optimized interleaving properties, that minimizes the effect of eddy currents, when the number of interleaves is a Fibonacci number², since the trajectory self-arranges in such a way that the displacements between successive readouts within one interleave are minimized. Furthermore, it is intrinsically prepared for self-navigated cardiac MRI, since the center of k-space is always sampled (Figure 2.4g). These non-Cartesian sampling patterns, as mentioned before, imply to include density compensation and gridding steps in the reconstruction problem, which may be complex and time consuming. To overcome this issue, some pseudo-radial trajectories have been proposed. ROCK (ROtating Cartesian K-space) [33] defines a rotating Cartesian k-space reordering, where a spiral path is generated and subsequently mapped to a Cartesian grid. Then the path is rotated

²Fibonacci numbers are those from the so called Fibonacci sequence, defined by $a_n = a_{n-1} + a_{n-2}$, for $n > 3$ and $a_1 = a_2 = 1$.

according to golden-angle until the desired number of samples is reached. The undersampling rate grows exponentially along radial direction and k-space center line is repetitively sampled as a respiratory motion surrogate. VDRad (Variable-Density sampling and Radial view ordering) [34] defines a temporal ordering of phase-encoding lines on a Cartesian grid that resemble spirals. This scheme aims to maintain a variable-density pseudorandom subsampling, by segmenting k-space according to its radius and grouping the lines into rings. The number of lines per ring is varied, so that lines from smaller ring groups are chosen more often than lines in larger ring groups. The advantage of this scheme is that variable-density sampling has shown better results for compressed sensing methods [35]. In a similar way, G-CASPR (Golden angle Cartesian Acquisition with Spiral PRofile ordering) [36] defines a temporal ordering of phase-encoding lines on a Cartesian grid, whose interleave is temporally ordered according to a golden ratio permutation (Figure 2.4h), resulting in a quasi-uniform sampling pattern of k-space. In Appendix A a generalized 3D Cartesian sampling scheme with spiral golden-angle ordering is provided. This scheme allows the practitioner to select from a uniform sampling pattern of k-space to a denser sampling scheme in its center by means of a continuous parameter α .

2.3 Image reconstruction

As mentioned in previous sections, MRI is a slow imaging technique due to its demanding sampling requirements. Therefore, in this section the focus is set on how acquisitions can be accelerated. Specifically, the fundamentals of parallel MRI are described as well as modern algebraic reconstruction techniques that use prior knowledge and regularization, with special attention to those approaches that have served as basis to develop the algorithms presented in this Thesis.

2.3.1 Parallel Imaging

Parallel Imaging (PI) [37,38] has its origin in Phased Array technology [39], with the aim of obtaining better SNR in reconstructed images [40]. Multiple antennas (also known as coils or channels) are placed around the object to be studied (Figure 2.5a). The images coming from each antenna can be later combined and, as a result, noise can be reduced. Thus, the SNR of the final image is improved. However, nowadays this approach is usually used to reduce acquisition times by undersampling k-space data [41].

As previously stated, the data are simultaneously sampled by N_c different coils placed around the object under study (see Figure 2.5a). The signal that each antenna receives varies as a function of the position, \vec{r} (the closer an antenna to a certain location, the stronger the signal it receives). An antenna can be characterized mathematically by its sensitivity map $C_n(\vec{r})$, so the signal $s_n(\vec{r})$ received by each antenna can be expressed as

$$s_n(\vec{r}) = C_n(\vec{r}) \cdot s(\vec{r}), \quad n = 1, \dots, N_c \quad (2.17)$$

where $s(\vec{r})$ represents the original image. In order to reduce acquisition time, some k-space lines can be skipped, resulting in aliased images. Even if the same k-space positions are acquired by all the coils, the data they receive are affected by different antenna profiles or *sensitivities*, therefore each coil is acquiring different information. Consequently, this new information incorporated by the antennas can be used to recover the missing data and reconstruct the original image. The most well-known PI techniques are SENSE and GRAPPA. Since most of the work developed in this Thesis takes SENSE as its basis, this technique will be described in more detail in the next subsection.

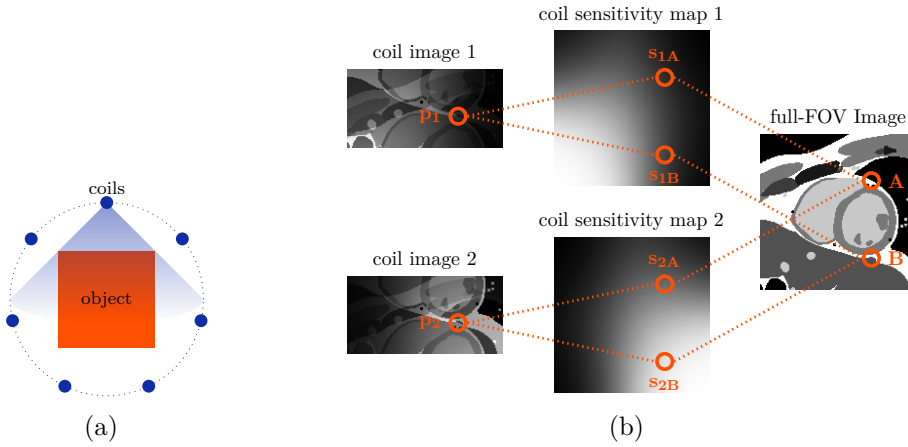


Figure 2.5: Parallel imaging scheme. Distribution of a multi-coil system around the object of study (a). Example of a regular subsampling with an AF of 2 and its pixel-wise resolution in the image domain (b) (SENSE).

2.3.2 SENSE

SENSitivity Encoding (SENSE) [37] is one of the most employed PI techniques, which is performed in the image domain after obtaining the images for each coil individually—in contrast to GRAPPA (Generalized Auto-calibrating Partially Parallel Acquisitions) that operates in k -space *before* obtaining the images. The use of multiple coils permits the reduction of the number of phase-encoding steps by means of increasing the distance of sampling positions in k -space while maintaining the maximum k -values. It is well-known that reducing the sampling density results in a reduction of the FOV, causing aliasing. In the first step, SENSE reconstruction creates one such aliased image for each coil element by means of the FT, creating a set of intermediate images. The second step is to create a full-FOV image by combining that set of intermediate images. To this purpose, the signal superposition underlying the fold-over effect must be undone. The key idea of SENSE is that the superposition of signals occurs with different weights according to the local coil sensitivities. Let us consider an acquisition with

two coils and an AF of 2 (Figure 2.5b). The original signal arising from the point A would be affected by the sensitivity of the two coils, namely, s_{1A} and s_{2A} . However, due to undersampling, the images obtained from each coil would be aliased and each pixel p would be the sum of the contribution of two pixels (A and B , in this example). Denoting this pixel values from coil images p_1 and p_2 , it can be written

$$\begin{aligned} p_1 &= s_{1A} \cdot A + s_{1B} \cdot B \\ p_2 &= s_{2A} \cdot A + s_{2B} \cdot B \end{aligned} \tag{2.18}$$

Since p_i and s_i ($i = 1, 2$) are known values, the true values A and B can be easily recovered by solving that system of 2 equations and 2 unknowns. A similar process can be done for all pixels and using a compact matrix vector notation the problem is formulated as

$$\mathbf{y} = \mathbf{E}\mathbf{m} = \mathbf{A}\mathcal{F}\mathbf{S}\mathbf{m} \tag{2.19}$$

where \mathbf{m} is the true image to be recovered and \mathbf{y} denotes all the k-space measurements by all the coils, defined both as a single column vector. The matrix \mathbf{E} is often called *encoding matrix* and comprises the coil sensitivity maps \mathbf{S} , the Fourier transform \mathcal{F} and the undersampling mask \mathbf{A} , which keeps only the acquired k-space positions and coincides for all coils. The unfolding process is possible as long as the matrix inversions in Eq. (2.19) can be performed. In particular, the number of pixels to be separated must not exceed the number of coils. On the other hand, in a real application this is generally not possible (due to noise presence, matrix size...), so the problem is solved as an optimization problem in an iterative manner [37].

Sensitivity based reconstruction requires highly accurate sensitivity assessment. The first step in generating such maps is to acquire and reconstruct single-coil, full-FOV images of the slice of interest in a conventional manner. By dividing each of these images by a body coil image a more homogeneous scaling is achieved, rather than “sum of squares” of the

set, since this is only applicable if the object phase is sufficiently smooth. However, resulting sensitivity maps are contaminated by noise, thus a smoothing procedure of polynomial fitting is performed to obtain refined sensitivity maps [37].

2.3.3 Compressed Sensing

The CS theory is remarkably extensive and therefore it is not covered in depth in this section. A thorough mathematical introduction can be found in [42]. The main ideas of the CS theory state that if the encoding matrix \mathbf{E} (Eq. (2.19)) satisfies the Restricted Isometry Property (RIP) for all S -sparse vectors (i.e., those vectors with S non-zero elements at most), and if the vector $\tilde{\mathbf{m}}$ is S -sparse and a solution of Eq. (2.19), then an exact recovery of $\tilde{\mathbf{m}}$ is possible by solving the following ℓ_1 -minimization problem [43]

$$\underset{\tilde{\mathbf{m}} \in \mathbb{C}^n}{\text{minimize}} \|\tilde{\mathbf{m}}\|_{\ell_1} \quad \text{s.t.} \quad \mathbf{y} = \mathbf{E}\tilde{\mathbf{m}} \quad (2.20)$$

where \mathbb{C} is the complex number space and n the dimension of the vector $\tilde{\mathbf{m}}$. When the data are noisy, the ℓ_2 -norm of the error between the solution of the problem

$$\underset{\tilde{\mathbf{m}} \in \mathbb{C}^n}{\text{minimize}} \|\tilde{\mathbf{m}}\|_{\ell_1} \quad \text{s.t.} \quad \|\mathbf{E}\tilde{\mathbf{m}} - \mathbf{y}\|^2 < \epsilon \quad (2.21)$$

and the true vector $\tilde{\mathbf{m}}$, is below $K\epsilon$, where K is a given constant [43]. These results can be extended to vectors that are not sparse in the canonical coordinates, but in a transformed domain defined by certain operator Ψ . In such case, those vectors are said to be *sparse* or *compressible*. One last idea related to CS theory and RIP is that the encoding matrix obeys the RIP with almost sure probability, when sampling is incoherent (i.e., when randomness is included) [43].

2.3.4 k-t SPARSE-SENSE

As described in the previous section, CS states that an image can be recovered from a small number of incoherent measurements, if such an image is sparse or compressible. This idea inspired the method k-t SPARSE-SENSE [44], which is, in turn, a combination of k-t SPARSE [45] and SENSE. The rationale of this combination is that CS alone limits the acceleration, due to the requirement in the number of samples in practice (three or five times the number of sparse coefficients). Therefore, PI may increase AF, which is ultimately limited by noise amplification [44].

The method exploits both spatial and temporal sparsity of dynamic images, since they are highly redundant in both spaces. By using linear transformations (such as wavelets, FT, etc.) the dynamic image can be represented by means of a few sparse transform coefficients [45]. Specifically, cardiac CINE MRI images are sparse in the combined temporal Fourier and spatial domain (y - f space, usually), since only portions of the FOV require the full temporal bandwidth while other regions may be either static or have information limited to low temporal frequencies. The incoherence required by CS can be obtained by randomly excluding phase-encoding lines (k_y lines) with a different pattern for each time frame (t). This k_y - t random undersampling increases incoherence, since undersampling artifacts are incoherently distributed along two dimensions rather than one. Furthermore, the combination of k-t SPARSE and SENSE does indeed represent a form of distributed compressed sensing, due to the fact that joint sparsity is exploited —instead of individual coil-by-coil sparsity— to reconstruct one image series that represents the combination from all coils. Multicoil samples with different spatial information content are simultaneously obtained to reduce the required number of samples per coil needed to reconstruct an unaliased image, just as in PI. Even though the same k_y - t random undersampling pattern is shared for all coils, the convolution in k-space with the coil sensitivities will generate different

incoherent artifacts for each coil [44]. The image is then recovered by solving the following optimization problem:

$$\underset{\mathbf{m}}{\text{minimize}} \|\Psi\mathbf{m}\|_{\ell_1} \quad \text{s.t.} \quad \|\mathbf{A}\mathcal{F}\mathbf{S}\mathbf{m} - \mathbf{y}\|^2 < \epsilon \quad (2.22)$$

where \mathbf{m} is the dynamic image to be recovered, \mathbf{y} is the measured k-space data, Ψ is the operator that transforms the dynamic image into a sparse representation, \mathcal{F} is the spatial FFT, \mathbf{S} is the sensitivity coil maps matrix and \mathbf{A} is the sampling matrix. The parameter ϵ controls the fidelity of the reconstruction to the measured data and it is usually set as the noise level. Using a Lagrange multiplier and the temporal FFT (\mathcal{F}_t) as the sparsifying transform, the problem can be rewritten as follows:

$$\tilde{\mathbf{m}} = \arg \min_{\mathbf{m}} \left\{ \|\mathbf{A}\mathcal{F}\mathbf{S}\mathbf{m} - \mathbf{y}\|^2 + \lambda \|\mathcal{F}_t\mathbf{m}\|_{\ell_1} \right\} \quad (2.23)$$

where the parameter λ establishes a trade-off between data consistency and the sparsity of the solution, enforced by the ℓ_1 norm term.

A further improvement to this approach is proposed in [8], in which two different sparsifying transforms are used. Specifically, a combination of temporal total variation (tTV) and temporal FFT are used as follows:

$$\tilde{\mathbf{m}} = \arg \min_{\mathbf{m}} \left\{ \|\mathbf{A}\mathcal{F}\mathbf{S}\mathbf{m} - \mathbf{y}\|^2 + \lambda_1 \|\nabla_t\mathbf{m}\|_{\ell_1} + \lambda_2 \|\mathcal{F}_t\mathbf{m}\|_{\ell_1} \right\} \quad (2.24)$$

where ∇_t is the tTV operator. λ_1 and λ_2 are regularization parameters that satisfy $\lambda_1 = 10\lambda_2$, so that the second regularization term (i.e., the one that uses temporal FFT) is sufficiently small so as not to introduce temporal blurring artifacts, but sufficiently large to help suppress residual aliasing artifacts arising from the static regions.

2.3.5 Groupwise motion compensated compressed sensing

A common proposal in cardiac CINE MRI is to incorporate motion information to regularize the reconstruction problem in order to promote signal sparsity and achieve higher AF [46–51]. One of them is the groupwise (GW) MC-CS algorithm (GWCS) in [51], which has been used in this Thesis for both comparison purposes and as part of one of the reconstruction methodologies proposed in this Thesis. In GWCS approach, a first reconstruction is performed by applying kt-SPARSE SENSE with tTV as sparsifying transform:

$$\tilde{\mathbf{m}} = \arg \min_{\mathbf{m}} \left\{ \|\mathbf{A}\mathcal{F}\mathbf{S}\mathbf{m} - \mathbf{y}\|^2 + \lambda \|\nabla_t \mathbf{m}\|_{\ell_1} \right\} \quad (2.25)$$

Note that this modification of the original formulation of k-t SPARSE-SENSE in [44] will be hereafter referred as to *simple Parallel Imaging Compressed Sensing* (sPICS) in order to distinguish it from the improved version of k-t SPARSE-SENSE with the two different regularization terms [8] (i.e., Eq. (2.24)), which will be referred to as such and denoted by the acronym kt-SS for brevity.

Then, motion is estimated from this first reconstruction in a groupwise manner instead of pairwise one, i.e., the whole sequence is registered at once. The registration method will be explained in subsequent subsections. Afterwards, the motion in the moving sequence is compensated by an operator \mathcal{T}_{Θ} that deforms each cardiac phase to a common reference, resulting into a pseudostatic sequence. This pseudostatic sequence gives rise to a higher sparse representation when a sparsifying transform, such as tTV, is applied. However, the direct application of such operator may lead to severe artifacts in those areas where large deformations occur. This is due to the accumulated differences, which are implicitly weighted according to their corresponding areas in the motion corrected sequence, as opposed to those in the one to be reconstructed. Specifically, when the transformation \mathcal{T}_{Θ} gives rise to a contraction (the Jacobian of the transformation is

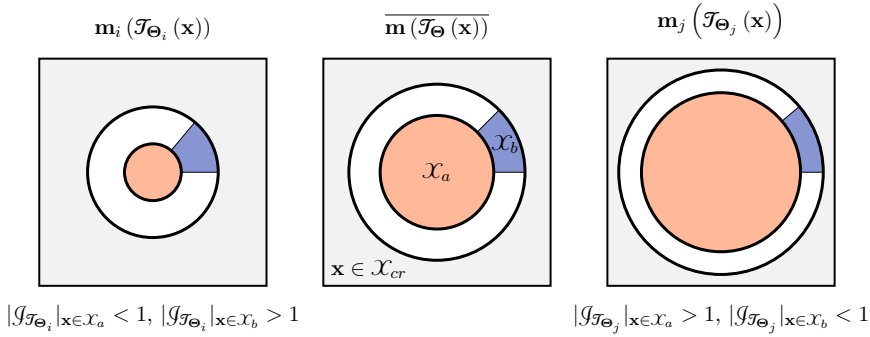


Figure 2.6: Relation between area changes and the Jacobian of the transformation. The scheme shows the left ventricle and the spatial transformations that map the common reference configuration, $\overline{\mathbf{m}}(\mathcal{T}_{\Theta}(\mathbf{x}))$, in the material point coordinate system, \mathcal{X}_{cr} (center) to systolic (left) and diastolic (right) cardiac phases. At systole, $\mathbf{m}_i(\mathcal{T}_{\Theta_i}(\mathbf{x}))$, the blood pool, \mathcal{X}_a , contracts (coloured in orange), so the Jacobian of the transformation takes values lower than one. In contrast, the cardiac muscle, \mathcal{X}_b , thickens (coloured in blue), so the Jacobian is greater than one in the myocardium. At diastole, $\mathbf{m}_j(\mathcal{T}_{\Theta_j}(\mathbf{x}))$, the situation is reversed.

lower than 1), that area will be overregularized during the reconstruction process, as it occupies a larger area in the reference configuration. On the contrary, when a dilatation occurs (the Jacobian is higher than 1), it will be underregularized (see Figure 2.6). Therefore, the Jacobian of the transformation is incorporated to the sparsifying operator in order to counteract this effect, so that each temporal difference is locally weighted. This sparsifying term avoids the presence of reconstruction artifacts and eliminates the need of an additional spatial regularization term. Thus, the problem is formulated as follows:

$$\tilde{\mathbf{m}} = \arg \min_{\mathbf{m}} \left\{ \|\mathbf{A}\mathcal{F}\mathbf{S}\mathbf{m} - \mathbf{y}\|^2 + \lambda \|\mathbf{m}\|_{\mathcal{J}_{\mathcal{T}_{\Theta}}} \right\} \quad (2.26)$$

where $\|\mathbf{m}\|_{\mathcal{J}_{\mathcal{T}_{\Theta}}}$ denotes the Jacobian weighted tTV regularization term,

which can be expressed by

$$\|\mathbf{m}\|_{\mathcal{J}_{\Theta}} = \frac{1}{|\mathcal{X}_{cr}|N} \int_{\mathbf{x} \in \mathcal{X}_{cr}} \sum_{n=1}^N |\mathbf{m}_{n+1}(\mathcal{T}_{\Theta_{n+1}}(\mathbf{x})) - \mathbf{m}_n(\mathcal{T}_{\Theta_n}(\mathbf{x}))| \mathcal{J}_{\mathcal{T}_{n+\frac{1}{2}}}(\mathbf{x}) d\mathbf{x} \quad (2.27)$$

where $\mathbf{x} \in \mathcal{X}_{cr} \subset \mathbb{R}^L$ denotes the coordinate space in which the common reference is defined, L is the number of dimensions of the image ($L = 2, 3$), N is the number of frames, $\mathcal{T}_{\Theta_n}(\mathbf{x}) \equiv \mathcal{T}_{\Theta}(\mathbf{x}, n)$ represents the spatial transformation —controlled by the set of parameters Θ — incurred by the n -th frame $\mathbf{m}_n(\mathbf{x}) \equiv \mathbf{m}(\mathbf{x}, n)$ of the dynamic image \mathbf{m} to match a common reference motion state³ and the term $\mathcal{J}_{\mathcal{T}_n}(\mathbf{x})$ denotes the Jacobian of the transformation $\mathcal{T}_{\Theta_n}(\mathbf{x})$. Given the discrete nature of the temporal index n , the the Jacobian of the transformation at time instant $(n + 1/2)$ is approximated by

$$\mathcal{J}_{\mathcal{T}_{n+\frac{1}{2}}}(\mathbf{x}) \approx \frac{1}{2} [\mathcal{J}_{\mathcal{T}_n}(\mathbf{x}) + \mathcal{J}_{\mathcal{T}_{n+1}}(\mathbf{x})] \quad (2.28)$$

2.3.5.1 Motion Estimation

Cardiac motion in the images is estimated by using a groupwise registration method based on the Free Form Deformation (FFD) model with B-splines [52]. FFDs rely on a parametric model that deforms an object by manipulating a mesh of K control points $\{\mathbf{u}_k | 1 \leq k \leq K\}$, governed by a set of transformation parameters $\Theta = \{\Theta_n | 1 \leq n \leq N\}$ with $\Theta_n = \{\theta_{n, \mathbf{u}_k}\}$ and $\theta_{n, \mathbf{u}_k} \in \mathbb{R}^L$.

Thus, FFDs are used here to describe the N nonrigid deformations \mathcal{T}_{Θ} that map the coordinates of each material point in a common reference image into its corresponding coordinates in each frame. The details of how the transformation is obtained are given in the Section 2.3.5.2. Using the variance of the intensity along time as groupwise registration metric,

³The transformation is defined from the space of the common reference motion state to the space of each dynamic image, so that it is precisely the reference image the one that is deformed.

the optimal set of transformation parameters Θ that describe the spatial transformations \mathcal{J}_Θ can be found by solving the following optimization problem:

$$\tilde{\Theta} = \arg \min_{\Theta} \left\{ \sum_{n=1}^N \sum_{\mathbf{x} \in \mathcal{X}_{cr}} \left[\mathbf{m}_n(\mathcal{J}_{\Theta_n}(\mathbf{x})) - \frac{1}{N} \sum_{k=1}^N \mathbf{m}_k(\mathcal{J}_{\Theta_k}(\mathbf{x})) \right]^2 + \mathcal{R}_1(\Theta) \right\} \quad (2.29)$$

where $\mathcal{R}_1(\Theta)$ represents an additional regularization term given by the second order spatio-temporal derivatives of the motion fields approximated by finite differences, the purpose of which is to promote smoothness of the estimated spatial deformations:

$$\mathcal{R}_1(\Theta) = \sum_{n=1}^N \sum_{\mathbf{x} \in \mathcal{X}_{cr}} \left(\beta_1 \left\| \nabla_{\mathbf{x}}^2 \mathcal{J}_{\Theta_n}(\mathbf{x}) \right\|^2 + \beta_2 \left\| \nabla_t^2 \mathcal{J}_{\Theta_n}(\mathbf{x}) \right\|^2 \right) \quad (2.30)$$

where the parameters β_1 and β_2 are used to weight the spatial and temporal regularization terms, respectively [50].

2.3.5.2 B-Spline Free Form Deformation model

Translation, rotation and scaling are the only means for describing a rigid transformation. However, soft tissues of the body, especially the heart, can be deformed in ways that such transformations cannot fully describe [53]. Therefore, non-rigid deformations are needed.

FFD models are a powerful tool for modelling arbitrary deformations applied to objects. The basic idea of them is that an object can be deformed by manipulating a regular grid of control points, which are distributed across the full object with a certain resolution.

In this Thesis, a FFD model based on cardinal cubic B-Splines is adopted. B-splines are functions defined piecewise by polynomials that have minimal support with respect to a given degree, smoothness and domain partition. B-spline functions pass through a number of knots and

create smooth shapes and surfaces. It is very common to use FFD based on third-order B-spline basis functions, since they present a good balance between smoothness and support region [54]. Therefore, they are suitable for modeling the elastic deformations of the hearth and the surrounding tissues.

2.3.5.2.1 Forward model

This Section is focused in explaining the 2D case, but the model is easily extendable to the 3D case. The set of control points $\mathbf{u} = (u_1, u_2) \in \mathbb{R}^2$, is located over a region of interest (ROI) in the pixel mesh, $\mathcal{X}_{cr} \subset \mathbb{R}^2$, so that the ROI is fully covered (see Figure 2.7). Notice that the ROI may be chosen considering some margin in each direction of the image to avoid border effects. The resolution of the control point grid, i.e., the spacing between control points, is denoted by $\Delta = (\Delta_1, \Delta_2)$. For simplicity, it is set to be constant, and satisfies the relation $\Delta_l K_l \leq N_l$, where N_l and K_l are the number of pixels in the ROI and the number of control points, respectively, along the l direction. Therefore, each control point \mathbf{u} can take values in the interval⁴ $-\lfloor \frac{K_l}{2} \rfloor \leq u_l \leq \lfloor \frac{K_l-1}{2} \rfloor$. If the position of the center of the control point grid, in the image coordinate space, is defined as $\mathbf{c} = (c_1, c_2) = \left(\left\lfloor \frac{N_1}{2} \right\rfloor, \left\lfloor \frac{N_2}{2} \right\rfloor \right)$, the position of the control point \mathbf{u} can be written as $\mathbf{p}(\mathbf{u}) = \mathbf{p}_{\mathbf{u}} = (p_{\mathbf{u}_1}, p_{\mathbf{u}_2}) = \mathbf{c} + \Delta \odot \mathbf{u}$, where ‘ \odot ’ denotes the Hadamard product⁵.

The resolution of the control point grid plays an important role, since it controls the elasticity of the transformation: lower values of Δ will allow to obtain very local transformations, as control points will only have influence inside a small pixel neighborhood, meanwhile higher values will allow to

⁴The the *floor* operator (nearest lower integer) is denoted by $\lfloor \cdot \rfloor$, whereas $\lceil \cdot \rceil$ denotes the *ceil* operator (the nearest higher integer).

⁵Given two matrices \mathbf{A} and \mathbf{B} of the same dimension $n \times m$, the Hadamard product is defined as the matrix $(\mathbf{A} \odot \mathbf{B})$, also of dimension $n \times m$, whose elements are given by $(\mathbf{A} \odot \mathbf{B})_{ij} = (\mathbf{A})_{ij}(\mathbf{B})_{ij}$.

obtain more global transformations, since the influence of control points will be extended to a larger area. The radius of influence of control points, r_l , is given by the following expression:

$$r_l = \frac{(E + 1) \Delta_l}{2} \quad (2.31)$$

where l denotes the dimension and E , the order of the B-Spline functions, which has been set to 3 in this Thesis. Thus, the local neighborhood affected by a control point is determined by the interval $[C_l^{inf}, C_l^{sup}]$ with $C_l^{inf} = -\lfloor \frac{c_l - x_l + r_l}{\Delta_l} \rfloor$ and $C_l^{sup} = \lfloor \frac{x_l - c_l + r_l}{\Delta_l} \rfloor$. Since the points outside the image will not have any effect, the previous expressions can be rewritten as $C_l^{inf} = \max\left(-\lfloor \frac{c_l - x_l + r_l}{\Delta_l} \rfloor, -\lfloor \frac{K_l}{2} \rfloor\right)$ and $C_l^{sup} = \min\left(\lfloor \frac{x_l - c_l + r_l}{\Delta_l} \rfloor, \lfloor \frac{(K_l - 1)}{2} \rfloor\right)$.

With all these previous definitions, the B-spline based transformation can be obtained as

$$\mathcal{T}_{\Theta}(\mathbf{x}) = \mathbf{x} + \sum_{u_1=C_1^{sup}}^{C_1^{inf}} \sum_{u_2=C_2^{sup}}^{C_2^{inf}} \left[\prod_{l=1}^2 B_E\left(\frac{x_l - p_{u_l}}{\Delta_l}\right) \right] \cdot \boldsymbol{\theta}_u \quad (2.32)$$

where $\boldsymbol{\theta}_u = (\theta_1, \theta_2)$ represents the control point displacements, and B_E stands for the third order ($E = 3$) B-spline function obtained through the Cox-DeBoor recursion formula, as defined in [55]. Deformations at each point are given by a 2D tensor product of 1D [52].

2.3.5.2.2 Backward model: inversion

Sometimes, the set of inverse transformations, $\mathcal{T}_{\Theta}^{-1}$, is needed. However, the inverse of a B-spline cannot be analytically obtained. Furthermore, such inverse transformation will not be described by another B-spline transformation in general. Therefore a numerical approach is adopted instead. We obtain, as an approximation of $\mathcal{T}_{\Theta}^{-1}$, the set points $\tilde{\mathbf{x}}$ that are mapped to the regular Cartesian grid of spatial locations, \mathbf{x}' , in which the

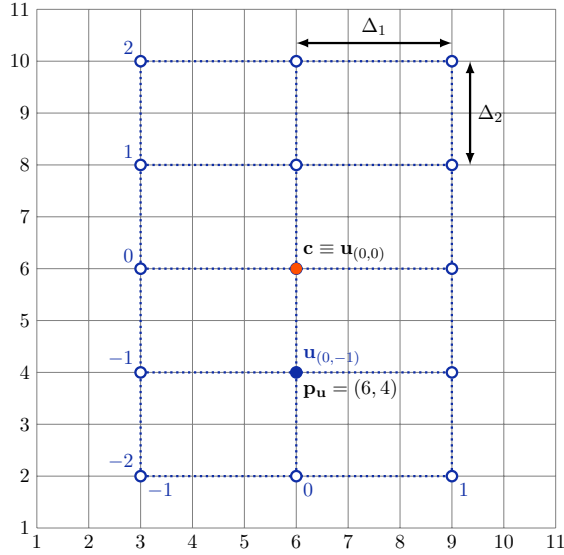


Figure 2.7: Design of the control point grid for FFD B-Spline transformations. Image coordinate grid is shown in black color, where as the control point grid is shown in blue. The center of the grid is highlighted in orange.

original images are defined, when \mathcal{T}_{Θ} is applied by solving

$$\tilde{\mathbf{x}} = \arg \min_{\mathbf{x}} \left\{ \sum_{\mathbf{x}' \in \mathcal{X}} \|\mathcal{T}_{\Theta}(\mathbf{x}) - \mathbf{x}'\|^2 \right\} \quad (2.33)$$

The solution of the optimization problem defined by Eq. (2.33) is equivalent of having a lookup table for the evaluation of $\mathcal{T}_{\Theta}^{-1}$ for each point \mathbf{u} . The main advantage of this procedure is that there is no deformation model assumption for the inverse transformation, but this solution will be only be valid for the set of points in \mathcal{X} where Eq. (2.33) is solved, which is compatible with the reconstruction methods that have been used.

2.3.5.2.3 Composition

Once the transformations and their inverses are obtained, the transfor-

mation that map any position in the i -th frame into its corresponding position in the j -th frame can be easily calculated by function composition as follows:

$$\mathcal{T}_{\Theta}^{i \rightarrow j} = \mathcal{T}_{\Theta_j}^{-1} \circ \mathcal{T}_{\Theta_i}(\mathbf{x}) \quad (2.34)$$

2.3.6 Other image reconstruction methods

In previous subsections, the methods that have been directly used or served as the basis for this Thesis work have been explained in more detail. For completeness, in the next paragraphs some other image reconstruction methods and techniques are briefly reviewed.

2.3.6.1 Methods with PI and CS

Along with SENSE, GRAPPA [38] is one of the most well-known PI techniques. In contrast with the former, GRAPPA operates in k-space *before* obtaining the images. It takes only a constrained number of phase-encoding steps; many k-space lines are skipped, but lines passing through the center of k-space are fully sampled and constitute the auto calibration signal region (ACS). These ACS lines are used to calculate the weighting factors for each coil, that describe how each coil affects spatial frequencies within k-space. Then, missing k-space data are estimated using these weighting factors by means of a local linear combination of the sensed data. Once the missing information is estimated, a FT is performed to obtain an image free of aliasing for each coil. Finally, these images are combined to form the final reconstructed image.

UNFOLD (UNaliasing by Fourier-encoding the Overlaps in the temporal Dimension) [56] takes advantage of spatio-temporal redundancy jointly. k-Space is undersampled by a factor of 2, alternating even and odd samples along time direction, so that the aliased portion of the image alternates signs in successive frames. Consequently, aliasing can be easily eliminated by filtering out the non-overlapping replicas.

k-t BLAST (Broad-use Linear Acquisition Speed-up Technique) and *k-t* SENSE [57] divide the data in two groups, namely, undersampled and training data. In the x - f domain, undersampled data have full spatio-temporal resolution but are contaminated by aliasing artifacts. Training data, however, have low spatio-temporal resolution but no aliasing artifacts, due to the fact that they are located in the k -space center. These training data are used to estimate how data are contaminated by the undersampling process and guide the reconstruction problem to eliminate aliasing artifacts in the undersampled data. *k-t* GRAPPA [58] recovers the missing data by estimating their values based on neighboring data points in k - t space. *k-t* PCA is an extension of *k-t* BLAST and *k-t* SENSE that uses Principal Component Analysis (PCA) along the time dimension; it has shown higher AF with improved temporal fidelity [59].

2.3.6.2 Methods with motion estimation and motion compensation

Motion estimation (ME) —i.e., the process for the obtention of motion vectors between certain frames— and the subsequent motion compensation (MC) —i.e., the process for the relocation of pixels on frames according to certain given motion vectors— can be used to compensate some undesired motion (such as respiratory motion) and/or to promote sparsity in the images.

The reconstruction method in [60] suggests a general reconstruction framework based on a temporal multi-resolution scheme that combines PI with a MC strategy, to compensate the respiratory motion. The registration method that they employ is based on estimating the optical flow between two consecutive images. The optical flow is a vector field consisting of the changes in space coordinates, regarding to the direction of intensity flow. Therefore, it only works for registering images of the same modality and with consistent grey intensity values. Other assumption of this method is

that the deformation is smooth, which it is valid for soft tissue deformation, in general.

The approach in [61] incorporates a generalized motion correction formulation to CS reconstruction. The respiratory motion is estimated by the algorithm in [62], which combines hierarchical multiple local affine registrations. This algorithm starts with a global affine registration, after which a hierarchical splitting scheme is applied. At each subsequent level, the registration result is refined by splitting each parent block into children sub-blocks, in which local registrations are performed. A B-Spline interpolation scheme is used to combine all the affine transformations to produce a smooth output transformation after each level in the hierarchy.

k-t FOCUSS (FOCal Underdetermined System Solver) [63] decomposes the unknown image into a predicted and a residual images. The predicted image is obtained by means of a high quality frame of reference and a block matching algorithm applied separately to each frame. To estimate the inter-frame motion, *k-t* FOCUSS recommends using a fully sampled image as a reference frame. However, a reference image can be generated from the temporal average of *k-t* measurements for the entire image sequence or for only those images that correspond to the diastole phase, if the fully sampled image is not accessible. Temporal FT is applied to the residual image in order to promote sparsity in the solution. MASTeR (Motion-Adaptive Spatio-Temporal Regularization) [47], on the other hand, does not depend on a reference frame. The motion is estimated sequentially between adjacent frames in both backward and forward directions. These motion operators construct motion-adaptive transforms that use inter-frame motion to represent an image sequence in the form of forward and backward motion-compensated residuals, which are assumed to be sparse. The image sequence is recovered by enforcing sparsity in those residual terms.

The proposed method in [64] estimates the motion field between two successive images. It is based on the traditional brightness constancy

combined with a local shape constraint. A random walk optimization is adopted to estimate the optimal displacement field. Random walk scheme refers to a special category of Markov chains that can be used to scan multi-dimensional spaces. The random walk model simulates the probability of the pixel displacement at certain time instant to its neighbour positions. A series of random displacement propositions are applied to each pixel, whose magnitude is restricted to a maximum of possible random displacement. A cost function is defined, so that if the cost function for a certain pixel is smaller than a reference cost function value, then the expected displacement is updated for that pixel; otherwise, no updating is applied at this iteration. This process will continue until the stop criterion is reached.

These methods so far use ME between pairs of frames. Nonetheless, as pointed out in subsection 2.3.5, an alternative methodology estimates motion in a groupwise manner [51] —i.e., the whole dynamic sequence at once— and has reported improved reconstructed images. This algorithm has also been successfully adapted to the golden-radial acquisition pattern and whole-heart single BH CINE MRI [65].

2.3.6.3 Methods with low-rank decomposition

Other approaches combine low-rank matrix completion and CS theories, in which the dynamic image is divided into a low-rank component (L) and a sparse component (S). Therefore, they are usually referred as $L + S$ decomposition or Robust PCA (RPCA). In [66] a multi-coil $L + S$ reconstruction problem is formulated. The temporally correlated background is modelled as the L component whereas the organ motion is modelled as the S component. The nuclear norm⁶ and ℓ_1 -norm are used as convex surrogate functions for the rank function and ℓ_0 -norm, respectively, in the optimization problem. The $L + S$ model is sensitive to respiratory motion, which affects the quality of the reconstructed MR images.

⁶The nuclear norm of a matrix \mathbf{M} is defined as the sum of the singular values of \mathbf{M} .

The approach in [67] proposes an $L + S$ decomposition in conjunction with a registration algorithm for ME/MC. The inter-frame motion between pairs of images is estimated using block matching, where fully sampled frames and the background segment of the $L + S$ decomposition is used as reference. The images are divided into non-overlapping blocks of equal size and the motion vectors for each block on the individual dynamic frame are calculated by minimizing the mean absolute difference between specific blocks of the reference frames and dynamic frames. The motion compensation is carried out on the image domain by relocating the specified blocks of the reference frames according to the estimated motion vectors.

The method proposed in [68] extracts the respiration motion signal by applying an algorithm based on the Fourier shift theorem. Then, a demons-based image registration algorithm [69–71] is performed, where the translational displacement of the moving sequences is calculated with respect to the reference images by means of the local characteristics of them. Finally, respiratory motion is compensated to promote sparsity in the MC-CS reconstruction problem. In MALLRT (Motion Aligned Locally Low Rank Tensor) [72] a low rank constraint is enforced on image patch-based local tensors, which correspond to overlapping blocks extracted from a reconstructed high-dimensional image after groupwise inter-frame motion registration. The problem is solved by using variable splitting and the Alternating Direction Method of Multipliers (ADMM) framework.

2.3.6.4 Methods with manifold learning

Manifold learning (ML) [73] have been recently used in MRI to detect the most important features from the acquired data. This technique projects a high dimensional manifold (e.g., an image of large dimensions) to a corresponding low dimensional representation, preserving the neighborhood structure of the higher dimensional space.

SToRM (SmooThness Regularization on Manifolds) [74] introduces the

concept of ML in the regularization term. In this approach, image frames are modeled as points on a smooth and low-dimensional non-linear manifold. The entire dynamic sequence is recovered by enforcing similarity between neighboring image frames on the manifold. A kernel-based framework is proposed in [75]. This framework exploits simple tangent-space geometries defined on manifolds in Reproducing Kernel Hilbert Spaces (RKHS), and follows classical kernel approximation arguments to form the data-recovery task as a bi-linear inverse problem.

The main disadvantage of applying global transforms is that they are not specific to the image and can lead to insufficiently sparse representations. The authors in [76] propose a patch-based sparsifying method, where the image is divided into patches that sample a low-dimensional manifold embedded in a high dimensional space. They rely on the idea that patches can better capture the local image features and promotes sparsity at much higher undersampling rates. The reconstruction problem is formulated as a Low-Dimensional Manifold Model (LDMM), in which the patch manifold is used as regularizer in the optimization function.

A Double Tight Frame (DTF) approach is proposed in [77]. The image is decomposed into smooth and non-smooth region. They achieve sparse representations by using separately a wavelet transform in the smooth region and a curvelet transform in non-smooth region. The key point is to combine these sparse representations with a new mixed-norm regularization model; the latter is intended to preserve the edge structural details in non-smooth regions and piecewise-smooth information of image in smooth regions.

2.3.6.5 Methods with FB acquisitions

The iGRASP (iterative Golden-angle RAdial Sparse Parallel MRI) paradigm [78] is based on the continuous acquisition of k-space data following a golden-angle sampling pattern. Within this paradigm, it should be highlighted the

XD-GRASP framework (XD comes from eXtra-Dimensional) [79], where dynamic data are retrospectively sorted into extra cardio-respiratory motion states, rather than applying any sort of MC algorithm. The resulting multidimensional dataset is reconstructed using a CS approach, in which sparsity along the two temporal dimensions, namely, cardiac and respiratory, is simultaneously imposed. Although it was originally conceived for 3D reconstruction, has also been successfully applied to the 2D case. In [11] an extension of this approach is proposed; their authors include on one hand, a groupwise motion correction procedure in which both cardiac and respiratory motions are taken into account during the CS reconstruction process, and on the other hand, an efficient multi-resolution scheme dealing with the high computational cost that this reconstruction framework involves.

CASPR-Tiger (CArtesian trajectory with Spiral PRofile ordering and Tiny golden angle step for eddy current reduction) [80] is a self-gated Cartesian approach for FB 3D CINE MRI with isotropic resolution and no data rejection. It uses a modified version of G-CASPR [36] sampling scheme, in which the authors use tiny golden angles⁷, so that eddy current effects are reduced. Then, the images are reconstructed using a soft gating technique and an iterative SENSE with tTV scheme.

2.3.6.6 Methods with Deep Learning

Deep Learning (DL) has burst in every field related to imaging, due to the current development of Graphics Processing Units (GPU) and the availability of big data. Deep neural networks are currently used to solve either classification, regression or reconstruction problems, since they are able to establish complex relationships between data in multiple abstraction

⁷Tiny golden angles are small irrational angles that exhibit properties similar to the original golden angle. They are defined using the golden ratio $\Phi = (1 + \sqrt{5})/2$ and the sequence $\phi_n = \pi/(\Phi + n - 1)$, $n = 1, 2, \dots$. For more details, the reader is referred to [81].

levels out of some training datasets, with very high performance. However, there is a questioning attitude toward the long training period that DL needs. Nevertheless, the training stage is performed “only once” in the pre-production stage, so that in the production stage processing time would be non-critical.

The approach in [82] is proposed as a framework for reconstructing dynamic 2D cardiac MRI sequences from highly undersampled Cartesian data using a deep cascade of convolutional neural networks (CNN), which resembles iterative reconstruction of DL-methods, but allows end-to-end optimization of the reconstruction. The problem is posed as an iterative procedure in the image domain, where CNNs learn spatio-temporal correlations by combining convolution and data sharing approaches to reconstruct frames jointly, by means of alternate de-aliasing and data consistency steps.

MoDL (Model-based Deep Learning framework) [83] introduces a framework in order to develop deep architectures to solve arbitrary inverse problems. It combines the capacity of model-based reconstruction schemes with DL. The proposed architecture consists of numerical optimization blocks, to capture information about the image set, and data consistency blocks, to promote agreement on the measurements. This enables the use of complex forward models as well as to include image priors. In addition, the training is performed end-to-end with weight sharing across iterations, offering a better performance than other approaches that rely on pre-trained denoisers [83].

The approach in [84] proposes a Convolutional Recurrent Neural Network (CRNN) architecture to reconstruct high quality cardiac MRI from highly undersampled k-space data. It consists of a CRNN block, that acts as a proximal operator, and a data consistency layer, corresponding to a data fidelity term. Furthermore, recurrent connections across each iteration are used to share information among multiple iterations of the process, as well as bidirectional convolutional recurrent units to exploit the temporal dependency of dynamic sequences.

A conditional Deep de-Aliasing Generative Adversarial Network (DA-GAN) is proposed in [85], where the architecture is designed with a refinement learning method to stabilize a U-Net [86] generator to reduce aliasing artifacts. To preserve texture and edges the adversarial loss is integrated, as well as frequency-domain information, to enforce similarity in both image and frequency domains. This approach is able to reconstruct images in some milliseconds, which makes it suitable for real-time applications.

2.3.6.7 Conclusion

The MRI reconstruction is a very wide area of active investigation, that is continuously evolving, and has been briefly covered in the previous subsections. An extensive and more detailed survey can be found in [87]. Thus, in this Thesis we have focused on CS techniques that take into account motion, specially those that make use of ME/MC.

Chapter 3

METHODS

3.1 Space-time variant weighted regularization

In dynamic applications, like cardiac CINE MRI, consecutive frames are expected to be very similar to each other, so a sparser representation of the original sequence can be obtained; therefore, CS in combination with temporal sparsity is often used [8, 44, 88]. However, as stated in Chapter 1, temporal regularization may affect negatively the dynamic properties of the moving regions in the reconstructed image whenever the regularization parameter is not carefully selected. Specifically, a low value of the regularization parameter does not eliminate aliasing artifacts due to k-space undersampling, whereas a high value of the regularization parameter causes temporal blurring artifacts and loss of motion. It should be pointed out that not only information about the anatomical structure should be preserved, but also the motion, so that its potential abnormalities can be evaluated. In Figure 3.1 an example of this effect is shown. The figure shows the temporal evolution of one line of the reference image (vertical orange line in Figure 3.1a) after reconstruction both with a high value of the regularization parameter (Figure 3.1b) and with a low value of this parameter (Figure 3.1c). In the former, contractile movement of the myocardium is barely appreciated, but the intensities are soft along the

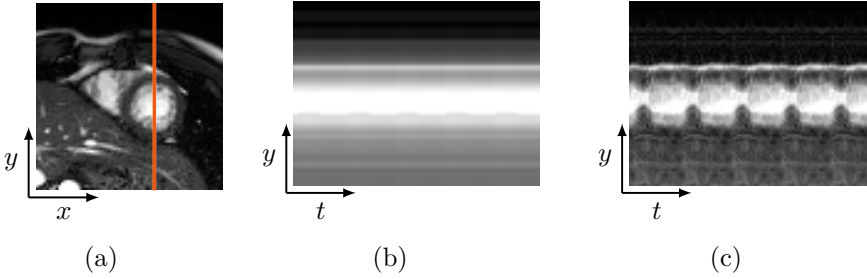


Figure 3.1: Effect of the regularization parameter in the reconstructed images. Temporal evolution of a single line in original image (a) in both reconstructions with a high value of the regularization parameter (b) and with a low value of the regularization parameter (c).

temporal dimension, so that undersampling artifacts are hardly seen. In the latter, on the contrary, myocardial movement is appreciated (wave-like patterns can be observed in the center of the image), but undersampling artifacts arise, which can be easier to appreciate in dark zones, as if they were some sort of noise.

A unique global regularization term is frequently used in the whole image for the reconstruction problem. However, as described in Section 2.3.4, the improved version of k-t SPARSE-SENSE [8] has two different sparsifying transforms, accounting for both dynamic and static regions in the image; specifically, tTV is employed for the dynamic region of the image while temporal FFT helps suppress residual aliasing artifacts from static regions (see Eq. 2.24). Nonetheless, these two regularization terms are applied globally to the whole image, i.e., λ_1 and λ_2 in that equation are constant values. The main drawback of applying global regularization terms is that they are not specific to the local image properties in terms of motion and the reconstruction may suffer, in particular, when the data are highly undersampled.

In this Thesis, we propose a methodology to dynamically adapt the regularization parameter according to the moving characteristics present in each point of the image. This methodology is based on the robust

registration technique for non-rigid motion estimation explained in Section 2.3.5.1, so that local motion properties can be adequately exploited. The reconstruction problem is formulated as a modified version of the original k-t SPARSE-SENSE [44], where the temporal FFT originally used has been substituted by tTV as sparsifying transform, since it has been reported that this operator offers reconstructions with lower root mean square error (RMSE) and higher temporal fidelity of myocardial wall motion than other operators such as temporal FFT or temporal PCA [8]. In addition, the regularization parameter λ has been substituted by a diagonal weighting matrix \mathbf{W} that locally leverages the regularization effect:

$$\tilde{\mathbf{m}} = \arg \min_{\mathbf{m}} \left\{ \|\mathbf{A}\mathcal{F}\mathbf{S}\mathbf{m} - \mathbf{y}\|^2 + \|\mathbf{W}\nabla_t\mathbf{m}\|_{\ell_1} \right\} \quad (3.1)$$

The selection of the weighting matrix \mathbf{W} entries and the underlying regularization parameter λ are explained in the following sections.

3.1.1 Weighting matrix

Different alternatives have been studied to define the matrix \mathbf{W} introduced in Eq. (3.1) and are described below.

3.1.1.1 Plateau regularization

In this strategy, the image is divided into two different regions, namely a *dynamic* region, which includes the heart and some other surrounding moving structures, and *static* (or pseudo-static) region, that includes the rest of the image or background, which barely moves. Therefore, the first step is to define a mask that contains the heart. This mask has been defined as the largest region where the temporal variance is higher than a certain threshold value γ , which has been empirically selected to accommodate the whole heart in the datasets used. Then, two different λ -values have been defined, namely, λ_{st} for the outer region, where *st* stands for *static*, and λ_{dyn} for the inner region, where *dyn* stands for *dynamic*. This procedure is

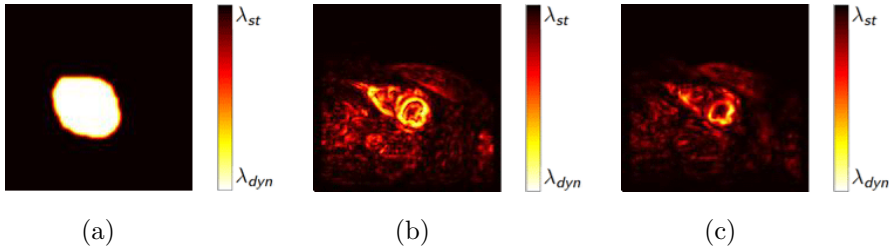


Figure 3.2: Different alternatives for the space-time variant weighting matrices: plateau regularization (a), motion weighted regularization by displacement fields (b) and motion weighted regularization by velocity fields (c).

formally expressed as follows:

$$w_{plateau}(\mathbf{x}, n) = \begin{cases} \lambda_{st}, & \text{Var}(\mathbf{x}) < \gamma \\ \lambda_{dyn}, & \text{Var}(\mathbf{x}) \geq \gamma \end{cases} \quad (3.2)$$

with $w_{plateau}(\mathbf{x}, n)$ the entry of the matrix \mathbf{W} corresponding to the spatial position \mathbf{x} and frame n , and the variance at point \mathbf{x} is defined as

$$\text{Var}(\mathbf{x}) = \frac{1}{N} \sum_{n=1}^N \left(\mathbf{m}(\mathbf{x}, n) - \frac{1}{N} \sum_{k=1}^N \mathbf{m}(\mathbf{x}, k) \right)^2 \quad (3.3)$$

Finally, the resulting mask is low-pass filtered to ensure soft transitions between the two regions.

3.1.1.2 Motion weighted regularization

In this set of strategies the magnitude of motion in the image determines the necessary amount of regularization needed in each pixel. To do this, we carry out a first reconstruction applying sPICS (Eq. (2.25)). Then, motion is estimated from the reconstructed images by using the registration algorithm explained in Section 2.3.5.1. The resulting transformations \mathcal{T}_{Θ} from the registration algorithm are used to obtain the displacement fields

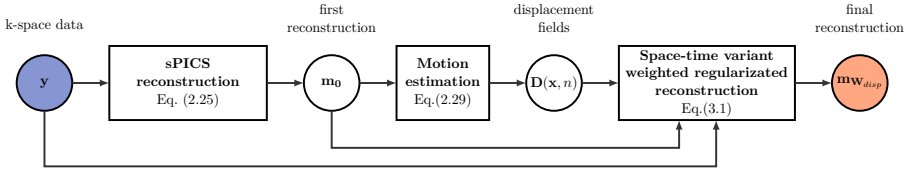


Figure 3.3: Space-time variant regularization reconstruction model. Motion is estimated in a first step of reconstruction and the obtained displacement fields are used to leverage the regularization in a second step of reconstruction. Alternatively, the velocity fields can be also used in the second step of reconstruction.

that are used to leverage the regularization parameter in a second step of reconstruction. If we denote $\mathbf{x}' = \mathcal{T}_{\Theta}(\mathbf{x}, n)$ as the transformed coordinates for the points \mathbf{x} in frame n , the modulus of the displacement $\|\mathbf{D}(\mathbf{x}, n)\|$ can be obtained as $\|\mathbf{D}(\mathbf{x}, n)\| = \|\mathbf{x}' - \mathbf{x}\| = \|\mathcal{T}_{\Theta}(\mathbf{x}, n) - \mathbf{x}\|$. The maximum and the minimum values of displacement modulus ($\|\mathbf{D}(\mathbf{x}, n)\|_{max}^2$ and $\|\mathbf{D}(\mathbf{x}, n)\|_{min}^2$, respectively) are associated to λ_{dyn} and λ_{st} , respectively, and the intermediate values for λ are calculated using linear interpolation (Eq.(3.4)). The rationale of this action is to increase regularization in more static areas and to decrease regularization in those areas where deformation is more pronounced. The pipeline of the whole reconstruction process is shown in Figure 3.3. Alternatively, the velocity fields, $\|\mathbf{V}(\mathbf{x}, n)\|$, derived from the displacements by means of temporal finite differences, have been also employed using a similar procedure (Eq.(3.5)), where $\|\mathbf{V}(\mathbf{x}, n)\|_{max}^2$ and $\|\mathbf{V}(\mathbf{x}, n)\|_{min}^2$ are the maximum and minimum velocity moduli, respectively. An example of these weighting matrices can be shown in Figure 3.2. The λ values have been selected with the methodology explained in Appendix B using twelve tentative values, ranging from 10^{-4} to 1, equally spaced in a logarithmic scale. Additionally, the resulting values for $w_{disp}(\mathbf{x}, n)$ and $w_{vel}(\mathbf{x}, n)$ were limited to lie within the interval $(\lambda_{dyn}, \lambda_{st})$

to eliminate any possible artifact caused by improper motion estimation.

$$w_{disp}(\mathbf{x}, n) = \lambda_{st} + \frac{(\lambda_{dyn} - \lambda_{st}) (\|\mathbf{D}(\mathbf{x}, n)\|^2 - \|\mathbf{D}(\mathbf{x}, n)\|_{min}^2)}{\|\mathbf{D}(\mathbf{x}, n)\|_{max}^2 - \|\mathbf{D}(\mathbf{x}, n)\|_{min}^2} \quad (3.4)$$

$$w_{vel}(\mathbf{x}, n) = \lambda_{st} + \frac{(\lambda_{dyn} - \lambda_{st}) (\|\mathbf{V}(\mathbf{x}, n)\|^2 - \|\mathbf{V}(\mathbf{x}, n)\|_{min}^2)}{\|\mathbf{V}(\mathbf{x}, n)\|_{max}^2 - \|\mathbf{V}(\mathbf{x}, n)\|_{min}^2} \quad (3.5)$$

3.2 Elastic alignedSENSE

An alternative approach to those presented so far is based on including a motion model directly in the data consistency term as opposed to including it in the regularization term [89, 90].

The method proposed in [89] is able to handle elastic motion models. It assumes that a corrupted image comes from a general matrix equation, the inversion of which provides the ideal image of the scanned object. This formulation can also be used to estimate motion using only partial spectral information, as shown in the alignedSENSE approach [90], where the authors reconstruct a static, multi-shot, 3D MRI brain volume subject to rigid motion between shots. Estimated motion is incorporated into the reconstruction model in an iterative manner to obtain a motion-free image. Their method does not assume any prior model for the image to be reconstructed, does not make use of external sensors and does not require modifications in the acquisition sequence [90]. The downside is the restrictive class of rigid motion used: this type of motion, however, is not suitable for deformable organs, such as the heart. Nevertheless, this idea of creating a single motion-free image (say, a pattern image) that is deformed to match the measured data may be of great interest to build a cardiac CINE reconstruction framework, as long as elastic motion is incorporated.

This Section focuses on the alignedSENSE formulation, which is here extended to handle elastic deformations and employs the 2D cardiac CINE

MRI reconstruction problem as a proof of concept. This approach, as originally posed, iterates between an image reconstruction problem and a deformation estimation problem. The second contribution of the Thesis is twofold; on one hand, a framework to incorporate elastic deformations in the pattern image is proposed; on the other hand, motion information is used to spatially weight the amount of regularization in both the reconstruction and the deformation problems. This allows us not only to pose the problem in terms of ℓ_2 -norms, which makes optimization more convenient, but also to simplify the problem so that a pattern image, along with a set of transformations, suffice to build an entire 2D CINE sequence.

The alignedSENSE approach for parallel multi-shot imaging was formulated in matrix form as follows [90]:

$$\{\tilde{\mathbf{m}}, \tilde{\Theta}\} = \arg \min_{\mathbf{m}, \Theta} \left\{ \|\mathbf{A}\mathcal{F}\mathbf{S}\mathbf{U}_{\Theta}\mathbf{m} - \mathbf{y}\|^2 \right\} \quad (3.6)$$

where \mathbf{U}_{Θ} denotes the rigid motion transformation matrix. The proposed elastic alignedSENSE (EAS) extends the approach in Eq. (3.6) to consider nonrigid deformations, referred to as \mathbf{T}_{Θ} . This is achieved by using a 2D FFD model, similar to that explained in Sections 2.3.5.1 and 2.3.5.2.

Thus, the proposed EAS reconstruction problem is formulated as follows:

$$\{\tilde{\mathbf{m}}, \tilde{\Theta}\} = \arg \min_{\mathbf{m}, \Theta} \left\{ \|\mathbf{A}\mathcal{F}\mathbf{S}\mathbf{T}_{\Theta}\mathbf{m} - \mathbf{y}\|^2 + \mathcal{R}_2(\mathbf{m}) + \mathcal{R}_3(\Theta) \right\} \quad (3.7)$$

where $\mathcal{R}_2(\mathbf{m})$ and $\mathcal{R}_3(\Theta)$ are regularization terms that stabilize the reconstruction: $\mathcal{R}_2(\mathbf{m})$ promotes removal of artifacts in the pattern image, whereas $\mathcal{R}_3(\Theta)$ favors smoothness in the temporal trajectory, since reconstructions may present some tremor. The specific expressions and further details for both regularization terms will be given in Subsection 3.2.1.

The joint problem in Eq. (3.7) is solved using an alternating fashion

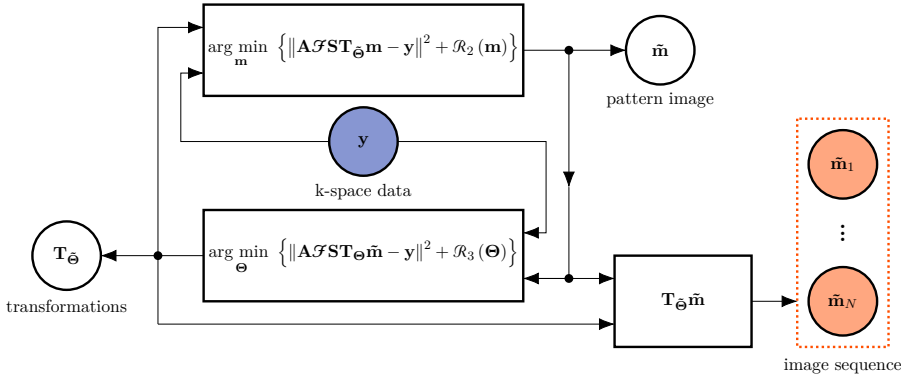


Figure 3.4: Scheme of the EAS reconstruction as an alternating minimization approach. If the transformations \mathbf{T}_Θ are assumed to be known, the best possible \mathbf{m} in terms of fidelity to the measured data \mathbf{y} can be obtained. Likewise, assuming \mathbf{m} to be known, the best possible \mathbf{T}_Θ can be obtained. The final image sequence is obtained by applying each of the transformations $\mathbf{T}_{\tilde{\Theta}_n}$ to the pattern image $\tilde{\mathbf{m}}$. Input to the reconstruction method is the blue shaded circle. Outputs are coloured in orange and enclosed by an orange dashed line rectangle.

by iteratively solving the two following sub-problems:

$$\tilde{\mathbf{m}} = \arg \min_{\mathbf{m}} \left\{ \|\mathbf{A} \mathcal{F} \mathbf{S} \mathbf{T}_\Theta \mathbf{m} - \mathbf{y}\|^2 + \mathcal{R}_2(\mathbf{m}) \right\} \quad (3.8a)$$

$$\tilde{\Theta} = \arg \min_{\Theta} \left\{ \|\mathbf{A} \mathcal{F} \mathbf{S} \mathbf{T}_\Theta \tilde{\mathbf{m}} - \mathbf{y}\|^2 + \mathcal{R}_3(\Theta) \right\} \quad (3.8b)$$

The first sub-problem (3.8a) will be referred to as *image sub-problem* — since its solution is a new image pattern—, whereas the second (3.8b), will be referred to as *deformation sub-problem*, since its solution is a new set of deformations.

The loop starts by solving the image sub-problem (Eq. (3.8a)), considering that there is no transformation, i.e., \mathbf{T}_Θ equals the identity, so that an initial pattern image \mathbf{m}_0 can be obtained. After that, the deformation sub-problem is fed with \mathbf{m}_0 and the loop can continue as expected (see Figure 3.4), until some stop criterion is achieved.

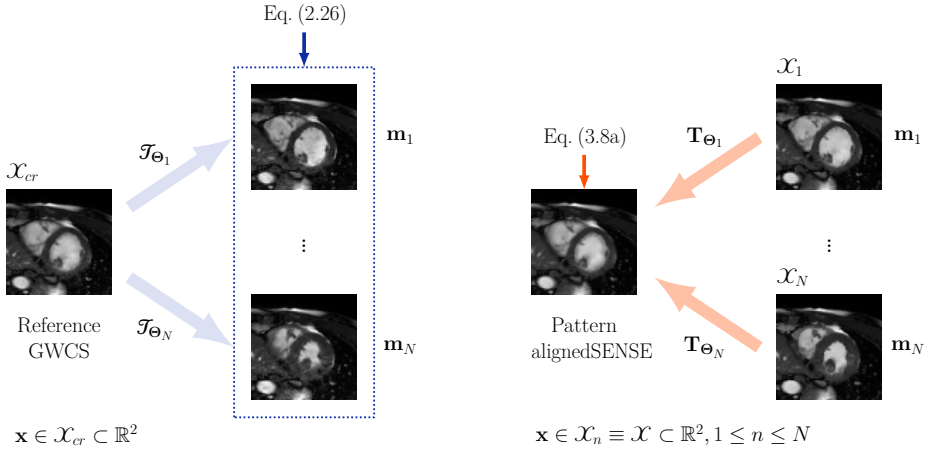


Figure 3.5: Scheme of spatial transformations in GWCS (left) and EAS (right) for 2D cardiac CINE MRI. Left: Points to be transformed $\mathbf{x} \in \mathcal{X}_{cr} \subset \mathbb{R}^2$ are defined on the common reference coordinate space. Right: Points to be transformed $\mathbf{x} \in \mathcal{X}_n \equiv \mathcal{X} \subset \mathbb{R}^2$, $1 \leq n \leq N$ are defined on each image coordinate space, which coincide for all images.

Notice that the registrations in GWCS and EAS, although quite similar in conception and notation, differ in two relevant elements:

1. Transformations are defined in opposite directions, as illustrated in Figure 3.5. In GWCS, the coordinate space $\mathcal{X}_{cr} \subset \mathbb{R}^2$ is defined in the common reference image and each frame \mathbf{m}_n ($1 \leq n \leq N$, being N the number of frames) is transformed so that it fits into such \mathcal{X}_{cr} , i.e., we calculate $\mathbf{m}_n(\mathcal{T}_{\theta_n}(\mathbf{x}))$ with $\mathbf{x} \in \mathcal{X}_{cr}$. Thus, in the optimization problem described in Eq. (2.29), we aim to find that $\mathbf{m}_p(\mathcal{T}_{\theta_p}(\mathbf{x})) \cong \mathbf{m}_q(\mathcal{T}_{\theta_q}(\mathbf{x}))$, with $p \neq q$. In the case of EAS, the coordinate space $\mathcal{X}_n \subset \mathbb{R}^2$ is defined in each frame \mathbf{m}_n —and coincides for all frames ($\mathcal{X}_n \equiv \mathcal{X}$, $1 \leq n \leq N$)—, so that each frame \mathbf{m}_n is a deformed version of the pattern image \mathbf{m} , i.e., $\mathbf{m}_n = \mathbf{m}(\mathbf{T}_{\theta_n}(\mathbf{x}))$. In summary, the transformations have their origin in the space in which the coordinate system is defined and the direction is the opposite of what “common sense” dictates. The reason of this is

because the transformation defined in that way makes the underlying interpolation process more convenient.

2. The common reference image in GWCS is the average of the registered images, following [91], while in EAS the reference arises as a result of the optimization sub-problem in Eq. (3.8a)¹, which is transformed to create the images of the final sequence, and does not necessarily correspond to any pre-selected cardiac phase.

It should be also pointed out that solving the whole EAS problem (Eq. (3.7)) can be challenging, specially when calculating the cost function and its gradient, due to the fact that both image and k-space domain terms may be mixed up. These calculations may become a bottleneck and degrade the performance of the reconstruction algorithm. Therefore, some details on this topic are provided in Appendix C.

3.2.1 Regularization terms in elastic alignedSENSE

Different strategies for the regularization terms in EAS have been tested. They can be divided in fixed regularization terms —which are governed by constant regularization parameters for the whole image— and variant regularization terms —in which the methodology described in 3.1 has been applied.

3.2.1.1 Fixed regularization terms in elastic alignedSENSE

The image sub-problem of EAS (Eq. 3.8a) is formulated, on one hand, as an ℓ_2 -problem in which $\mathcal{R}_2(\mathbf{m})$ is substituted by both spatial total variation (spTV) —Eq. (3.9a)— and the Laplacian operator —Eq. (3.9b)—. These two resulting ℓ_2 -problems have been solved by means of a conjugate gradient (CG) algorithm [89].

¹For simplicity in notation, we often denote $\mathbf{m}(\mathbf{T}_\Theta(\mathbf{x}))$ as $\mathbf{T}_\Theta\mathbf{m}$. Also note that, when we refer to a specific frame, we add a subindex to the previous expression, i.e., $\mathbf{T}_{\Theta_n}\mathbf{m}_n \equiv \mathbf{m}_n(\mathbf{T}_{\Theta_n}(\mathbf{x})) \equiv \mathbf{m}(\mathbf{T}_\Theta(\mathbf{x}, n))$.

On the other hand, the image sub-problem is also formulated as a ℓ_1 -problem where $\mathcal{R}_2(\mathbf{m})$ is substituted by both spatial FFT —Eq. (3.9c)— and Wavelet Transform operators —Eq. (3.9d)—. These two resulting ℓ_1 -problems, on the contrary, have been solved by using the Nesterov’s algorithm (NESTA) [92].

In summary, the four different regularization terms that have been tested for the image sub-problem can be expressed as follows:

$$\mathcal{R}_{2,1}(\mathbf{m}) = \lambda \|\nabla_{\mathbf{x}}\mathbf{m}\| \quad (3.9a)$$

$$\mathcal{R}_{2,2}(\mathbf{m}) = \lambda \|\nabla_{\mathbf{x}}^2\mathbf{m}\| \quad (3.9b)$$

$$\mathcal{R}_{2,3}(\mathbf{m}) = \lambda \|\mathcal{F}\mathbf{m}\|_{\ell_1} \quad (3.9c)$$

$$\mathcal{R}_{2,4}(\mathbf{m}) = \lambda \|\mathcal{W}\mathbf{m}\|_{\ell_1} \quad (3.9d)$$

where $\nabla_{\mathbf{x}}$ represents here the spTV operator, $\nabla_{\mathbf{x}}^2$ denotes the Laplacian operator, \mathcal{F} symbolizes the FFT and \mathcal{W} stands for the Wavelet Transform operator. The influence of the regularization term is controlled by the regularization parameter λ , the value of which must be determined in each case.

The regularization term $\mathcal{R}_3(\mathbf{m})$ in the deformation sub-problem of EAS (Eq. 3.8b) is related to both first and second order derivatives of transformation \mathbf{T}_{Θ} in both spatial and temporal dimensions. However, the spatial derivatives have not shown any perceptible effect on the reconstructions. Therefore, only the temporal derivatives are considered:

$$\mathcal{R}_3(\Theta) = \sum_{n=1}^N \sum_{\mathbf{x} \in \mathcal{X}} \left(\omega_1 \left\| \frac{\partial \mathbf{T}_{\Theta}(\mathbf{x}, t)}{\partial t} \right\|_{t=n}^2 + \omega_2 \left\| \frac{\partial^2 \mathbf{T}_{\Theta}(\mathbf{x}, t)}{\partial t^2} \right\|_{t=n}^2 \right) \quad (3.10)$$

where, ω_1 and ω_2 are regularization parameters to be set and derivatives are approximated by temporal finite differences. The deformation sub-problem has been solved by means of a nonlinear CG algorithm with backtracking

line search [93].

3.2.1.2 Variant regularization terms in elastic alignedSENSE

The formulation of EAS in Eq. (3.7) is modified in order to incorporate space-time variant regularization, as described in Section 3.1. To this end, the regularization parameters λ , ω_1 and ω_2 have been substituted— analogously to matrix \mathbf{W} in Section 3.1— by the diagonal weighting matrices $\mathbf{\Lambda}$, $\mathbf{\Omega}_1$ and $\mathbf{\Omega}_2$, respectively, as follows:

$$\{\tilde{\mathbf{m}}, \tilde{\Theta}\} = \arg \min_{\mathbf{m}, \Theta} \left\{ \|\mathbf{A}\mathcal{F}\mathbf{S}\mathbf{T}_{\Theta}\mathbf{m} - \mathbf{y}\|^2 + \|\mathbf{\Lambda}\Phi\mathbf{m}\|^2 + \mathcal{R}_4(\Theta) \right\} \quad (3.11a)$$

$$\mathcal{R}_4(\Theta) = \sum_{n=1}^N \sum_{\mathbf{x} \in \mathcal{X}} \left(\left\| \mathbf{\Omega}_1 \frac{\partial \mathbf{T}_{\Theta}(\mathbf{x}, t)}{\partial t} \right\|_{t=n}^2 + \left\| \mathbf{\Omega}_2 \frac{\partial^2 \mathbf{T}_{\Theta}(\mathbf{x}, t)}{\partial t^2} \right\|_{t=n}^2 \right) \quad (3.11b)$$

where Φ could be any of the operators defined in Eq. (3.9).

The version of EAS when displacement fields are used to leverage the regularization parameters will be referred as to EAS_{disp} , whereas it will be referred as to EAS_{vel} , when velocity fields are used. These two strategies have been used because they exploit the motion information in a more specific way than *Plateau* and therefore the latter has not been employed.

3.2.2 Combination of elastic alignedSESNE and groupwise motion-compensated compressed sensing

Elastic alignedSENSE may be a method on its own, but it may also be used as an initializer of methods with ME/MC, such as the GWCS approach (Figure 3.6). Recall from Eqs. (2.26) and (3.7) that less parameters are estimated in EAS with respect to GWCS, so it is expected that estimations may be more stable with EAS, at least in the first iterations. Therefore, a combination of EAS with GWCS is proposed (referred as to MIX) in an attempt to benefit from the advantages of each. EAS with fixed regulari-

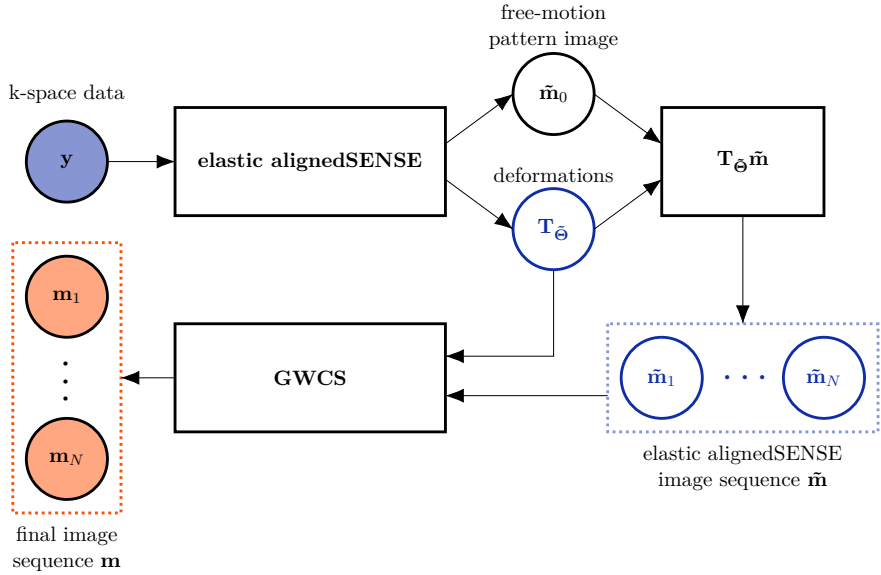


Figure 3.6: Scheme of the MIX reconstruction method as a combination of EAS phases followed by a GWCS phase. The output of EAS, $\tilde{\mathbf{m}}$ and $\mathbf{T}_{\tilde{\Theta}}$ (coloured with blue lines), is fed to GWCS. Since EAS provides directly a set of transformations $\mathbf{T}_{\tilde{\Theta}}$, that maps the pattern image \mathbf{m}_0 to each cardiac state, there is no need of the registration stage within GWCS. Thus, only the MC stage in GWCS is applied to obtain the final reconstruction. Input to the whole reconstruction method is the blue shaded circle. Outputs are coloured in orange and enclosed by an orange dashed line rectangle.

zation parameters as well as EAS with variant regularization parameters—namely, EAS_{disp} and EAS_{vel} —have been tested as initializers of GWCS. The resulting combinations of the different variants of EAS with GWCS will be referred as to MIX , MIX_{disp} and MIX_{vel} , respectively.

3.2.3 Radial extension of elastic alignedSENSE

So far, a Cartesian sampling scheme was always considered. As pointed out in Section 2.2.1, Cartesian sampling is significantly less robust to motion than radial sampling. However, it is simpler to handle, since no

gridding is needed and the efficient FFT algorithm can be directly applied to reconstruct the image, at least in the fully sample case. So, the radial alternative seems worth exploring.

The extension of EAS to radial trajectories is rather straightforward, since we only need to substitute the regular FFT for the non-uniform FFT (NUFFT) [94] in Eq. (3.7). The NUFFT was computed by using the existing implementation for GPU in [95] (gpuNUFFT).

$$\{\tilde{\mathbf{m}}, \tilde{\Theta}\} = \arg \min_{\mathbf{m}, \Theta} \left\{ \|\mathcal{G}\mathbf{T}_{\Theta}\mathbf{m} - \mathbf{y}\|^2 + \lambda \|\nabla_{\mathbf{x}}\mathbf{m}\|^2 + \mathcal{R}_3(\Theta) \right\} \quad (3.12)$$

where \mathcal{G} represents the gpuNUFFT operator just mentioned, that includes sensitivity coil maps operator as well as gridding, NUFFT and subsampling operations.

3.3 Experiments

3.3.1 Space-time variant weighted regularization

To test this method some experiments have been conducted for both 2D and 3D datasets, whose details will be given in subsequent sections.

The 2D datasets were retrospectively subsampled with the procedure described in [47] for different values of AF, whereas 3D datasets were retrospectively subsampled with the procedure described in Appendix A, with different values of AF and α , which controls the amount of subsampling in the center of k -space. Complex Gaussian noise has been also artificially added in k -space to these datasets by setting different values for the noise standard deviation, so that its effects in reconstructions can be analyzed.

Images have been reconstructed with sPICS (Eq. (2.25)), kt-SS (Eq. (2.24)) and with the three different approaches of weighted regularization described before: *Plateau*, weighted λ by displacement fields (W_{disp}) and

weighted λ by velocity fields (W_{vel}), respectively, Eqs. (3.2), (3.4) and (3.5). Both Signal-to-Error Ratio (SER) and High Frequency Signal-to-Error ratio (HFSER) [96] were calculated as image quality measurements. SER and HFSER are defined as given by Eqs. (3.13) and (3.14), respectively

$$SER = 10 \cdot \log \left(\frac{\|\mathbf{m}_{ref}\|^2}{\|\mathbf{m}_{ref} - \mathbf{m}_{rec}\|^2} \right) \quad (3.13)$$

$$HFSER = 10 \cdot \log \left(\frac{\|\text{LoG}(\mathbf{m}_{ref})\|^2}{\|\text{LoG}(\mathbf{m}_{ref}) - \text{LoG}(\mathbf{m}_{rec})\|^2} \right) \quad (3.14)$$

where \mathbf{m}_{ref} is the fully sampled image (reference), \mathbf{m}_{rec} is the reconstructed image, and LoG is a Laplacian of Gaussian filter that captures boundaries, with a kernel size of 7×7 pixels ($-3 \leq x \leq 3$, $-3 \leq y \leq 3$) and standard deviation of $\sigma = 1.5$:

$$\text{LoG}(x, y) = -\frac{1}{\pi\sigma^4} \left(1 - \frac{x^2 + y^2}{2\sigma^2} \right) e^{-\frac{x^2 + y^2}{2\sigma^2}} \quad (3.15)$$

For 2D experiments, quantitative cardiac function indicators have been also obtained, namely, end diastolic volume (EDV), end systolic volume (ESV), stroke volume (SV) and ejection fraction (EF). EDV and ESV were computed using Simpson's rule and manual segmentation with an in-house software for all the reconstructions using all regularization strategies. Afterwards, SV and EF were calculated as:

$$SV = EDV - ESV \quad (3.16)$$

$$EF = 100 \cdot \frac{SV}{EDV} \quad (3.17)$$

Since this chapter is focused on the importance of regularization, the selection of the parameter λ has received special attention. A methodology based on cross validation [97] has been applied. The details of the procedure are thoroughly described in Appendix B, where some parameters (namely,

the total number of datasets used in the cross validation procedure, K , the number of datasets used for the training group, P , the set of N tentative values of the regularization parameter λ and the similarity metric $V(\lambda)$ have to be set. In this case, $K = 7$ and $P = 4$ have been chosen for 2D experiments and $K = 5$ and $P = 4$ for the 3D experiments. For both 2D and 3D experiments, SER (Eq. (3.13)) has been chosen as similarity metric and twelve values equally space in a logarithmic scale in the range between 10^{-4} and 1 have been chosen as tentative values of λ . As for the methods in Eqs. (2.25) and (2.24) that are used to compare with, the parameters have been set $\lambda = \lambda_1 = \lambda_{opt}$ and $\lambda_2 = \lambda_1/10$, following the same criteria as in [8], and being λ_{opt} the value obtained by the procedure described in Appendix B.

It should be pointed out that 3D images are reconstructed in a per-slice basis, since the k-space visiting schemes are fully sampled in one direction, so 2D displacement fields have been used in both 2D and 3D experiments.

Coil sensitivity maps were obtained from separate SENSE reference scans in an arbitrary geometry. After the adaptation of the geometry of the reference scans to the geometry of the corresponding CINE scans, the sensitivity maps are estimated by dividing the individual coil images by the body coil images. Finally, the sensitivity maps are smoothed to remove undesired peaks and singularities.

3.3.1.1 2D experiments

2D Cartesian, fully sampled dynamic CINE BH gated acquisitions were performed on 7 healthy subjects in a 1.5 T Philips scanner with a balanced Steady State Free Precession (bSSFP) sequence. Some relevant parameters of the acquisitions include flip-angle 60° , $TR/TE = 3/1.5$ ms, spatial resolution 2×2 mm², slice thickness 8 mm, 20 cardiac phases, FOV 320×320 mm². They were afterwards retrospectively subsampled using a Gaussian variable-density random undersampling pattern along the phase

encoding direction [47] with different values of AF.

3.3.1.2 3D experiments

A 3D+t cardiac MR scan was performed on five swine in a 3 T Philips scanner with volumetric balanced Turbo Field Echo (bTFE) sequence. Some relevant parameters of the acquisition include flip-angle 30° , TR/TE = 1.95/0.976 ms, 20 cardiac phases. Reconstructed voxel size was $1.417 \times 1.417 \times 1.1 \text{ mm}^3$. Acquisitions were cardiac-triggered by means of a Peripheral Pulse Unit (PPU) located at the swine’s tail. Due to the physiology of these animals, respiratory motion in sedated swine is barely appreciated and causes no artifacts, so the acquisition did not make use of any additional hardware to deal with breathing issues. A 3D Cartesian sampling scheme has been used to avoid gridding operations. This sampling scheme is defined here as a general Cartesian sampling scheme with spiral ordering of samples and golden-angle step, whose details are given in Appendix A.

3.3.2 Elastic alignedSENSE

The 2D datasets from previous sections have also been used to test the EAS framework. Details follow.

3.3.2.1 Fixed regularization terms

The 2D datasets were retrospectively subsampled using the procedure in [47] for different values of AF. Afterwards, they were reconstructed using EAS with the four different alternatives for the regularization term in the image subproblem (Eqs. (3.9)).

The fully sampled reconstruction was used as a reference. HFSE and structural similarity index (SSIM) [98] were calculated for image quality assessment. To measure the quality of motion, we obtained displacement fields by registering the reconstructed sequence and the reference sequence; specifically, the n -th frame on the reconstructed sequence, is registered

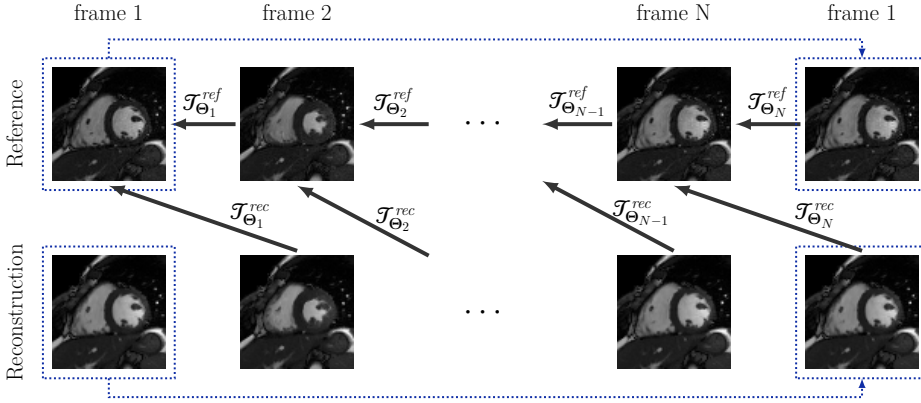


Figure 3.7: Scheme of the registration methods performed for motion quality assessment. Note that a periodic extension is considered (represented with dotted blue lines), so that the first frame is registered to the last one.

to the $(n - 1)$ -th frame on the reference² to obtain the displacement field $\mathbf{D}_{rec}(n)$ that results from transformation $\mathcal{T}_{\theta_n}^{rec}$, where the latter is calculated by using the motion estimation procedure described in Section 2.3.5.1 (see Figure 3.7). Similarly, each frame in the reference sequence was registered to its previous frame in the reference (once again, with periodic extension) to obtain the displacement field $\mathbf{D}_{ref}(n)$. Finally, the RMSE value between both reference and reconstruction displacement fields is calculated (Eq. 3.18).

$$RMSE = \sqrt{\frac{\sum_{n=1}^N \|\mathbf{D}_{rec}(n) - \mathbf{D}_{ref}(n)\|_F^2}{N}} \quad (3.18)$$

with $\|\cdot\|_F$ the Frobenius norm, considering $\mathbf{D}_{ref}(n)$ a matrix with dimensions $|\mathcal{X}| \times 2$, with \mathcal{X} the set of reconstructed pixels and $|\cdot|$ the cardinality of a set.

The temporal profiles along radial directions separated 45 degrees were concatenated to form the image \mathbf{I}_{ncc} (Figure 3.8). The normalized crossed

²Actually, as indicated in Figure 3.7, we assume periodicity in the cardiac cycle, so $n = \text{mod}(m, N)$, with $2 \leq m \leq N + 1$, and N is the number of frames in the sequence.

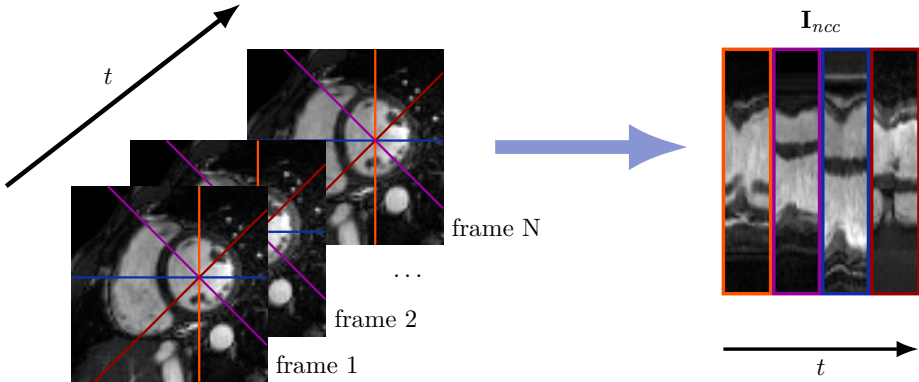


Figure 3.8: Temporal profiles along radial directions every 45 degrees, (the center of which coincide with the center of the left ventricle) are concatenated to form an image. The NCC between such images is used to assess motion quality.

correlation (NCC) between such images from both the reconstructed and the reference datasets was also computed as a quality measurement. NCC is defined as

$$NCC = \frac{\sum_{\mathbf{x} \in \mathcal{X}} \left(\mathbf{I}_{ncc}^{ref} - \overline{\mathbf{I}_{ncc}^{ref}} \right) \left(\mathbf{I}_{ncc}^{rec} - \overline{\mathbf{I}_{ncc}^{rec}} \right)}{\sqrt{\sum_{\mathbf{x} \in \mathcal{X}} \left(\mathbf{I}_{ncc}^{ref} - \overline{\mathbf{I}_{ncc}^{ref}} \right)^2 \sum_{\mathbf{x} \in \mathcal{X}} \left(\mathbf{I}_{ncc}^{rec} - \overline{\mathbf{I}_{ncc}^{rec}} \right)^2}} \quad (3.19)$$

where \mathbf{I}_{ncc}^{ref} and \mathbf{I}_{ncc}^{rec} stand for the \mathbf{I}_{ncc} images obtained from the reference image and the reconstruction, with spatial average values $\overline{\mathbf{I}_{ncc}^{ref}}$ and $\overline{\mathbf{I}_{ncc}^{rec}}$, respectively. Since the temporal evolution is accounted for in NCC, this parameter is also useful for motion quality assessment.

The λ value for each case in Eqs. (3.9), as well as the values of ω_i ($i = 1, 2$) in Eq. (3.10) have been set by using the procedure described in Appendix B. The parameters of the procedure have been chosen as follows: $K = 7$, $P = 4$ and HFSE as the similarity metric. λ and ω_i ($i = 1, 2$) have been grouped into vector $\boldsymbol{\mu} = (\lambda, \omega_1, \omega_2)$ and the exploring grid has been established by setting six tentative values for λ ranging in logarithmic

scale from 1 to 10^{-3} , and five tentative values in logarithmic scale from 1 to 10^{-4} for ω_i ($i = 1, 2$).

3.3.2.2 Variant regularization terms

Similarly to previous experiments, the 2D datasets were retrospectively subsampled and reconstructed by using the two types of EAS with variant regularization terms, namely EAS_{disp} (Eqs. (3.11) and (3.4)) and EAS_{vel} (Eqs. (3.11) and (3.5)). For comparisons, they have also been reconstructed using $sPICS$ (Eq. (2.25)), $GWCS$ (Eq. (2.26)), $kt-SS$ (Eq. (2.24)), W_{disp} (Eqs. (3.1) and (3.4)) and W_{vel} (Eqs. (3.1) and (3.5)).

In this case, two values have to be set for the regularization parameters, $\boldsymbol{\mu} = (\lambda, \omega_1, \omega_2)$, namely $\boldsymbol{\mu}_{st}$ and $\boldsymbol{\mu}_{dyn}$. To do this, the procedure described in Appendix B have been used with the same parameters as in the previous subsection. The difference is that, in order to set the $\boldsymbol{\mu}_{st}$, we have used HFSE, since it is more focused on intensity levels and, therefore, is more suitable for static regions. As for $\boldsymbol{\mu}_{dyn}$, we have used RMSE, since it is more focused in displacement fields, so that it is more suitable for dynamic regions.

Using the fully sampled reconstruction as a reference, HFSE, SSIM, RMSE between displacement fields —obtained as in the previous section— as well as NCC have been computed to measure performance.

Moreover, for this type of regularization we have used an additional quality metric, which is based on landmark distance. Specifically, we have used four frames, including diastole and systole as well as two intermediate frames. We have manually drawn several landmarks in three different slices—in basal, medial and apical regions of the heart— (see Figure 3.9). The process has been carried out twice and coordinates have been averaged to avoid bias. The RMSE between the landmarks obtained in both reconstructed and reference images has been calculated.

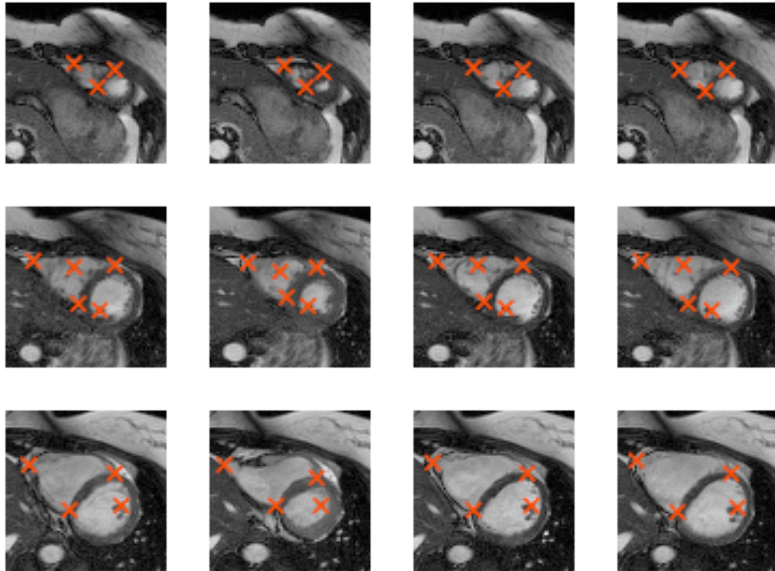


Figure 3.9: Example of landmarks for motion assessment.

3.3.2.3 Combination of elastic alignedSENSE and groupwise motion-compensated compressed sensing

The 2D datasets were retrospectively subsampled and reconstructed by using MIX, MIX_{disp} and MIX_{vel} methods. Indeed, we have tested to initialize GWCS with one iteration of each variant of EAS —i.e., finding one solution to the image and the deformation EAS sub-problems— and two iterations as well —to solve twice each image and deformation EAS sub-problems—. These two possibilities will be denoted by a superscript MIX^n , where n indicates the number of EAS iterations performed before the GWCS stage. The resulting reconstructions were compared with GWCS and EAS. HFSE, SSIM, NCC and RMSE were computed as both image and motion quality assessment.

3.3.2.4 Radial extension of elastic alignedSENSE

2D whole heart single BH acquisitions with golden radial trajectory and 32-element cardiac coil were performed on 7 subjects on a 1.5 T Philips scanner with bSSFP sequence. Some other parameters include TR/TE = 2.9 ms/1.44 ms, flip-angle 60°, spatial resolution $2 \times 2 \text{ mm}^2$, slice thickness 8 mm and FOV $320 \times 320 \text{ mm}^2$. Between 256 and 280 radial profiles, depending on the subject, were acquired per slice during a single cardiac cycle with ECG triggering.

Datasets were retrospectively reconstructed by using EAS, with 16 cardiac phases including the maximum of the spokes available per frame, which results in an equivalent temporal resolution of 46.4 ms. In this case, there is no availability of ground truth to compare with. Thus, the regularization parameters in Eqs. (3.12) and (3.10) could not be set by applying the method described in Appendix B. Therefore, some parameter sweeps for λ and ω_i ($i = 1, 2$) were performed. Specifically, the parameters varied within the intervals $\lambda \in [10^{-7}, 10^{-4}]$, $\omega_1 \in [0, 5 \cdot 10^3]$ and $\omega_2 \in [0, 5 \cdot 10^4]$. The resulting reconstructions were visually inspected and the parameters were set accordingly. Furthermore, this parameter sweeping revealed that the component of $\mathcal{R}_3(\Theta)$ weighted by ω_1 (see Eq. (3.10)) had no perceptible effect in the reconstructions and therefore was discarded for all the subsequent experiments.

Variant regularization parameters, both weighting by displacement and by velocity fields, were also tested for the radial extension of EAS. From the values for the regularization parameters obtained in the previous experiments, $\mu_0 = (\lambda_0, \omega_{20})$, the variation interval for $\mu \in [\mu_{dyn}, \mu_{st}]$ was set to $\mu \in [\mu_0/K_1, \mu_0 \cdot K_2]$, with $(K_1, K_2) = \{(10, 10), (1, 10), (10, 1)\}$.

Finally, the datasets were also reconstructed with *iGRASP*, *GWCS* and *MIX* for comparison purposes. The regularization parameter λ in *iGRASP* was set to 0.02 as the authors specify in [79]. For *GWCS* the regularization parameter λ in the MC steps, was set to 0.007 after performing some sweeps

for λ in the range $[10^{-3}, 10^{-1}]$. For the MIX methods, the parameters were the same of *EAS* and *GWCS* when they act independently.

The reconstructions in the experiments described in all Section 3.3 were performed using Matlab R2017b (The MathWorks, Natick, MA) on a Virtual Machine (VM) with two processors (Intel[®] Xeon[®] E5-2697 v4 @ 2.30 GHz), with a total of 35 cores (2 threads per core) and 500 GB RAM. The GPU executions for computing the *gpuNUFFT* needed in the experiments that make use of radial trajectories were performed in a NVIDIA Quadro RTX5000 device by using Matlab CUDA capabilities.

4.1 Space-time variant weighted regularization

4.1.1 2D Results

Figure 4.1 show boxplots of SER and HFSEr parameterized by R for all the reconstructions on the 2D datasets using the five regularization strategies and reveals that motion-weighted regularization schemes provide higher figures for higher values of R . Mann-Whitney U-tests have been conducted between SER and HFSEr distributions for reconstructions with $R = 20$, finding no significant differences. Despite these differences are not statistically significant (at both $p < 0.05$ and $p < 0.01$) it can indeed be observed some artifacts in the motion of papillary muscles, but this motion seems more natural in reconstructions using W_{disp} . Error images shown in Figure 4.3 reveal that the error is higher in the left-ventricle myocardium and in the apex.

Regarding functional measurements, Figure 4.2 show Bland-Altman plots for EF calculated on the reconstructions using the five strategies of regularization for $R = 5$. It reports agreement between them, but a bias in measurements can also be observed as a function of R . The resulting EF values (mean \pm standard deviation) and their p-values are shown in Table 4.1 for two different values of R . Nevertheless, those p-values

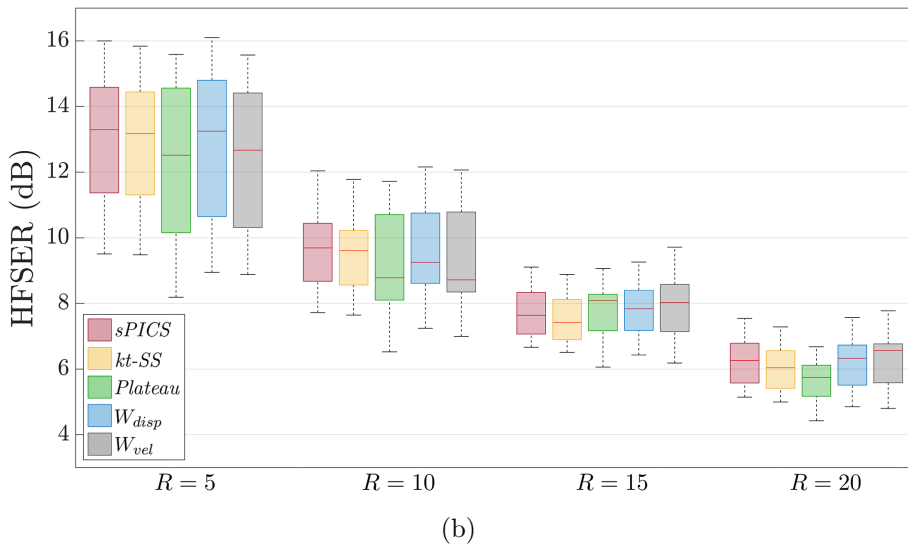
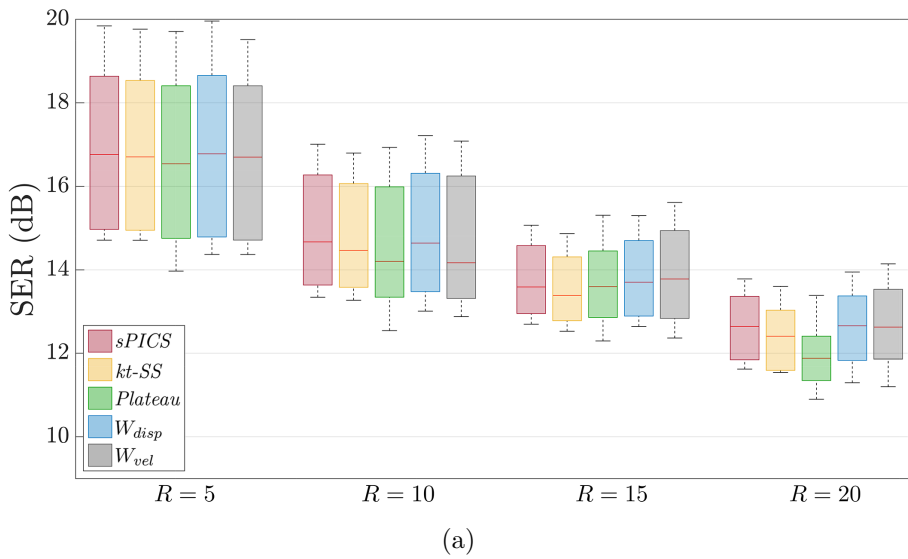


Figure 4.1: SER (a) and HF SER (b) values of all reconstructions on 2D datasets for the five regularization strategies (*sPICS*, *kt-SS*, *Plateau*, W_{disp} and W_{vel}), using Cartesian subsampling and different values of R .

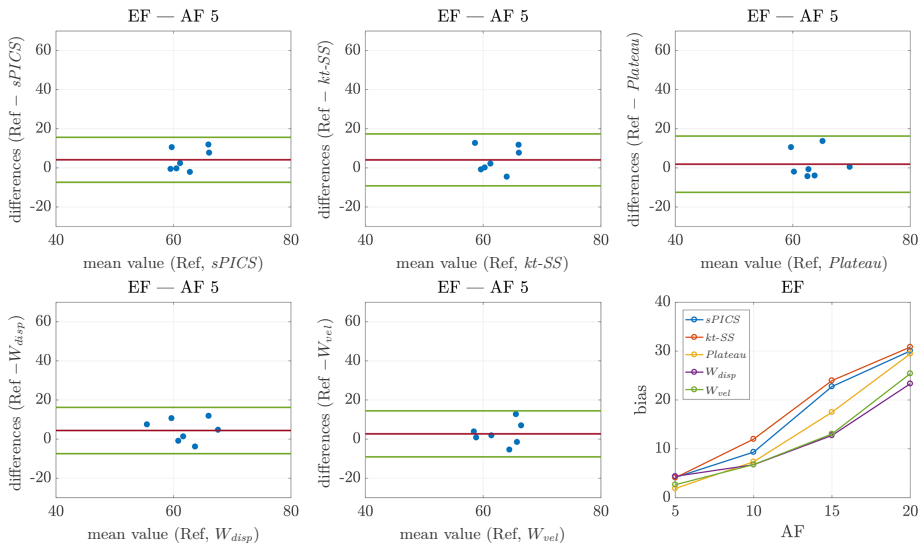


Figure 4.2: Bland-Altman plots for ejection fraction (EF) for all the the regularization strategies ($sPICS$, $kt-SS$, $Plateau$, W_{disp} and W_{vel}) on 2D datasets using Cartesian trajectories and $R = 5$. The observed bias is also represented parameterized by the parameter R .

in Table 4.1 reveal that there are not significant differences ($p > 0.05$) in EF between the reference value obtained in the fully sampled image and those obtained in reconstructions by using all the regularizations strategies when low values of R are used. Significant differences ($p < 0.05$) appear when R increases, although those space-time variant regularization strategies (namely, W_{disp} and W_{vel}) give rise to higher p-values which are not significant at a lower level value ($p < 0.01$). The positive sign of the bias means that the regularization strategies provide lower values than those of the ground truth. This being the case, it can be inferred that there is a loss of movement in the reconstructed images. However, the figure shows that regularization strategies with variant parameters (and, specifically, that in Eq. (3.4)) preserve heart movement better than those with a single and/or invariant regularization parameter (Eqs. (2.25) and (2.24)).

Table 4.1: EF values (mean value \pm standard deviation) calculated in the 2D reconstructions using all the regularization strategies (*sPICS*, *kt-SS*, *Plateau*, W_{disp} and W_{vel}) for $R = 5$ and $R = 10$. The EF reference value, calculated in the fully sampled image, is shown for comparison. p-Values between EF calculated in fully sampled image and reconstructed images are also shown. p-Values below the significance level 0.05 are boldfaced.

Strategy	$R = 5$		$R = 10$	
	EF	p-value	EF	p-value
<i>sPICS</i>	60.21 ± 2.92	0.1282	55.02 ± 4.65	0.0006
<i>kt-SS</i>	60.27 ± 4.16	0.1282	52.36 ± 5.63	0.0006
<i>Plateau</i>	62.46 ± 4.97	0.6200	57.00 ± 3.69	0.0041
W_{disp}	59.97 ± 5.19	0.2593	57.60 ± 4.70	0.0175
W_{vel}	61.69 ± 4.08	0.3829	57.67 ± 4.44	0.0262
Reference	64.35 ± 4.87			

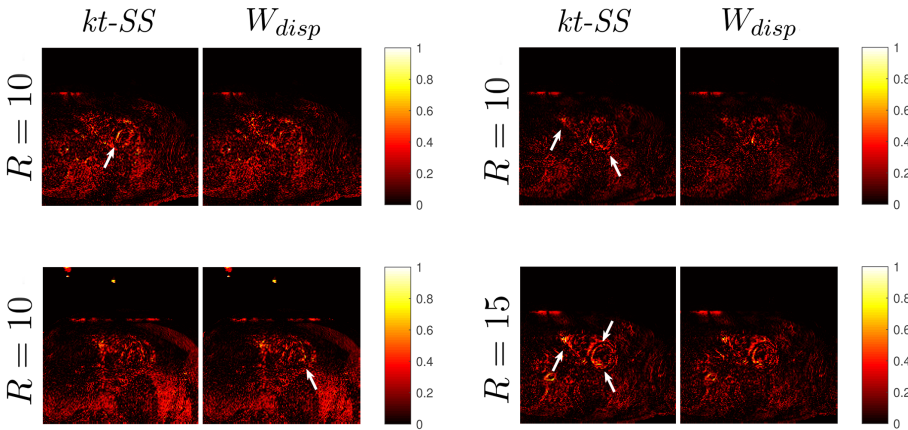
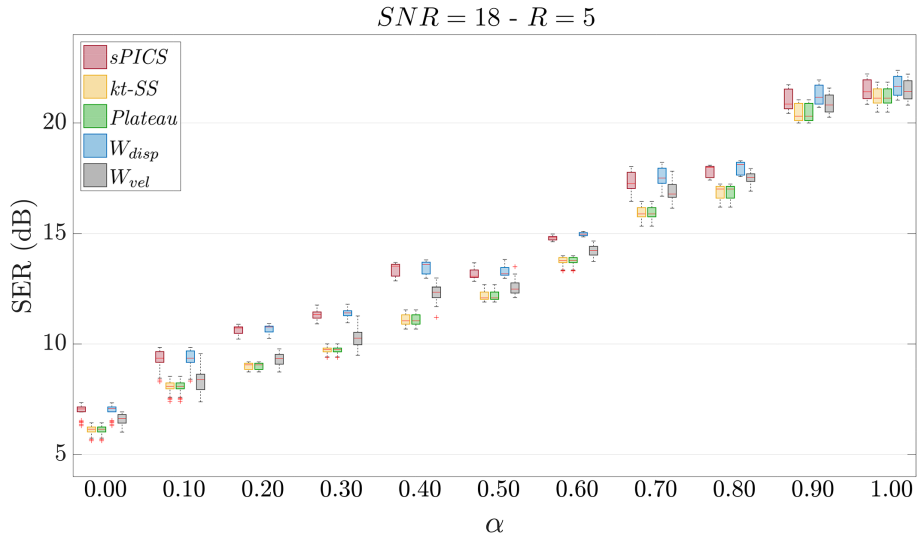


Figure 4.3: Normalized error images between reference and reconstructions on 2D datasets subjects with different values of R using *kt-SS* and W_{disp} strategies. White arrows point at significant locations where error is higher.

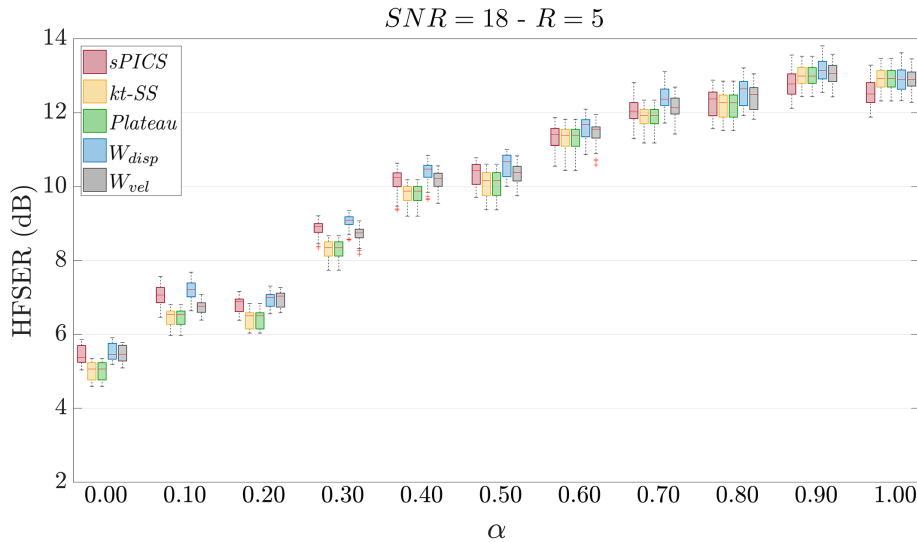
4.1.2 3D Results

Figures 4.4 and 4.5 show boxplots of SER and HFSER parameterized by α , which controls the amount of subsampling in the center of k-space (see Appendix A), for all the reconstructions on the 3D datasets using the five regularization strategies for a selected value of $SNR = 18$ (recall from Section 3.3.1 how this value is set up) and $R = 5$ and $R = 20$, respectively. These results reveal that reconstructions with higher values of SER and HFSER are obtained when α is close to —albeit not necessarily equal to— 1. Differences between methods are more notable when R increases. *sPICS* and W_{disp} regularization strategies give rise to reconstructions with higher SER and HFSER values than the other three regularization strategies. However, between these two strategies there are not significant differences in terms of SER and HFSER (Tables 4.2 and 4.3), which is a result that supports the proposed space-time variant weighted regularization method, since λ_{opt} was chosen, as described in the Appendix B, to maximize SER, so the method with λ_{opt} is acting in this experiment as a SER benchmark. Nevertheless, W_{disp} strategy produces reconstructions with more natural movement, especially in papillary muscles, than the other strategies. For easier reading, several examples have been included in Figure 4.7 that reveal higher and more structured error¹ values in myocardium in *sPICS* reconstructions than those using W_{disp} . This result is in line with the fact that SER is limited when used to quantify image quality perception and, specially, to measure the amount of movement present in a dynamic image. Therefore, the selected optimal value λ_{opt} may be higher than necessary, so that images tend to be overregularized. HFSER, on the other hand, does not seem to provide additional information to these experiments. As for the other three methods, they do show significant differences with respect to W_{disp} , which, again, supports this proposal.

¹Structured errors similar to the original signal are not desirable and far from the ideal case, which would be unstructured noise (ideally, white Gaussian noise).

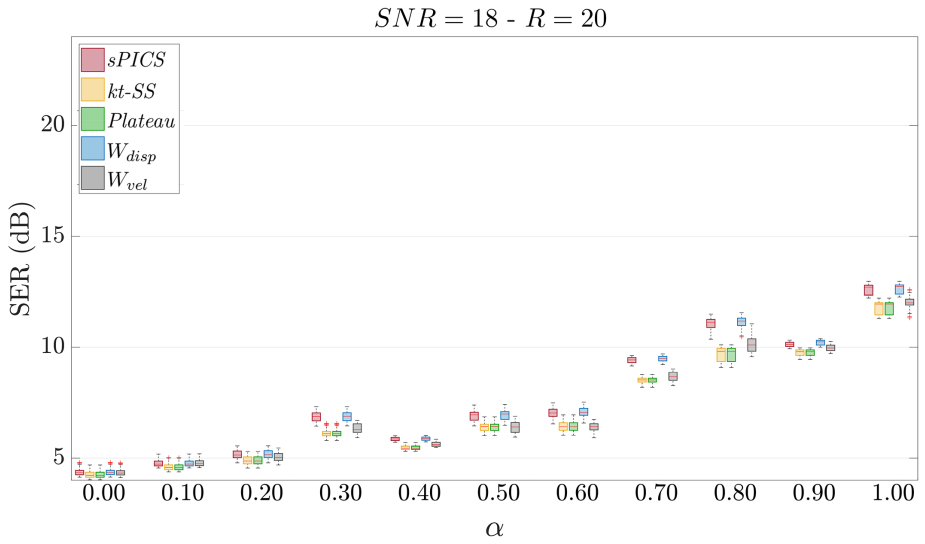


(a)

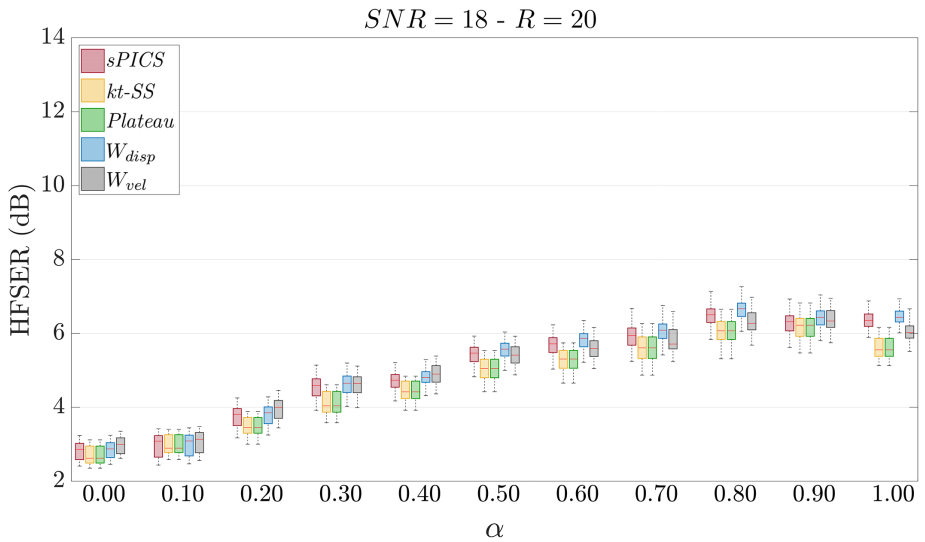


(b)

Figure 4.4: SER (a) and HFSER (b) values of all reconstructions on 3D datasets for the five regularization strategies ($sPICS$, $kt-SS$, $Plateau$, W_{disp} and W_{vel}), different values of α , $R = 5$ and $SNR = 18$.



(a)



(b)

Figure 4.5: SER (a) and HFSEr (b) values of all reconstructions on 3D datasets for the five regularization strategies ($sPICS$, $kt-SS$, $Plateau$, W_{disp} and W_{vel}), different values of α , $R = 20$ and $SNR = 18$.

Table 4.2: p-values of SER distributions for reconstructions on 3D datasets using all regularization strategies ($sPICS$, $kt-SS$, $Plateau$, W_{disp} and W_{vel}) with $R = 20$ and (a) $\alpha = 0.7$ and (b) $\alpha = 1$. p-Values below the significance level 0.05 are boldfaced.

	$sPICS$	$kt-SS$	$Plateau$	W_{disp}
$kt-SS$	0.0000			
$Plateau$	0.0000	1.0000		
W_{disp}	0.0877	0.0000	0.0000	
W_{vel}	0.0000	0.0056	0.0056	0.0000

(a)

	$sPICS$	$kt-SS$	$Plateau$	W_{disp}
$kt-SS$	0.0000			
$Plateau$	0.0000	1.0000		
W_{disp}	0.3329	0.0000	0.0000	
W_{vel}	0.0000	0.0339	0.0339	0.0000

(b)

Table 4.3: p-values of HF SER distributions for reconstructions on 3D datasets using all regularization strategies ($sPICS$, $kt-SS$, $Plateau$, W_{disp} and W_{vel}) with $R = 20$ and (a) $\alpha = 0.7$ and (b) $\alpha = 1$. p-Values below the significance level 0.05 are boldfaced.

	$sPICS$	$kt-SS$	$Plateau$	W_{disp}
$kt-SS$	0.0040			
$Plateau$	0.0040	1.0000		
W_{disp}	0.1120	0.0000	0.0000	
W_{vel}	0.2707	0.0351	0.0351	0.0199

(a)

	$sPICS$	$kt-SS$	$Plateau$	W_{disp}
$kt-SS$	0.0000			
$Plateau$	0.0000	1.0000		
W_{disp}	0.1537	0.0000	0.0000	
W_{vel}	0.0000	0.0000	0.0000	0.0000

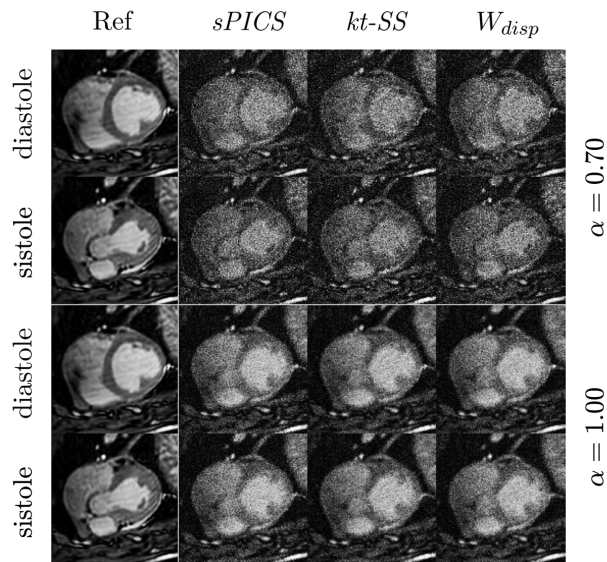
(b)

These experiments also allowed us to study the effect of noise in the different regularization strategies. In Figure 4.6a it can be observed that, for the same value of SNR and R , reconstructed images with $\alpha = 1$ in systole and diastole are very similar to each other. However, reconstructed images with $\alpha = 0.7$ differ notably. Additionally, it can be observed in reconstructed images that those with $\alpha = 1$ seem to show step-wise transitions while images with $\alpha = 0.7$ move seamlessly along the cardiac cycle. It can also be noticed that the accumulated error is more structured when $\alpha = 1$ than for $\alpha = 0.7$.

In Figures 4.6 we show a comparison between reconstructions of the systole and the diastole time instants on 3D datasets for three different regularization strategies ($sPICS$, $kt-SS$ and W_{disp}), two different values of α (0.7 and 1), $R = 5$ and with two low levels of SNR (0 and 6 dB, respectively). For simplicity, only W_{disp} strategy has been compared with the other reported regularization strategies, since the former provides the best reconstructions (Figures 4.4 and 4.5) in the motion-weighted strategies. It can be observed that in figure 4.6b, with a higher SNR, differences are hardly appreciated in terms of quality of motion although the error images maintain a higher structure for $\alpha = 1$. This evidence highlights that $\alpha = 1$ gives rise to images with less natural movement in the presence of noise, even though they obtain higher SER and HFSER values. Thus, in low signal to noise ratio scenarios, it would be preferable to choose an intermediate value of α close to 0.7, since heart movement is better preserved and noise can be eliminated by using tailored techniques.

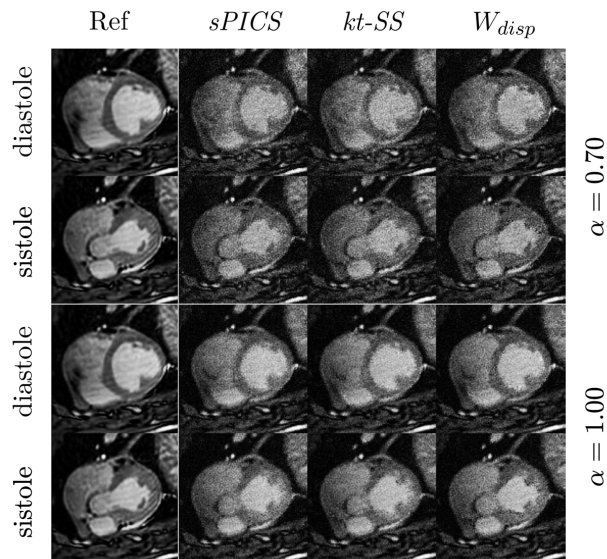
Figure 4.7 shows normalized error images for representative cases between reference and reconstructions on 3D datasets using two different regularization strategies ($sPICS$ and W_{disp}), $SNR = 18$, $\alpha = 1$ and different values of R (10 and 15).

As mentioned in previous sections, the space-time variant weighted regularized methods involve two steps: (1) initial reconstruction and (2) second reconstruction using a variant regularization term derived from



$SNR = 0 - R = 5$

(a)



$SNR = 6 - R = 5$

(b)

Figure 4.6: Fully sampled image (Ref) compared to reconstructions on 3D datasets with $R = 5$ and two different values of α , using *sPICS*, *kt-SS* and W_{disp} , and $SNR = 0$ (a) and $SNR = 6$ (b).

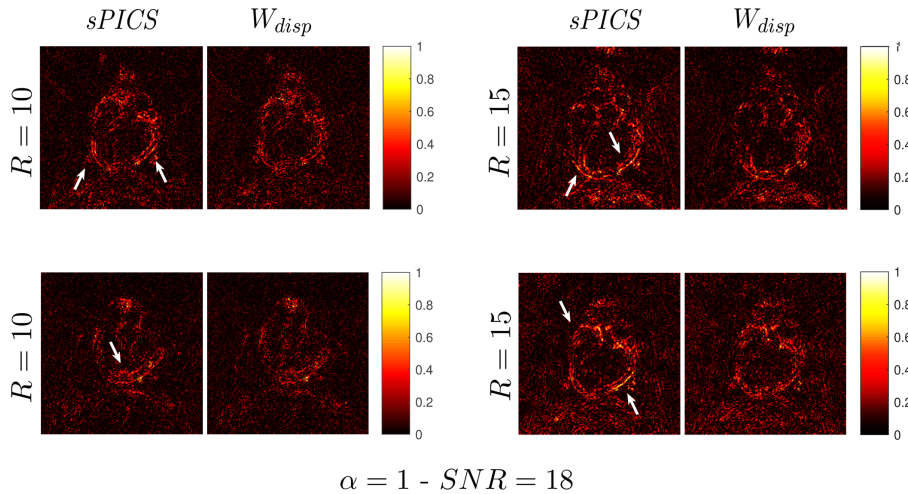


Figure 4.7: Normalized error images between reference and reconstructions on 3D datasets with different values of R using $sPICS$ and W_{disp} strategies, $\alpha = 1$ and $SNR = 18$. White arrows point at significant locations where error is higher.

the motion fields obtained from step (1). It is indeed more critical to have errors in step (1). At this step, errors arise due to either over- or under-regularization. Over-regularization gives rise to images with less artifacts (which is desirable) but more static (which is not desirable), while under-regularization is accompanied by more artifacts but better motion preservation. At step (2), artifacts may hinder motion estimation, but this estimation will never be corrected if motion is lost at step (1). Therefore, it is critical not to over-regularize in step (1). Under-regularization in step (1) may lead to worse motion estimates in step (2) but, since motion information is solely used to leverage temporal differences, the method would never introduce spurious movement, although it may give rise to non-optimal regularization in those specific areas where motion is incorrectly assessed. This sort of remaining artifacts, however, may be smoothed by tailored techniques. Therefore, it should be pointed out the importance of the procedure to select the parameter λ and develop a method to select it automatically for the step (1).

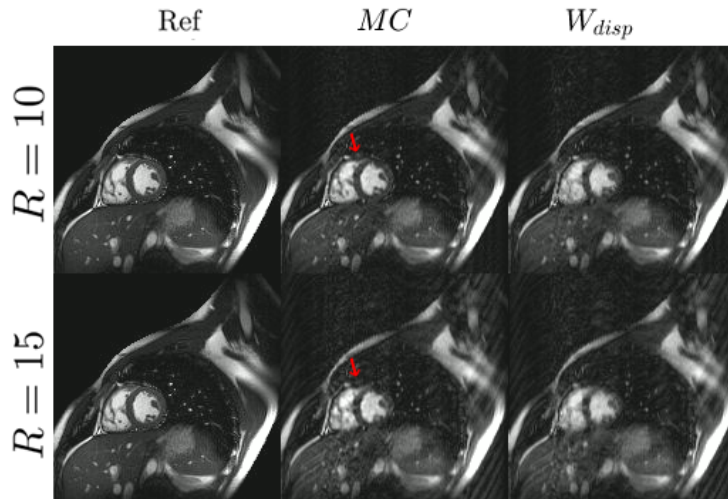
The main limitation of using Eq. (3.4) is the need to estimate movement from a prior reconstruction, making the whole reconstruction process longer. However the development of high performance implementations of the algorithms on GPUs drastically reduces these reconstructions times. As a matter of fact, this information has been incorporated in the reconstruction pipeline as well [11, 50]. Nevertheless, as previously stated, errors in motion field estimation may be propagated to the final reconstruction so robustness to this sort of mismatch is of importance. This may be the case in 2D imaging of the apical and basal slices, where structures come in and out of the planes along the cardiac cycle. To illustrate this, one of the human images has been sampled with a pseudorandom Cartesian scheme ($R = 10$) and has been reconstructed both with the MC-method described in [50] and with the method here proposed. It can be observed in Figure 4.8a that the MC algorithm introduces spurious deformations in the lung/right ventricle area (pointed with arrows). Interestingly, the rounded shape of the right ventricle is preserved when W_{disp} algorithm is used instead. In Figure 4.8b, a part of the myocardium has been marked with colored lines to highlight this fact. As observed, the method proposed in this chapter seems more robust when model mismatches are observed.

According to this evidence, complementarity between these two methods is worth exploring. This could be done by setting λ as a function of the residual motion observed in the (ideally) motion compensated images.

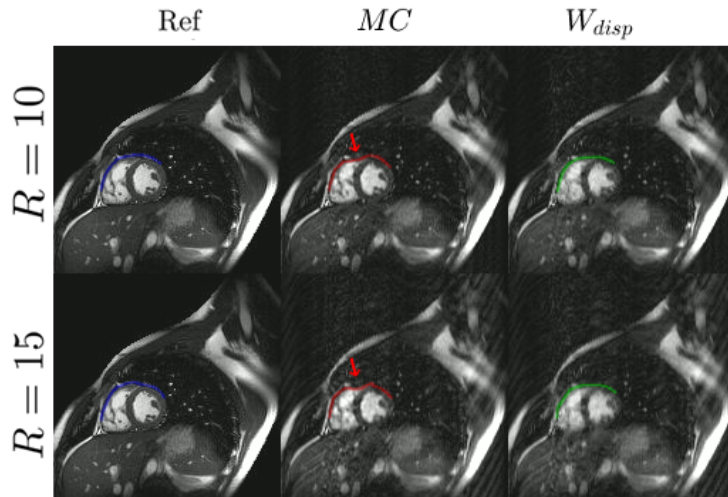
4.2 Elastic alignedSENSE

4.2.1 Fixed regularization terms

Figure 4.9 shows HFSE (a), SSIM (b), NCC (c) and RMSE (d) averaged values across all slices and volunteers, parameterized by R , for the reconstructions of the 2D datasets by applying EAS with the four different operators for the regularization term in the EAS image sub-problem de-



(a)



(b)

Figure 4.8: Results on real data, using 2D Cartesian pseudorandom undersampling with acceleration factors (R) of 10 (top row) and 15 (bottom row). Left column, fully sampled images of reference (Ref); center column, reconstructed images using a motion compensation algorithm (MC); right column, reconstructed images using displacement fields to leverage the regularization parameter (W_{disp}). Red arrows point areas with spurious deformation. In (b) the same images as in (a) are represented, but the myocardium is marked with coloured lines to highlight spurious deformations.

fined in Eq. (3.9). The average execution time needed for reconstructing one slice is also provided in Figure 4.9e. Tables 4.4–4.6 show p-values for comparisons with the Mann-Whitney test for every pair of operators on samples of HFSE (Table 4.4), RMSE (Table 4.5) and average running time for reconstructing one slice (Table 4.6) for three values of AF, namely $R = 2$, $R = 8$ and $R = 14$.

As it can be seen in Figure 4.9, the wavelet transform operator provides, generally speaking, worse results compared with the other three operators. Furthermore, it has also presented some convergence problems when reconstructing some slices in the whole dataset. In contrast, the remaining operators provide very similar values to each other for the four quality measures and there are hardly any differences among them, a statement that is supported by the p-values provided in Tables 4.4 and 4.5 ($p > 0.05$). Nevertheless, Table 4.6 presents some significative differences ($p < 0.05$) in the average execution times needed for reconstructing one slice, essentially between spTV operator and the other three. According to Figure 4.9e, spTV regularization operator reveals itself as the fastest and needs between twice and three times less time to reconstruct one slice, compared to the others. Therefore, this strategy seems the one to be preferred, since it offers similar quality in both image and motion to Laplacian or FFT operators, but needing less running time, besides that it entails less computational complexity.

4.2.2 Variant regularization terms

Figure 4.10 displays systole and diastole frames of the reconstructions of the 2D datasets by applying EAS with both fixed (EAS) and variant regularization terms (EAS_{disp} and EAS_{vel}), for a representative case and $R = 8$. The selected operator for the EAS image sub-problem regularization term is spTV in all of these three cases, due to the results obtained in the previous subsection. Two temporal profiles corresponding to a vertical and

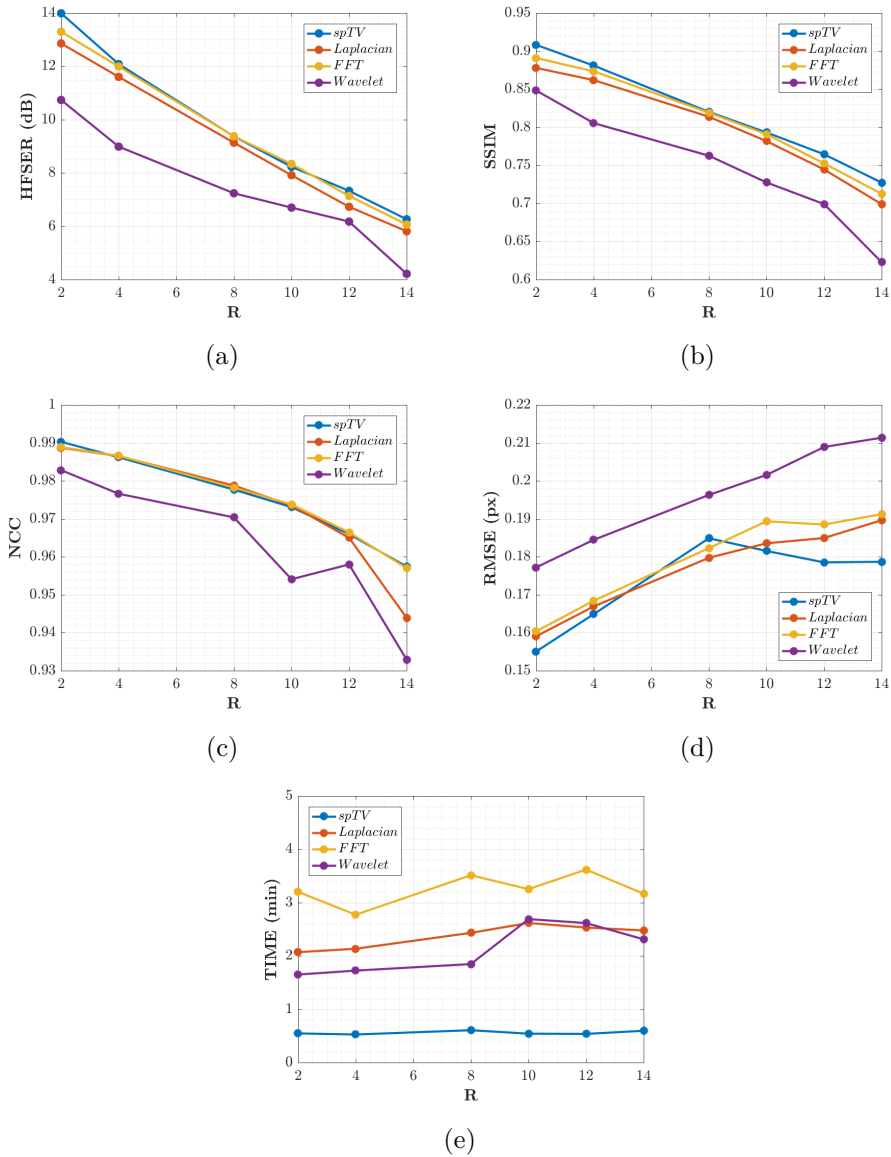


Figure 4.9: Results for EAS reconstructions with the four different regularization operators defined in Eq. (3.9) for the EAS image sub-problem. Averaged values across slices and volunteers for HFSE (a), SSIM (b), NCC (c) RMSE (d) and the average running time needed to reconstruct one slice (e) are provided for different values of R .

Table 4.4: p-Values of the Mann-Whitney test on samples of HFSER for reconstructions using EAS with the four different regularization operators defined in Eq. (3.9) for the EAS image sub-problem and different values of AF: $R = 2$ (a), $R = 8$ (b) and $R = 14$ (c). p-Values below the significance level 0.05 are boldfaced.

	<i>spTV</i>	<i>Laplacian</i>	<i>FFT</i>		<i>spTV</i>	<i>Laplacian</i>	<i>FFT</i>
<i>Laplacian</i>	0.1007			<i>Laplacian</i>	0.5271		
<i>FFT</i>	0.1214	0.2556		<i>FFT</i>	0.9264	0.5042	
<i>Wavelet</i>	0.0211	0.0491	0.0471	<i>Wavelet</i>	0.0121	0.0082	0.0100

(a)

(b)

	<i>spTV</i>	<i>Laplacian</i>	<i>FFT</i>
<i>Laplacian</i>	0.2556		
<i>FFT</i>	0.2892	0.5225	
<i>Wavelet</i>	0.0036	0.0325	0.0133

(c)

Table 4.5: p-Values of the Mann-Whitney test on samples of HFSER for reconstructions using EAS with the four different regularization operators defined in Eq. (3.9) for the EAS image sub-problem and different values of AF: $R = 2$ (a), $R = 8$ (b) and $R = 14$ (c).

	<i>spTV</i>	<i>Laplacian</i>	<i>FFT</i>		<i>spTV</i>	<i>Laplacian</i>	<i>FFT</i>
<i>Laplacian</i>	0.5271			<i>Laplacian</i>	0.6340		
<i>FFT</i>	0.5042	0.9887		<i>FFT</i>	0.8091	0.8201	
<i>Wavelet</i>	0.2191	0.2320	0.2738	<i>Wavelet</i>	0.4691	0.3722	0.4288

(a)

(b)

	<i>spTV</i>	<i>Laplacian</i>	<i>FFT</i>
<i>Laplacian</i>	0.2996		
<i>FFT</i>	0.2526	0.9039	
<i>Wavelet</i>	0.1255	0.2320	0.3905

(c)

Table 4.6: p-Values of the Mann-Whitney test on samples of running times for reconstructing one slice using EAS with the four different regularization operators defined in Eq. (3.9) for the EAS image sub-problem and different values of AF: $R = 2$ (a), $R = 8$ (b) and $R = 14$ (c). p-Values below the significance level 0.05 are boldfaced.

	<i>spTV</i>	<i>Laplacian</i>	<i>FFT</i>		<i>spTV</i>	<i>Laplacian</i>	<i>FFT</i>
<i>Laplacian</i>	0.0000			<i>Laplacian</i>	0.0000		
<i>FFT</i>	0.0000	0.0000		<i>FFT</i>	0.0000	0.0000	
<i>Wavelet</i>	0.0013	0.1835	0.0061	<i>Wavelet</i>	0.0010	0.0771	0.0018

(a)
(b)

	<i>spTV</i>	<i>Laplacian</i>	<i>FFT</i>
<i>Laplacian</i>	0.0000		
<i>FFT</i>	0.0000	0.0005	
<i>Wavelet</i>	0.0010	0.9329	0.0771

(c)

a horizontal line are also displayed. Similarly to the previous subsection, Figure 4.11 displays HFSEr (a), SSIM (b), NCC (c) and RMSE (d) averaged values across all slices and volunteers, parameterized by R , for the reconstructions just mentioned. The average time needed for reconstructing one slice is also provided in Figure 4.11e.

Tables 4.7–4.9 show p-values of comparisons with the Mann-Whitney test for every pair of regularization methods on samples of HFSEr (Table 4.7), RMSE (Table 4.8) and average time for reconstructing one slice (Table 4.9) for three values of AF, specifically $R = 2$, $R = 8$ and $R = 14$.

It is rather difficult to perceive differences with a naked eye between the three different versions of EAS that have been tested (EAS , EAS_{disp} and EAS_{vel}), unless one pays attention to small and subtle details. In fact, Figure 4.11 shows very similar values in HFSEr, SSIM and NCC, which is also supported by p-values (Table 4.7) in all the AF range. This is also the case for RMSE, where at a first glance might not be the case, but this may be just an effect on the scale (Figure 4.11d). Indeed, corresponding p-values (Table 4.8) do not reveal any significant difference ($p > 0.05$).

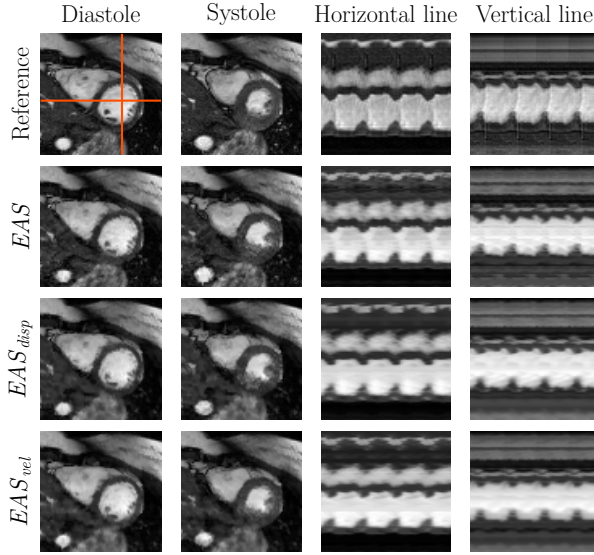


Figure 4.10: EAS reconstructions of a representative case with $R = 8$. The fully sampled reconstruction is included in the top line as a reference. Diastole and systole frames are shown in the two leftmost columns, respectively. Two temporal profiles of the horizontal and vertical lines —marked in the reference image with orange lines— are shown in the rightmost columns for all the methods.

Table 4.7: p-Values of the Mann-Whitney test on samples of HFSEER distributions for reconstructions using EAS with both fixed and variant regularization terms, and three different values of AF: $R = 2$ (a), $R = 8$ (b) and $R = 14$ (c).

	EAS	EAS_{disp}		EAS	EAS_{disp}
EAS_{disp}	0.2627		EAS_{disp}	0.3483	
EAS_{vel}	0.2708	0.8423	EAS_{vel}	0.2526	0.8758

(a) (b)

	EAS	EAS_{disp}
EAS_{disp}	0.2411	
EAS_{vel}	0.4730	0.0993

(c)

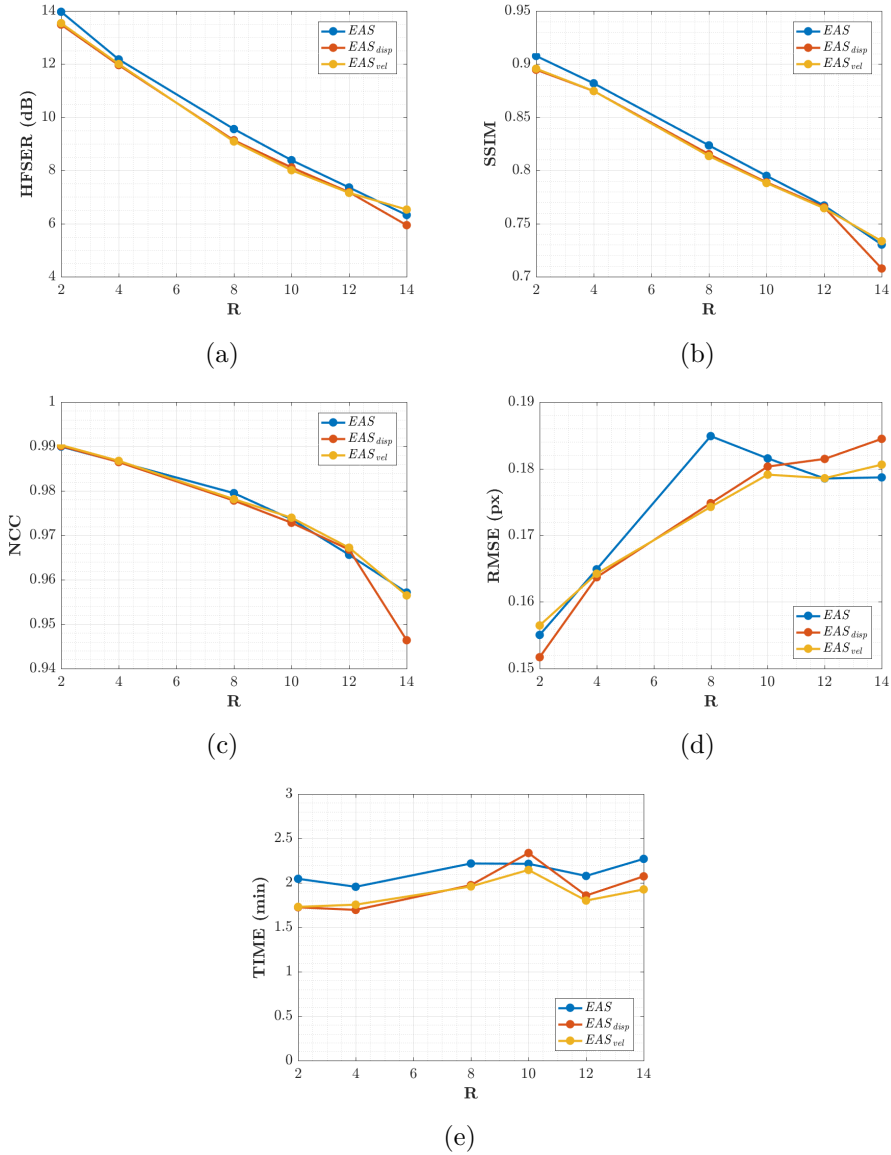


Figure 4.11: Results for EAS reconstructions with both fixed and variant regularization terms. The average values across slices and volunteers for HFSE (a), SSIM (b), NCC (c) RMSE (d) and the average time needed for reconstruct one slice (e) are provided for different values of R .

Table 4.8: p-Values of the Mann-Whitney test on samples of RMSE for reconstructions using EAS with both fixed and variant regularization terms, and three different values of AF: $R = 2$ (a), $R = 8$ (b) and $R = 14$ (c).

	<i>EAS</i>	<i>EAS_{disp}</i>		<i>EAS</i>	<i>EAS_{disp}</i>
<i>EAS_{disp}</i>	0.7708		<i>EAS_{disp}</i>	0.3096	
<i>EAS_{vel}</i>	0.9151	0.7065	<i>EAS_{vel}</i>	0.3375	0.9773
(a)			(b)		
	<i>EAS</i>	<i>EAS_{disp}</i>			
<i>EAS_{disp}</i>	0.6493				
<i>EAS_{vel}</i>	0.8814	0.7763			
(c)					

In contrast, p-values in Table 4.9 reveal that there are some significant differences between average running times for reconstructing one slice, specifically between EAS with fixed regularization terms (*EAS*) and both EAS with variant regularization terms (*EAS_{disp}* and *EAS_{vel}*). The former takes about 20 additional seconds with respect to the other two. This stems from the fact that variable regularization turns out to converge faster in the optimization algorithm, so that the execution time is reduced despite it entails more computational complexity. This overhead, for a typical multislice reconstruction, where the heart is divided into 10 or 12 slices, leads to a time saving between 3.5 and 4 minutes, approximately, per subject.

Figures 4.12 and 4.13 display the systole and diastole frames from two representative cases of the 2D datasets reconstructed with EAS methods (*EAS*, *EAS_{disp}* and *EAS_{vel}*) compared with other methods from the literature —*sPICS*, *GWCS*, *kt-SS* as well as the space-variant regularization methods proposed in Section 3.1 of this Thesis (*W_{disp}* and *W_{vel}*)—. Two temporal profiles from vertical and horizontal lines are also provided in the two rightmost columns. Both images and temporal profiles from

Table 4.9: p-Values of the Mann-Whitney test on samples of execution times for reconstructing one slice using EAS with both fixed and variant regularization terms, and three different values of AF: $R = 2$ (a), $R = 8$ (b) and $R = 14$ (c). p-Values below the significance level 0.05 are boldfaced.

<table style="width: 100%; border-collapse: collapse;"> <thead> <tr> <th style="width: 50%;"></th> <th style="width: 50%; text-align: center;"><i>EAS</i></th> <th style="width: 50%; text-align: center;"><i>EAS_{disp}</i></th> </tr> </thead> <tbody> <tr> <td style="text-align: center;"><i>EAS_{disp}</i></td> <td style="text-align: center;">0.0027</td> <td></td> </tr> <tr> <td style="text-align: center;"><i>EAS_{vel}</i></td> <td style="text-align: center;">0.0022</td> <td style="text-align: center;">0.9943</td> </tr> </tbody> </table>		<i>EAS</i>	<i>EAS_{disp}</i>	<i>EAS_{disp}</i>	0.0027		<i>EAS_{vel}</i>	0.0022	0.9943	<table style="width: 100%; border-collapse: collapse;"> <thead> <tr> <th style="width: 50%;"></th> <th style="width: 50%; text-align: center;"><i>EAS</i></th> <th style="width: 50%; text-align: center;"><i>EAS_{disp}</i></th> </tr> </thead> <tbody> <tr> <td style="text-align: center;"><i>EAS_{disp}</i></td> <td style="text-align: center;">0.0124</td> <td></td> </tr> <tr> <td style="text-align: center;"><i>EAS_{vel}</i></td> <td style="text-align: center;">0.0414</td> <td style="text-align: center;">0.6040</td> </tr> </tbody> </table>		<i>EAS</i>	<i>EAS_{disp}</i>	<i>EAS_{disp}</i>	0.0124		<i>EAS_{vel}</i>	0.0414	0.6040
	<i>EAS</i>	<i>EAS_{disp}</i>																	
<i>EAS_{disp}</i>	0.0027																		
<i>EAS_{vel}</i>	0.0022	0.9943																	
	<i>EAS</i>	<i>EAS_{disp}</i>																	
<i>EAS_{disp}</i>	0.0124																		
<i>EAS_{vel}</i>	0.0414	0.6040																	
(a)	(b)																		
<table style="width: 100%; border-collapse: collapse;"> <thead> <tr> <th style="width: 50%;"></th> <th style="width: 50%; text-align: center;"><i>EAS</i></th> <th style="width: 50%; text-align: center;"><i>EAS_{disp}</i></th> </tr> </thead> <tbody> <tr> <td style="text-align: center;"><i>EAS_{disp}</i></td> <td style="text-align: center;">0.2439</td> <td></td> </tr> <tr> <td style="text-align: center;"><i>EAS_{vel}</i></td> <td style="text-align: center;">0.0187</td> <td style="text-align: center;">0.1935</td> </tr> </tbody> </table>				<i>EAS</i>	<i>EAS_{disp}</i>	<i>EAS_{disp}</i>	0.2439		<i>EAS_{vel}</i>	0.0187	0.1935								
	<i>EAS</i>	<i>EAS_{disp}</i>																	
<i>EAS_{disp}</i>	0.2439																		
<i>EAS_{vel}</i>	0.0187	0.1935																	
(c)																			

the fully sampled reconstruction are included as a reference in the top line. In terms of image quality, EAS reconstructions tend to have less subsampling artifacts (Figure 4.12, orange arrows), but they may show some more pronounced blurring—especially in EAS_{vel} —due to the spatial regularization that is applied in the EAS image-subproblem (4.12, red arrows). In terms of motion, EAS reconstructions (EAS , EAS_{disp} and EAS_{vel}) seem smoother, whereas in the other methods motion is perceived with sharper transitions, mostly when AF increases. Nevertheless, in some of the EAS reconstructions residual fluctuations may also be perceived in the images, as if they were immersed in liquid. This effect probably arises as a consequence of using a B-spline deformation model and sub-optimal regularization parameter tuning.

In addition, EAS methods tend to show difficulties in homogeneous areas where registration is known to show worse performance. Since EAS methods are essentially model-based (as opposed to the other methods, which are data-driven), resulting reconstructions tend to be in some areas more static than expected, what may lead to a false diagnosis of a movement disorder characterized by that loss of motion (hypokinesia). An example of this effect

is presented in Figure 4.13. The corresponding EAS reconstructions showed more static inferior/inferior-lateral segments compared to the reference image. This fact manifest itself in the images of the temporal profile of the vertical line (rightmost column of Figure 4.13) by a subdued fluctuation in the intensity line as a consequence of contraction of the myocardium (marked with blue arrows).

For the sake of performance quantification, figure 4.14 shows HFSER (a), SSIM (c) and NCC (e) averaged values across all slices and volunteers, parameterized by R , for the reconstructions of the 2D datasets by applying EAS with both fixed and variant regularization terms in comparison with the reconstruction methods mentioned in previous paragraphs. Since the resulting graphs are very close together, their relative values with respect to those provided by $GWCS$ are shown (Figures 4.14b, d and f, respectively), so that both visualization and interpretation could be easier. Similarly, Figure 4.15 displays RMSE (a), Landmark RMSE (c) —as defined in Chapter 3— and average time needed for reconstructing one slice (e) and their relative values (Figures 4.15b, d and f, respectively), taking again $GWCS$ method as reference.

Figure 4.14 shows that the set of EAS methods gives rise to values of the metrics more closely related to intensity quality (HFSER, SSIM and NCC) lower than those provided by the other methods for AF less than 8. From this AF value, the metrics begin to approximate and from $R = 10$ EAS methods give rise to slightly higher values than the other ones, specifically EAS and EAS_{vel} . As far as motion metrics is concerned, the crossing point seems to be also at $R=10$. Below this value, the rest of methods give rise to higher values, but there is no method that clearly qualifies as “*the winner*”. In contrast, for $R \geq 10$ EAS methods give rise to higher values, being EAS_{vel} the method with the highest scores closely followed by EAS . Taking into account the RMSE scores, EAS methods with variant regularization terms give rise to lower values than the rest of reconstruction methods (here lower is better). The Landmarks RMSE

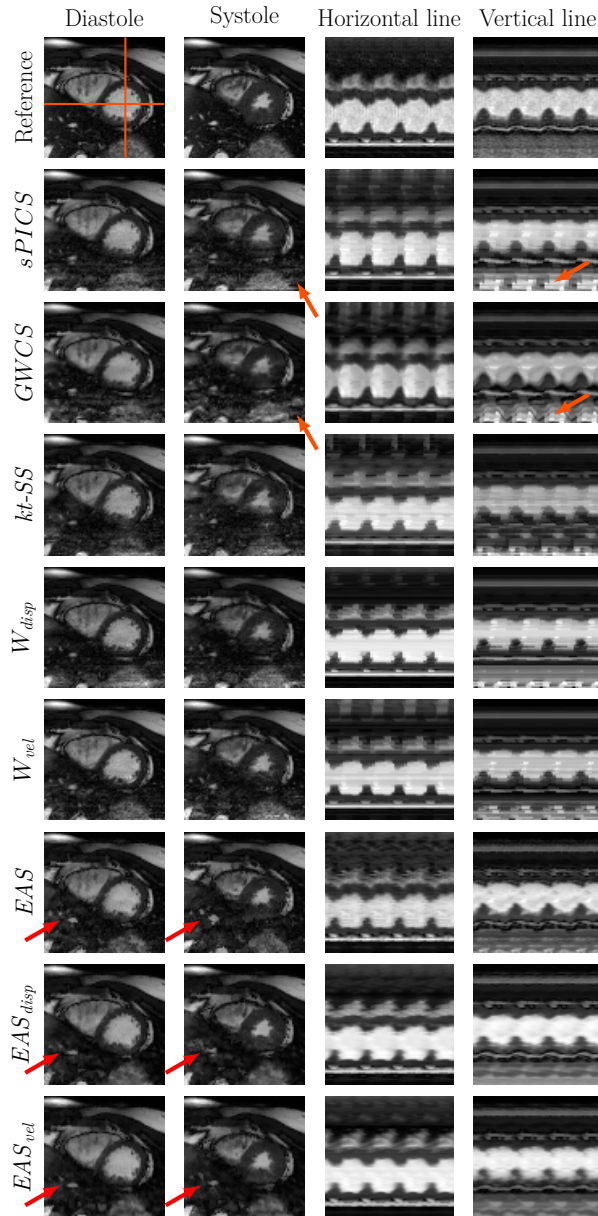


Figure 4.12: Comparison of EAS reconstructions with other methods from the literature for a representative case (volunteer 2) with $R = 8$. The fully sampled reconstruction is included in the top line as a reference. Diastole and systole frames are shown in the two leftmost columns, respectively. Two temporal profiles of the horizontal and vertical lines —marked in the reference image with orange lines— are shown in the rightmost columns for all the methods. Arrows point to significant locations.

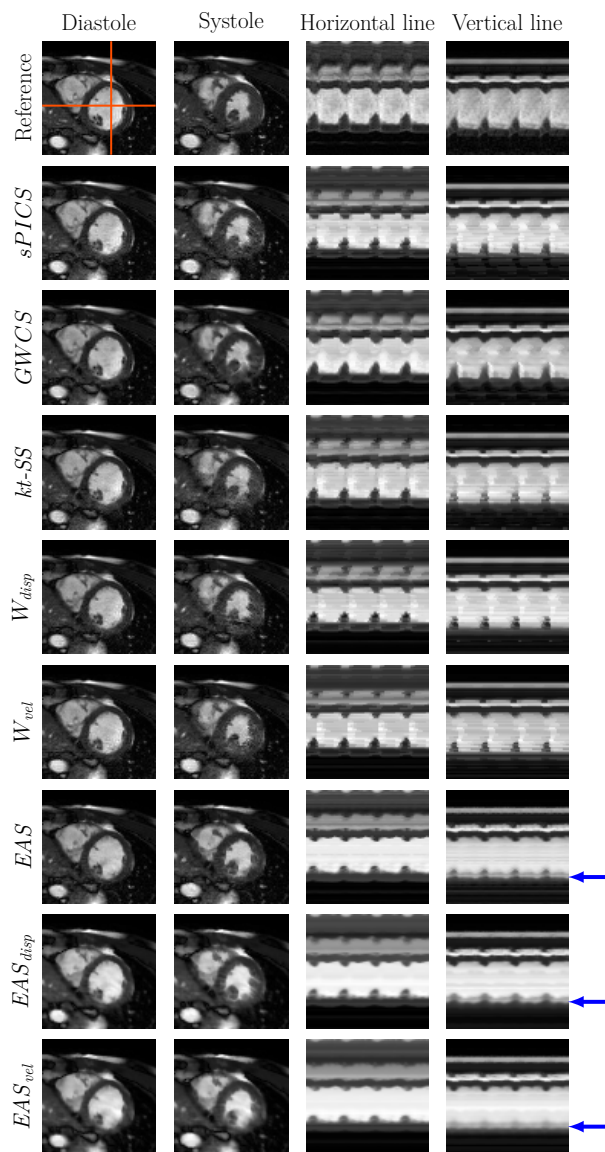


Figure 4.13: Comparison of EAS reconstructions with other methods from the literature for a representative case (volunteer 3) with $R = 8$. The fully sampled reconstruction is included in the top line as a reference. Diastole and systole frames are shown in the two leftmost columns, respectively. Two temporal profiles of the horizontal and vertical lines —marked in the reference image with orange lines— are shown in the rightmost columns for all the methods. Arrows point to significant locations.

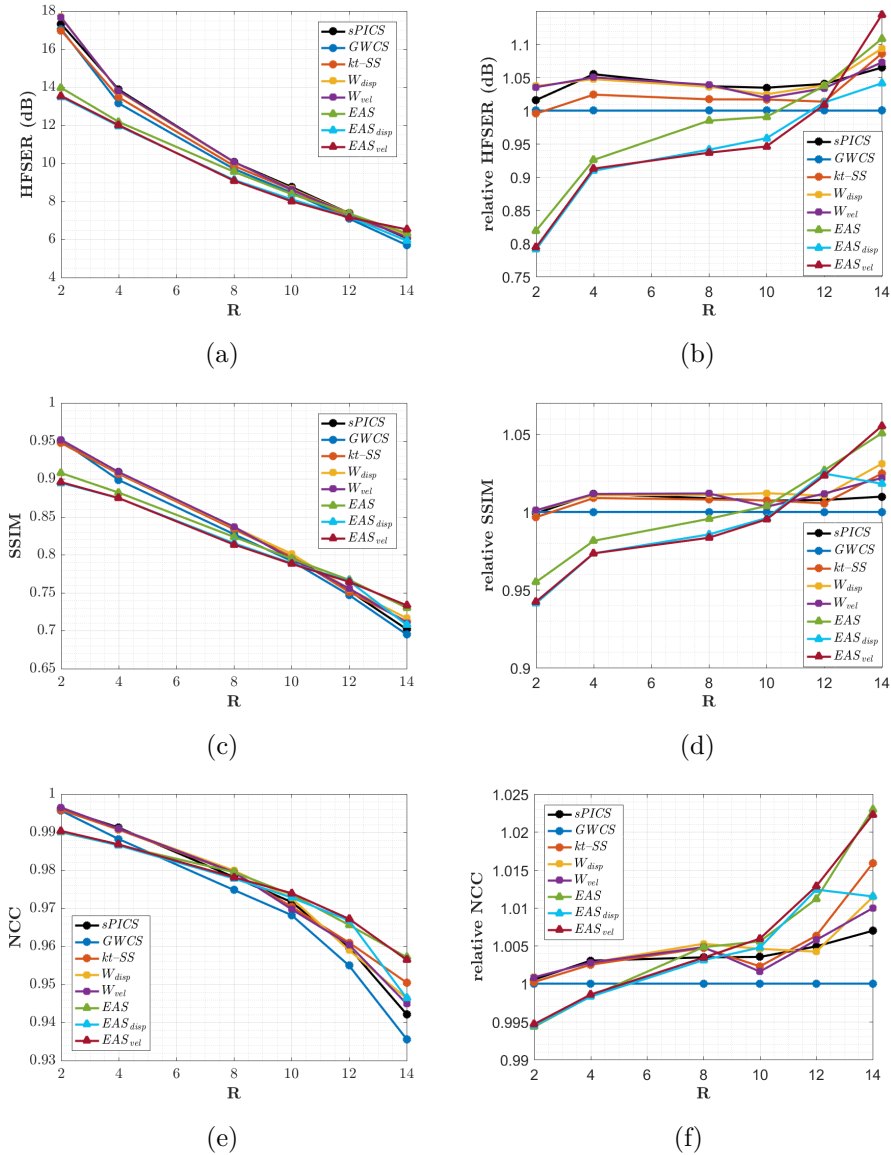


Figure 4.14: EAS with both fixed and variant regularization terms compared to other methods from the literature. Absolute values for HFSE (a), SSIM (c) and NCC (e), parametrized by R are shown. Relative values for HFSE (b), SSIM (d) and NCC (f), taking $GWCS$ method as reference and parametrized by R , are also displayed.

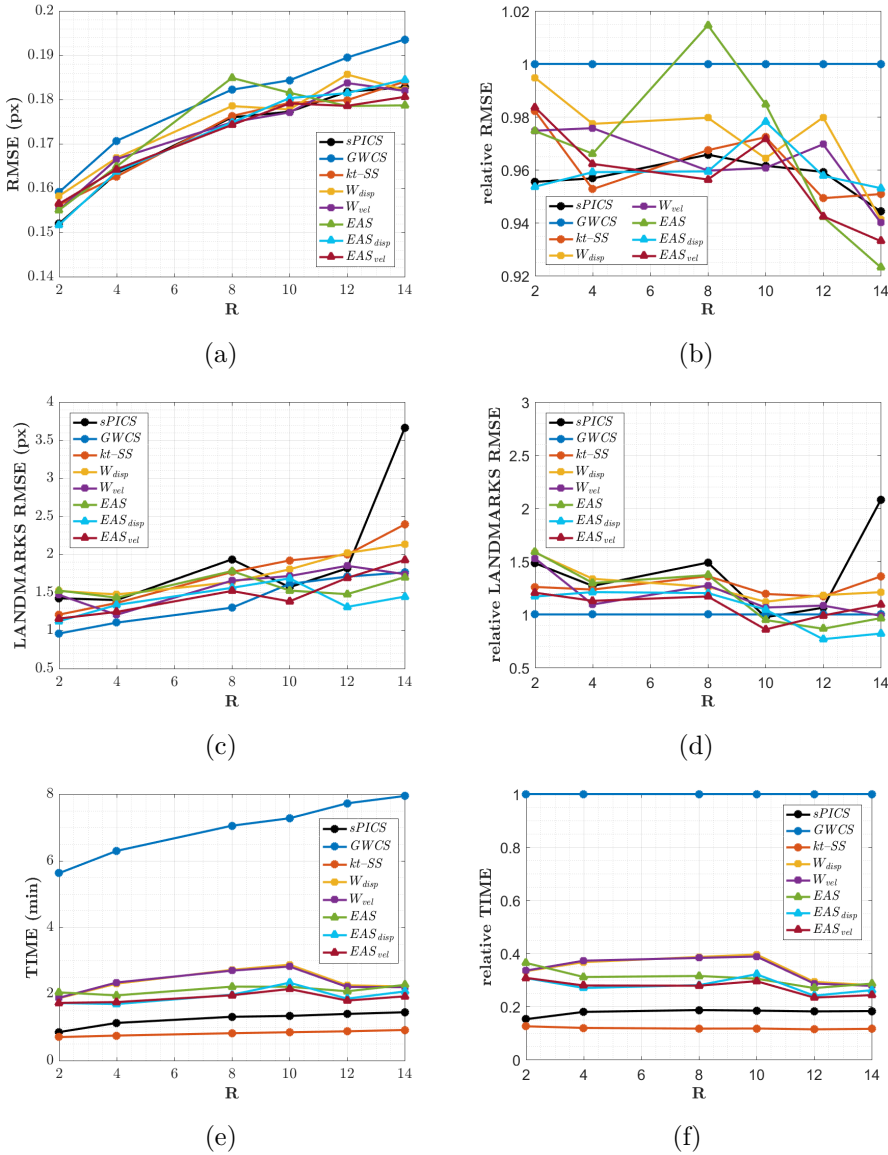


Figure 4.15: EAS with both fixed and variant regularization terms compared to other methods from the literature. Absolute values for RMSE (a), landmarks RMSE (c) and average time for reconstructing one slice (e), parametrized by R are shown. Relative values for RMSE (b), landmarks RMSE (d) and average time for reconstructing one slice (f), taking *GWCS* method as reference and parametrized by R , are also displayed.

shows a similar behaviour to the other metrics: below $R = 10$, *GWCS* gives rise to the lowest values, whereas EAS methods lead for higher R values.

Additionally, a cardiologist² was consulted by means of a questionnaire, consisting of 21 videos. Each video displayed a composition of CINE reconstructions of the same slice, volunteer and AF level by applying the six methods to be compared, randomly sorted: *sPICS*, *GWCS*, *kt-SS*, *EAS*, *EAS_{disp}* and *EAS_{vel}* (*W_{disp}* and *W_{vel}* were not included to simplify the task). The fully sampled image was also included as reference (see Figure 4.16) and the selected levels of AF were $R = 8$, $R = 10$ and $R = 14$. The expert was asked to sort the reconstructions in each video according to his perceived quality, especially in terms of observed motion, giving a score of 6 to the reconstruction with the best quality and a score of 1 to the reconstruction with the worst quality.

According to the expert all the images were useful for diagnosis. He reported the great difficulty of executing the task, since all the images were quite similar and the differences between them were very subtle. Nevertheless, he also mentioned that it was relatively easier to find differences between the images in the quality extremes, than among those in the intermediate quality levels. He also reported that a homogeneous decision criterion for the entire sample was very difficult to set, since different subtle details had to be accounted for, such as sharpness in trabeculae or papillary muscles, among other structures, depending on the image in every moment. Table 4.10 displays the mean value \pm standard deviation calculated out of the scores that each reconstruction method received in the 21 videos mentioned above.

It can be inferred from the results in Table 4.10, the *GWCS* reconstruction method received, generally speaking, the highest scores. EAS methods, however, give rise to motion patterns that the expert was not comfortable with, despite Figures 4.14 and 4.15 indicate that EAS methods provide

²Dr. David Filgueiras-Rama, from CNIC, Spain.

Table 4.10: Mean value \pm standard deviation of the scores given by the expert for each reconstruction method. The scores vary in the range $[1, 6]$, being 6 the method that provides reconstructions with the highest image quality.

	R=8	R=10	R=14
<i>sPICS</i>	5.14 ± 0.69	4.86 ± 0.69	3.43 ± 1.72
<i>GWCS</i>	5.00 ± 1.83	5.71 ± 0.49	4.86 ± 1.68
<i>kt-SS</i>	4.00 ± 1.53	3.43 ± 1.62	4.86 ± 0.90
<i>EAS</i>	2.57 ± 1.13	2.57 ± 0.79	3.29 ± 1.38
<i>EAS_{disp}</i>	2.43 ± 0.53	2.71 ± 1.60	2.14 ± 1.46
<i>EAS_{vel}</i>	2.00 ± 1.15	1.71 ± 0.76	2.43 ± 1.40

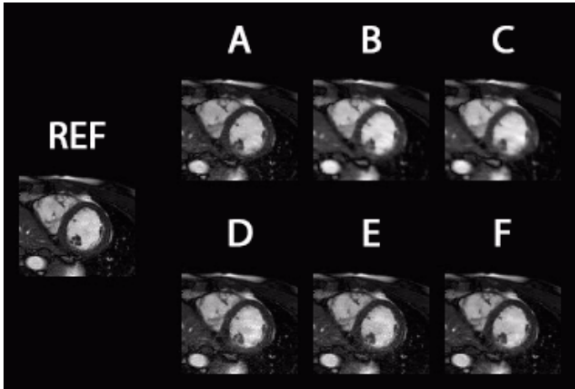
better figures for $R \geq 10$. As stated above, the model-based character of EAS seems to reduce the degrees of freedom in the reconstruction to an extent that other data-driven methods are preferable to the expert eye in terms of motion quality (but not in terms of image quality).

Hence, due to the fact that motion provided by *GWCS* was the preferred expert option, but EAS provides slightly better results with considerable less execution times when $R \geq 10$, according to Figures 4.14 and 4.15, the combination of both methods —EAS as an initializer of *GWCS*— can benefit from each other, since better motion reconstructions can be achieved with *GWCS* but in EAS comparable running times. This is developed in the next subsection.

4.2.3 Combination of elastic alignedSENSE and groupwise motion-compensated compressed sensing

Figure 4.17 illustrates reconstructions for the different versions of MIX methods with both fixed and variant regularization terms in comparison with *GWCS* and *EAS* for a representative case and $R = 8$. Specifically, diastole and systole frames are displayed in the two leftmost columns. The fully sampled images of reference are shown in the top line for comparison purposes. Two temporal profiles of both horizontal and vertical lines — marked in the reference image with orange lines— are also displayed, in

DISPLAY 2: Sort the reconstruction methods (A-F) shown in the following video according to the image quality, being 1 the method with the worst quality and 6, the method with the best. Please do not select more than one answer per column unless the qualities are completely indistinguishable.



	1 (worst)	2	3	4	5	6 (best)
Method A	<input type="radio"/>	<input type="radio"/>	<input type="radio"/>	<input type="radio"/>	<input type="radio"/>	<input type="radio"/>
Method B	<input type="radio"/>	<input type="radio"/>	<input type="radio"/>	<input type="radio"/>	<input type="radio"/>	<input type="radio"/>
Method C	<input type="radio"/>	<input type="radio"/>	<input type="radio"/>	<input type="radio"/>	<input type="radio"/>	<input type="radio"/>
Method D	<input type="radio"/>	<input type="radio"/>	<input type="radio"/>	<input type="radio"/>	<input type="radio"/>	<input type="radio"/>
Method E	<input type="radio"/>	<input type="radio"/>	<input type="radio"/>	<input type="radio"/>	<input type="radio"/>	<input type="radio"/>
Method F	<input type="radio"/>	<input type="radio"/>	<input type="radio"/>	<input type="radio"/>	<input type="radio"/>	<input type="radio"/>

DISPLAY 2: comments (optional)

Your answer

[Back](#) [Next](#)

Figure 4.16: Example of the questionnaire for subjective image quality assessment. The questionnaire was originally written in Spanish, but has been translated here into English to facilitate its reading by non-Spanish speakers.

the two rightmost columns. The superscript in the MIX methods represent the number of EAS stages before the *GWCS* stage.

Figure 4.18 shows HFSER (a), SSIM (c) and NCC (e) for the 2D datasets reconstructed by using both MIX^n , MIX_{disp}^n and MIX_{vel}^n ($n = 1, 2$), parameterized by R , in comparison with with *GWCS* and *EAS*. Their relative values are also shown (Figures 4.18b, d and f), taking *GWCS* as reference. Figure 4.19 shows the corresponding RMSE (a) and average execution time for reconstructing a slice (b).

There are hardly any noticeable differences within the reconstructions using MIX methods (Figure 4.17). Indeed, it can be seen in Figure 4.18 that MIX methods provide figures very similar to each other for the metrics related with intensity (HFSER, SSIM and also NCC). Furthermore, the MIX values in Figure 4.18 are comparable with those provided by *GWCS* for lower values of AF, but they separate when AF is increasing, with MIX providing values higher than those from the other methods, including *EAS*. Looking to Figure 4.19 we can notice that MIX methods give rise to lower values of RMSE, specifically, the MIX strategies that incorporate variant regularization terms using velocity fields.

As far as execution time is concerned, MIX strategies take much less time than *GWCS*, about two or three times less, reaching the same level as *EAS*, particularly when MIX strategies with one EAS stage are considered (MIX^1 , MIX_{disp}^1 and MIX_{vel}^1). Between the two groups of MIX strategies—those with one EAS stage and those with two EAS stages, previous to the *GWCS* stage—the differences in running times can be as long as one minute, approximately. However, as seen above, the quality of reconstruction is similar in both. Therefore, MIX^1 strategies—and specifically, MIX_{vel}^1 —arise as competitive reconstruction methods to take into account.

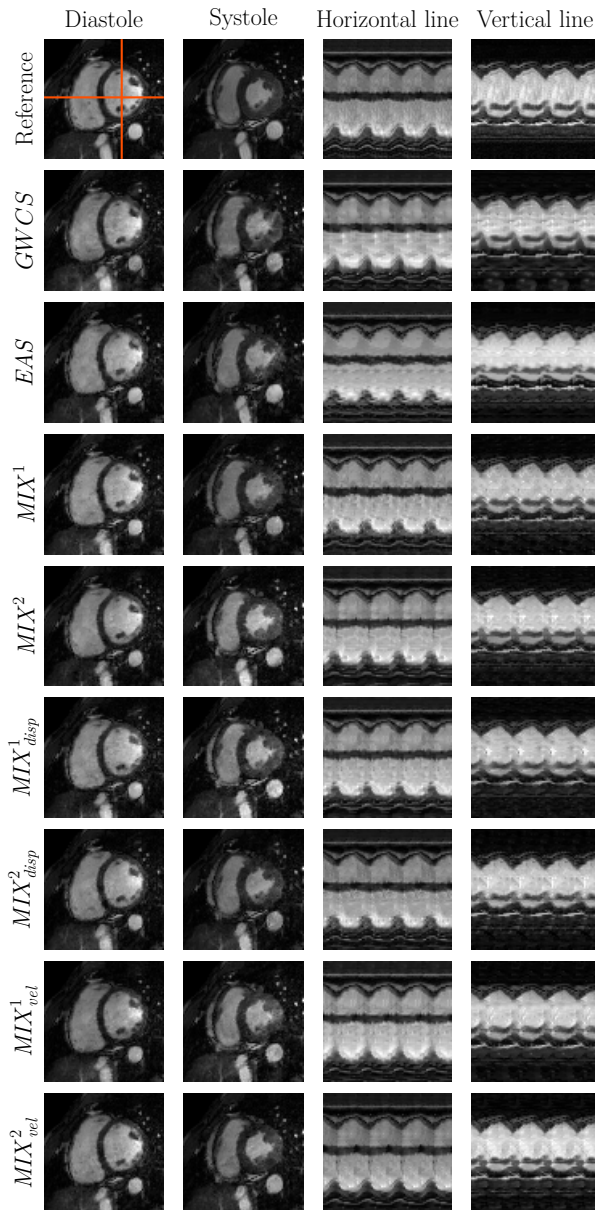


Figure 4.17: Comparison of MIX reconstructions with *GWCS* and *EAS* for a representative case with $R = 8$. The fully sampled reconstruction is included in the top line as a reference. Diastole and systole frames are shown in the two leftmost columns, respectively. Two temporal profiles of the horizontal and vertical lines—marked in the reference image with orange lines—are shown in the rightmost columns for all the methods.

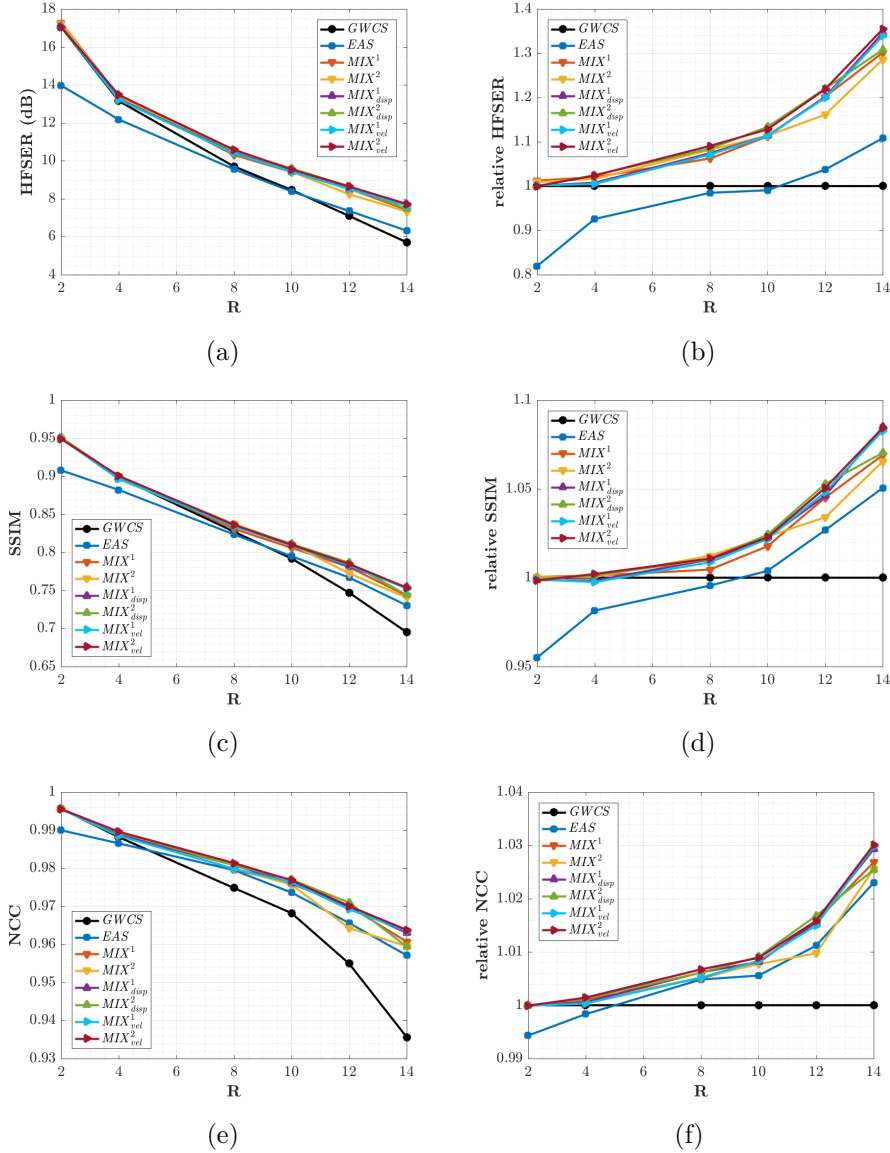


Figure 4.18: MIX with both fixed and variant regularization terms compared with EAS and GWCS. Absolute values for HFSEER (a), SSIM (c) and NCC (e), parameterized by R are shown. Relative values for HFSEER (b), SSIM (d) and NCC (f), taking GWCS as reference and parameterized by R are also displayed.

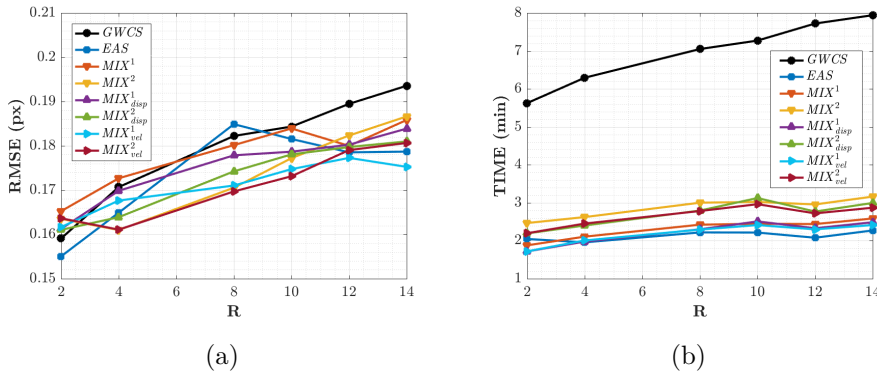


Figure 4.19: MIX with both fixed and variant regularization terms compared to EAS and GWCS. RMSE (a) and average execution times for reconstructing one slice (b), parameterized by R are shown.

4.2.4 Radial extension of elastic alignedSENSE

Figure 4.20 illustrates 2D golden radial reconstructions using EAS with both fixed and variant regularization terms in comparison with *iGRASP* and *GWCS* for a representative case. The reconstructions using the three variants of the MIX method are also included. In the two leftmost columns diastole and systole frames are shown and in the two rightmost columns temporal profiles of both horizontal and vertical lines (marked with orange lines in the top left image) are represented. Table 4.11 shows the average running time needed for reconstruct one slice. The equivalent AF for this example is 19.33.

The *iGRASP* method provides the most blurred images: the borders of the myocardium are not as defined as in the other methods. In addition, the contraction motion of the heart is reduced, which can be perceived by the smooth intensity waves in the temporal profiles (see purple arrows in Figure 4.20). On the contrary, *GWCS* seems to reflect the motion of the heart in a more accurate way, compared to the Cartesian reconstructions from the previous experiments.

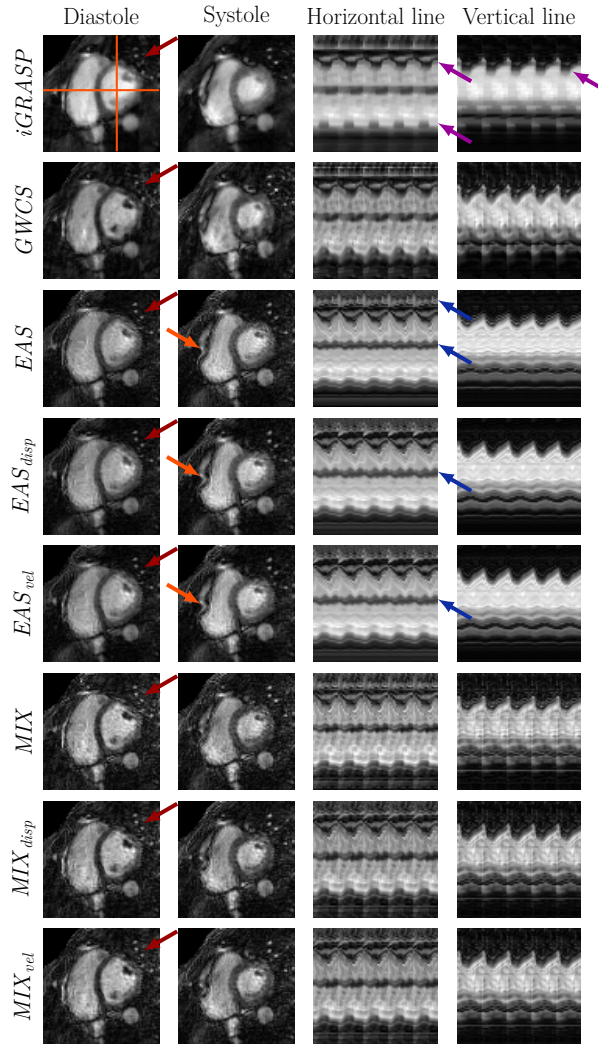


Figure 4.20: EAS radial reconstructions in comparison with iGRASP and GWCS ($R = 19.33$). Reconstructions from MIX methods have been also included. Arrows point significant locations.

Table 4.11: Mean values of execution times for reconstructing one slice using EAS and MIX radial approaches in comparison with iGRASP and GWCS.

	mean running time (min)
<i>iGRASP</i>	1.9513
<i>GWCS</i>	6.4263
<i>EAS</i>	2.2940
<i>EAS_{disp}</i>	1.8276
<i>EAS_{vel}</i>	1.6979
<i>MIX</i>	3.7792
<i>MIX_{disp}</i>	2.6890
<i>MIX_{vel}</i>	2.9559

There are no perceptible differences between the three versions of EAS (*EAS*, *EAS_{disp}* and *EAS_{vel}*) but not among the three versions of MIX methods (*MIX*, *MIX_{disp}* and *MIX_{vel}*). The three EAS strategies also preserve motion, although there is a slightly loss of it. This effect can be observed in the intensity fluctuations due to myocardial contraction in the temporal profiles, which are perceived not as prominent as in *GWCS*. In addition, the torsion motion has not been captured by the deformations of EAS approaches, although this torsion is maintained in the Cartesian reconstruction. This is probably due to the fact that the regularization term in the radial EAS deformation sub-problem is filtering out some important components of motion, so that a finer tuning of the parameters might be necessary. Despite this, EAS strategies still introduce some residual vibrations in the image sequences, as a consequence of the B-spline model used for deformations. This can be seen in the temporal profiles of Figure 4.20 as tiny waves in some intensity bands (blue arrows). Finally, EAS strategies have introduced a non-realistic deformation in the right ventricle (Figure 4.20, orange arrows). MIX methods on the contrary manage to capture the torsion motion and the general motion is perceived of the same quality as in *GWCS* but with slightly sharper details and less subsampling artifacts.

As far as running time is concerned, the fastest method is EAS_{vel} , followed by EAS_{disp} and $iGRASP$, which take between 10-15 more seconds. MIX approaches reach an intermediate level and take half of the time needed by GWCS, which is the slowest approach, taking almost 6.5 minutes per slice. Other point to highlight is that the versions that make use of variable regularization are faster than their versions with fixed regularization. Specifically, EAS_{disp} and EAS_{vel} are about 30 seconds faster than EAS , whereas MIX_{disp} and EAS_{vel} take about a minute less than MIX .

Chapter 5

CONCLUSIONS AND FUTURE WORK

5.1 Conclusion

MRI is a powerful image modality due to its reproducibility, accuracy and versatility and it offers high spatial resolution, wide FOV and good contrast between soft tissues. However, an MRI scan takes long time compared to common physiological processes and the acquisition procedure requires well-trained staff and elaborated setups.

One way to reduce scan times is to subsample k-space data and to apply involved image reconstruction techniques. However, this makes the resulting reconstruction problem become undetermined, due to absent samples, and ill-conditioned, due to presence of noise in measurements. Thus, some knowledge, constrains and assumptions are integrated in the function to be optimized for reconstruction, usually making the overall problem even more computationally demanding and time consuming. Modern learning-based approaches are fast in production mode, but require long training stages.

This Thesis has focused on the cardiac CINE MRI reconstruction problem from highly subsampled data. The work in this Thesis has pursued to use motion as a source of knowledge, i.e., to take advantage of the redundancy in the images in both spatial and temporal dimensions to reduce, whenever possible, computational needs and execution times in the optimization while keeping quality in the reconstructions. This statement

was our main objective, from which two sub-objectives were identified, namely, to define a strategy for spatially varying regularization and to reduce the number of parameters needed in the problem by finding a pattern image (reference) and a set of deformations to apply to that image. The contributions derived from this Thesis (described in section 5.2) allow us to state that these objectives have been satisfied.

This Thesis, however, has a number of limitations which give rise to some ideas to be explored in future work. Those future lines of research are covered in Section 5.3.

5.2 Contributions

The main contributions and results of this Thesis are:

- Space-time variant weighted regularization strategies based on group-wise motion estimation. We have observed that CS in combination with this kind of regularization provides better reconstructions in terms of motion fidelity than other methods from the literature.
- Design and implementation of the EAS framework for cardiac CINE MRI reconstruction for both Cartesian and radial subsampling. This reconstruction framework provides a motion-free pattern image along with a set of nonrigid deformations. Motion is not only used here to deform the pattern image that generates the cardiac CINE series, but also to weight the regularization degree in the objective functions. However, no appreciable differences have been observed in terms of image intensity quality between variant and non-variant regularization versions of the proposed method, but they arise when motion quality and running times are considered, where variant regularized strategies seem preferable. We have also observed that the regularization term based on spTV (spatial Total Variation) employed in the image sub-problem provides reconstructions with a similar quality,

but with less execution times, than the other regularization terms that have been tested (FT, Laplacian and Wavelet Transform).

- The combination of EAS and GWCS as a complete reconstruction method provides images with a better degree of quality in both intensity and motion, or with comparable quality and less computational load, compared to other methods from the literature. Specifically, the combination of EAS with variant regularization weighted by velocity fields and GWCS (denoted as MIX_{vel}) arises, in our opinion, as the most competitive method to take into account and to keep exploring in future lines of investigation, since it has provided the highest quality metrics and the lowest error between displacement fields as well, and also incorporates the motion patterns preferred by the expert eye, but with less computational load and shorter running times than other approaches.

As a result of the work described in the Thesis mentioned, the following secondary contributions have also arisen:

- Generalization of 3D Cartesian sampling scheme with spiral golden angle ordering. This sampling scheme is designed to make it possible to choose, by a certain continuous parameter α , from a uniform sampling pattern of k-space to a denser sampling scheme in its center. For CINE cardiac MRI α values in the vicinity of $\alpha = 1$ seem preferable. However, higher noise content makes intermediate configurations ($\alpha \approx 0.7$) draw better results.
- A cross validation method to select regularization parameters based on certain image quality metrics, when the number of available images is scarce has been also proposed.

5.3 Future work

EAS is capable to reconstruct cardiac CINE images, but in some cases some motion components are lost. This is due to the fact that the method is model-based. In such methodologies the performance is satisfactory as long as the model describes accurately the motion that is dealt with. Our results seem to indicate that this is not quite the case, as revealed by a cardiologist subjective assessment. Indeed, there is a limitation in the method by its own 2D nature: cardiac motion has a component in the perpendicular direction to the observation plane (*through-plane motion*), which cannot be estimated or recovered based on its two-dimensional projection in the observation plane. Thus, the estimated motion will not fully represent the real deformations that the heart suffers, since only the two *in-plane* components are accessible. This fact restricts the ability of the estimation method —EAS deformation sub-problem— and, consequently, the quality of the reconstructed images is reduced. Hence, the extension to 3D arises as a natural line of future work, where the problem of through-plane motion disappears. In addition, 3D reconstruction offers an advantage over 2D multi-slice reconstruction: the latter needs a laborious spatial planning, due to the leaning position of the heart within the thoracic cage and the variability between subjects. In a 3D method with isotropic resolution, this operation can be avoided since orientation can be obtained retrospectively from the canonical planes. External contrast, however, is needed for the latter.

On the other hand, the deformation model used in EAS may be not entirely adequate or it may be too simple to describe the complex motion of the heart. Therefore, a more exhaustive modelling of the components of the heart motion seems mandatory, as well as to account for respiratory motion, specially in the 3D case.

The level of running times achieved by EAS and MIX approaches may be still not clinically viable. Furthermore, the implementation of the

algorithms used for this Thesis were executed in CPU and implemented in Matlab and still in a development stage, so that some programming optimization or even a compiled implementation surely would be possible to reduce running times. Nevertheless, the MRI reconstruction problem turns out to be highly parallelizable, so that an implementation in GPU seems advisable.

However, programming in GPU is device dependent. OpenCL [99] is an open standard for parallel computing that covers a wide set of computing devices from several vendors, while ensuring that source code and data are unique, thus avoiding the need for code and data replication among prospectively supported devices. However, OpenCL programmers must deal on their own with device selection and initialization, memory management, kernel loading and compilation, host-device interaction, and administration overload. The OpenCLIPER framework [100] was developed to address all these shortcomings, allowing to work in a wide range of computing devices (CPU, GPU, DSP, FPGA, etc.), so that development is significantly simplified versus a pure OpenCL implementation. Therefore, EAS and MIX as well could benefit from OpenCLIPER and achieve more competitive running times. In fact —and serve as an example—, the authors in [101] report running times between 4 and 8 seconds for reconstructing a whole slice stack of k-space data similar to those datasets used in this Thesis by using a GPU implementation similar to the GWCS algorithm.

DL approaches have gained importance recently, since they are capable of obtaining reconstructions typically in the order of seconds, once the training step is completed. Most of DL MRI reconstruction techniques are based on a supervised training strategy, but they require abundant high-quality reference images for network training, which are not always available [83]. Several recent works have investigated self-supervised learning for the reconstruction of undersampled MRI [102,103], in which a network is trained on undersampled datasets directly without fully sampled references, and inherent MR physical models are incorporated as training regularizations,

achieving a similar reconstruction performance. EAS and MIX can benefit from such self-supervised approaches, by adopting a methodology similar to [101], where the optimization problem is considered as an inverse problem including a data fidelity term and a regularization term with groupwise motion compensation, implemented by means of a pre-trained network [104]. Thus, running times may be further reduced and become clinically viable.

Furthermore, EAS has been mainly evaluated from a technical point of view, although the clinical viewpoint has also been tackled by consulting a cardiologist, who kindly assessed the proposed methods through a questionnaire. However, this second method has the drawback of subjectiveness, especially if only one expert judgement is available. Therefore, it would be advisable to assess the proposed methods from the clinical point of view by using more objective indicators, such as the well-established end systolic volume or end diastolic volume, among others.

Finally, only datasets from healthy volunteers have been used. Therefore, it would be advisable to test the EAS method with patients with certain pathologies, such as arrhythmia, hypokinesia or any other condition related to impaired left ventricle and/or regional wall motion abnormalities.

Appendix A

GENERALIZED 3D CARTESSIAN SAMPLING SCHEME WITH SPIRAL GOLDEN ANGLE ORDERING

A.1 Introduction

Non-Cartesian sampling patterns, such as radial or spiral, are more robust to motion. However, they have the disadvantage that FFT algorithm cannot be directly applied to reconstruct an image and therefore a prior gridding stage is needed, which introduces more complexity and overload to the reconstruction problem.

As stated in Section 2.2.1, different approaches that use Cartesian trajectories with spiral profiles and golden angle step have been proposed to avoid the gridding procedure and accelerate the reconstruction problem. G-CASPR [36] is characterized by a scheme with uniform k-space sampling pattern that is usually applied to static MRI, although in [80] was used in cardiac CINE MRI. Nevertheless, compressed sensing have shown better results if the center of k-space is more densely sampled [35, 105]. VDRad [34] is a variable density sampling scheme that has been reported for abdominal imaging. This sampling scheme has the drawback that some positions in the k-space are repeatedly acquired, decreasing efficiency. We define a

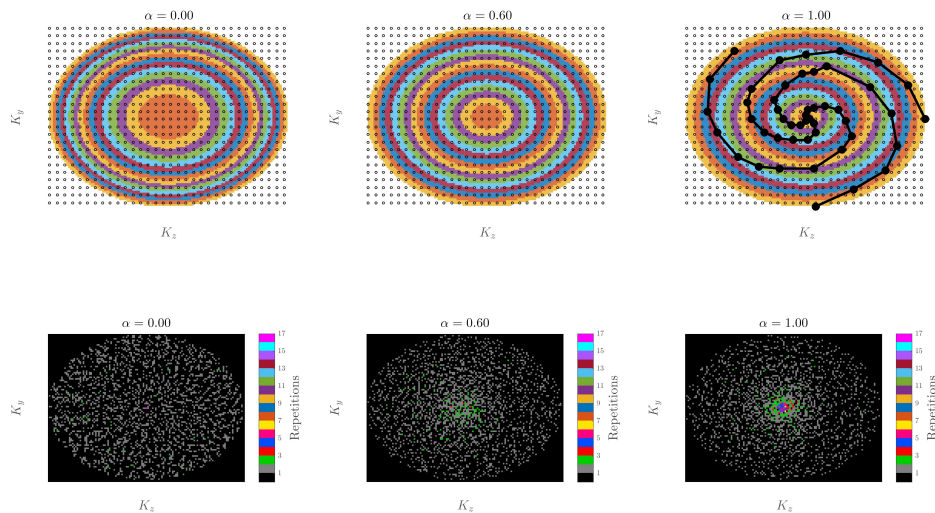


Figure A.1: proposed sampling pattern overview. Top line: on the left, each ring has the same area ($\alpha = 0.00$), on the right each ring has the same radial width ($\alpha = 1.00$). In the center an intermediate case is shown ($\alpha = 0.60$) where each ring has variable radial width and area. Bottom line: Resulting sampling patterns for different values of α after the cardiac binning. Sampling patterns show uniformity for $\alpha = 0.00$, although there are some zones with a few samples in the center of k-space. The density in the center of k-space increases progressively with the value of α and so do the repetitions of samples. The number of times that a sample has been visited is represented by colors.

versatile sampling scheme that varies continuously, by setting a parameter α , from a uniform sampling pattern of k-space to a denser sampling scheme in its center. The reason of this is to determine whether intermediate configurations can provide better sampling schemes for cardiac CINE MRI applications.

A.2 Description of the sampling scheme

The proposed sampling scheme is defined here as a general Cartesian sampling scheme with spiral ordering of samples and golden-angle step.

Specifically, samples are acquired from the center to the periphery of the k_y - k_z plane, giving rise to spiral-like trajectories (see Figure A.1); k_x dimension is fully sampled. Given a spiral length L , the k_y - k_z plane is divided into L concentric elliptic rings (no corners are used) and each ring in turn is divided in L sectors. The radii of every ring along the k_y and k_z directions (R_{K_y} and R_{K_z} , respectively) are controlled by the parameter α , as shown by

$$\left. \begin{aligned} R_{k_y}(k) &= \alpha \cdot \frac{kN}{2L} + (1 - \alpha) \cdot \frac{N}{2} \sqrt{\frac{k}{L}} \\ R_{k_z}(k) &= \alpha \cdot \frac{kM}{2L} + (1 - \alpha) \cdot \frac{M}{2} \sqrt{\frac{k}{L}} \end{aligned} \right\} \quad (\text{A.1})$$

where $N \times M$ is the size of the image, k represents the number of the ring ($k = 1, 2, \dots, L$) and $0 \leq \alpha \leq 1$.

It is easy to check that a value of α equal to zero produces rings with constant area while a value of α equal to one produces rings with constant radial width but with increasing area when moving to the periphery of the k-space. Since each sector will be sampled an equal number of times, the case $\alpha = 0$ yields uniform sampling of the k-space, while in the case $\alpha = 1$ the sampling density decreases at the periphery. Thus, the parameter α enables the selection from an uniform —or quasi-uniform— sampling pattern of k-space to a denser sampling in its center.

The samples within each ring are ordered first by radius and second by angle in the k-space. Afterwards, trajectories are formed by choosing each time one sample of one ring and sector forming a spiral twist (for example, (sector, ring)=(l, l), $1 \leq l \leq L$, then (sector, ring)=($l, l + 1$), $1 \leq l \leq L - 1$ and so forth). Finally, the resulting trajectories are ordered according to the golden-angle (137.5°). The number of total acquired samples is adjusted by the desired AF.

Appendix *B*

REGULARIZATION PARAMETER SELECTION

B.1 Introduction

Establishing the regularization parameter in a cardiac CINE MRI reconstruction problem is not an easy task and, furthermore, it is decisive, due to the fact that, if the chosen value is too large, reconstructed images with less artifacts are obtained, but motion can also be reduced; whereas if the value of the regularization parameter is chosen too small, the motion will be preserved, but artifacts will be hardly eliminated. Therefore, an intermediate situation would be ideal.

In this Appendix a method to select the regularization parameter is proposed, specially when the number of available images is scarce. Roughly, the proposed approach can be described this way: the images are reconstructed using some different regularization parameters, that have been previously chosen. Afterwards, these reconstructed images are divided into training and test groups and a quality metric is computed (in this Thesis SER, HFSE and RMSE between displacement fields have been used as quality metrics). By means of a cross-validation methodology, the regularization parameter that maximizes the former metric within the test groups is selected, so that a compromise between the two situations explained in the previous paragraph may be achieved.

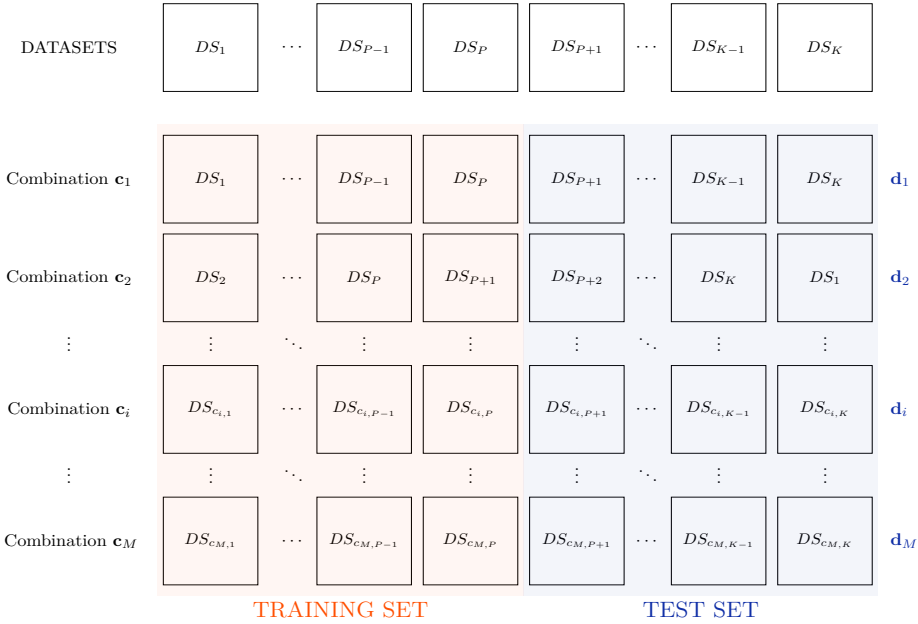


Figure B.1: Division of the datasets into both training and test sets of the regularization parameter selection method. Note that $M = \binom{K}{P}$.

Details as well as the mathematical description of the procedure are given in the next section.

B.2 Description of the procedure

In the first place a set of N tentative values for the regularization parameter vector $\boldsymbol{\mu} = (\mu_1, \dots, \mu_n) \in \mathbb{R}^n$ is defined, as well as a similarity metric $V(\boldsymbol{\mu})$ to measure the affinity between the set of reconstructed images with respect to a reference one. Let K denote the number of datasets available and let $k \in \{1, \dots, K\}$. In a pre-training phase (see Figure B.2), an image $\mathbf{m}_k^{rec}(\boldsymbol{\mu}_i)$ is reconstructed for each dataset k and each tentative vector $\boldsymbol{\mu}_i$ ($1 \leq i \leq N$). After that, the similarity metric, $V_k(\mu_i)$, is computed within a ROI that contains the heart for each of those reconstructions. The $\boldsymbol{\mu}_i$

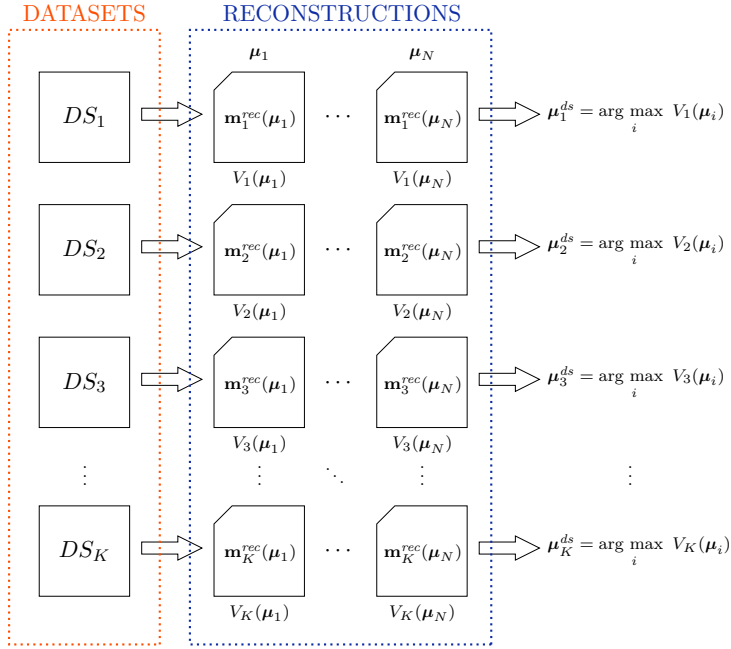


Figure B.2: Pre-training phase of the regularization parameter selection method.

that gives rise to the highest $V(\boldsymbol{\mu})$ value is then selected for dataset k :

$$\boldsymbol{\mu}_k^{ds} = \arg \max_i V_k(\boldsymbol{\mu}_i) \quad (\text{B.1})$$

Later on, a cross validation method is used to determine the optimum vector, i.e., $\boldsymbol{\mu}_{opt}$. This method can be described as follows: The K datasets are divided into P training datasets and $(K - P)$ test datasets (see Figure B.1). In order to avoid any sort of bias, exhaustiveness in the number $M = \binom{K}{P}$ of different combinations is suggested. Let \mathbf{c}_i denote the group of training datasets included in combination i ($1 \leq i \leq M$) and let c_{ij} denote the index in the set $\{1, \dots, K\}$ of the j -th element of \mathbf{c}_i ($1 \leq j \leq P$), i.e., $c_{ij} \in \{1, \dots, K\}$. For this j -th element its associated $\boldsymbol{\mu}_{c_{ij}}^{ds}$ is taken and is used to reconstruct all other datasets in \mathbf{c}_i (see Figure B.3). Afterwards,

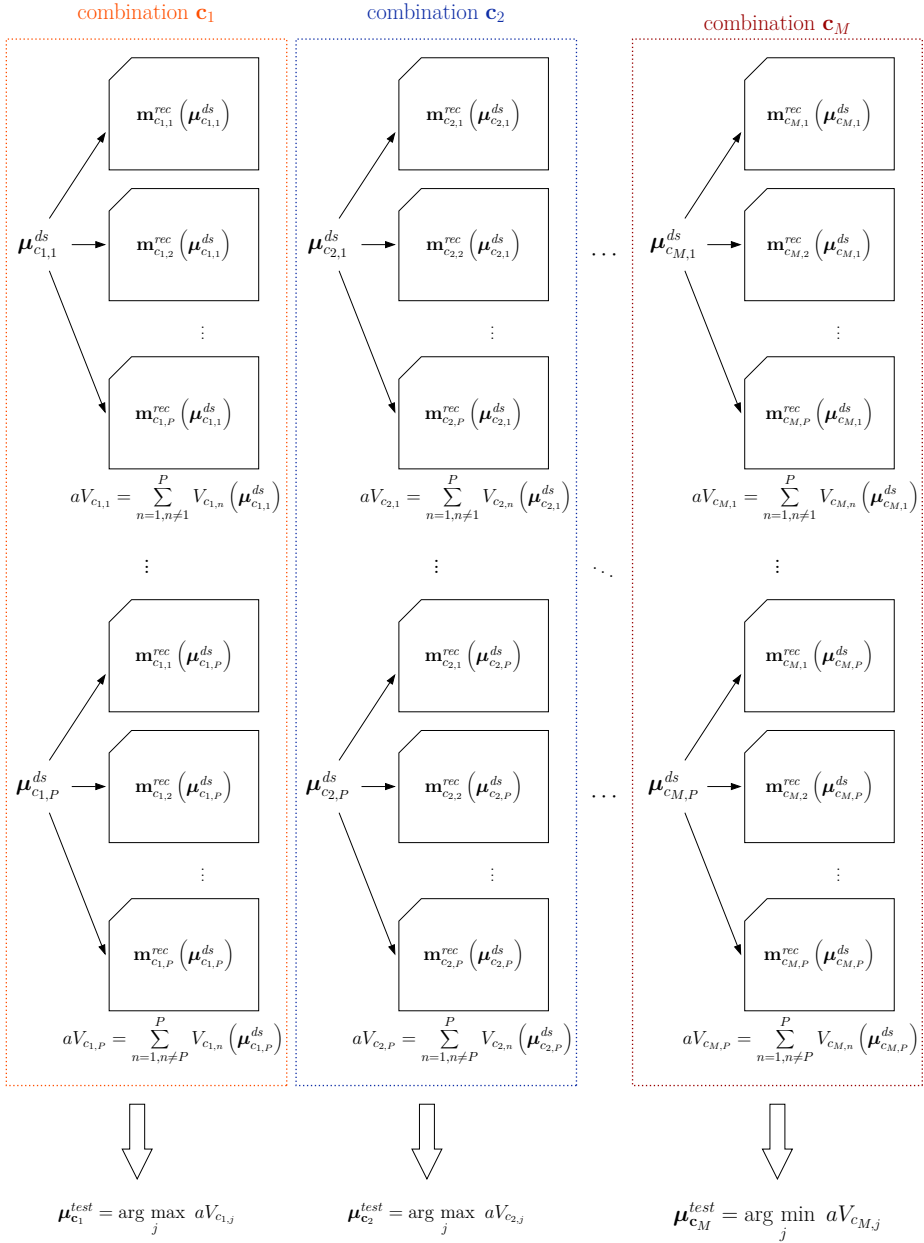


Figure B.3: Training phase of the regularization parameter selection method.

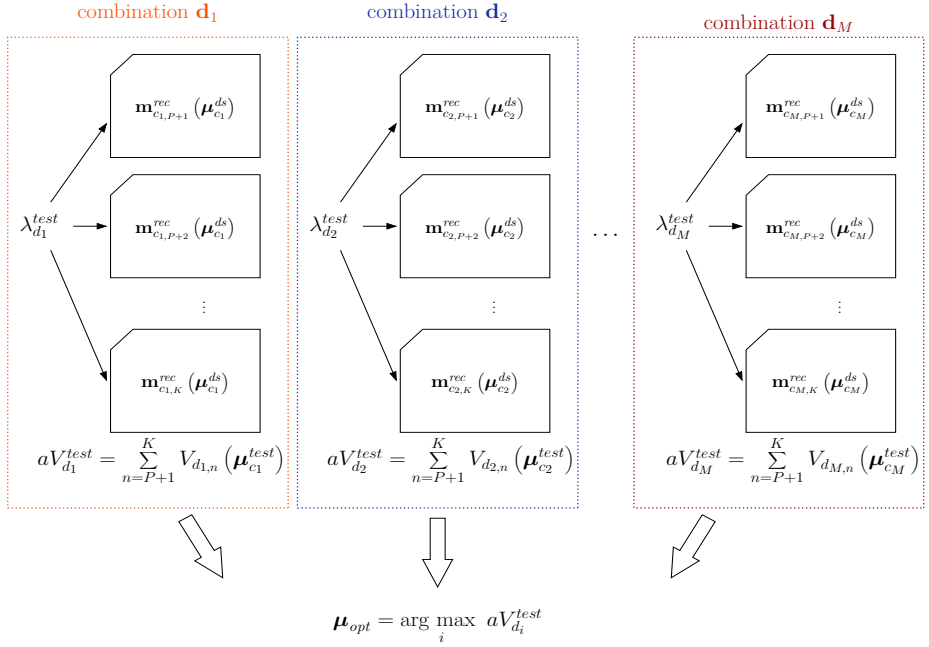


Figure B.4: Test phase of the regularization parameter selection method. Note that $M = \binom{K}{P}$.

the accumulated similarity metric $aV(\boldsymbol{\mu})$ is calculated:

$$aV_{c_i, j} = \sum_{n=1, n \neq j}^P V_{c_i, n}(\boldsymbol{\mu}_{c_i, j}^{ds}). \quad (\text{B.2})$$

For each training group \mathbf{c}_i we select the candidate $\boldsymbol{\mu}_{\mathbf{c}_i}^{test}$ by maximizing the accumulated similarity metric $aV(\boldsymbol{\mu})$ within \mathbf{c}_i , i.e.,

$$\boldsymbol{\mu}_{\mathbf{c}_i}^{test} = \arg \max_j aV_{c_i, j} \quad (\text{B.3})$$

The final step to determine $\boldsymbol{\mu}_{opt}$ (see Figure B.4) is to select the best $\boldsymbol{\mu}_{\mathbf{c}_i}^{test}$ with $1 \leq i \leq M$. Let \mathbf{d}_i denote the group of datasets not included in \mathbf{c}_i (i.e., the testing datasets associated to the training set \mathbf{c}_i); correspondingly, let d_{ij} denote the index in the set $\{1, \dots, K\}$ of the j -th element of \mathbf{d}_i

($1 \leq j \leq K - P$). The accumulated similarity metric $aV(\lambda)$ is calculated as follows:

$$aV_{\mathbf{d}_i}^{test} = \sum_{n=1}^{K-P} V_{d_{i,n}}(\boldsymbol{\mu}_{\mathbf{c}_i}^{test}) \quad (\text{B.4})$$

With these values \mathbf{d}_i^{test} , ($1 \leq i \leq M$), the optimum value is selected as

$$\boldsymbol{\mu}_{opt} = \arg \max_i aV_{\mathbf{d}_i}^{test} \quad (\text{B.5})$$

Appendix C

GRADIENT CALCULATION OF THE COST FUNCTION FOR ELASTIC ALIGNEDSENSE

C.1 Introduction

The calculation of the gradient of the cost function is a key point in any reconstruction problem. In the case of the EAS, the cost function has associated an image registration component. This makes the calculation of the gradient quite challenging, due to the fact that computational cost and execution times may increase considerably.

In this Thesis, the convolutional implementation of the B-spline based FFD model by means of 1D convolutions proposed in [106] has been adopted. This technique takes advantage of the limited number of points in which operators are defined and the high optimization of the convolution that different development environments have achieved during the last years. Therefore, computational cost and execution times can be reduced. However, one must be careful when obtaining the analytical expression of the gradient of the cost function, since elements in both k-space and image space may be mixed, so that the previous technique cannot be applied. In this Appendix how the gradient can be obtained in order to apply the efficient implementation technique from above is explained.

C.2 Calculation

The cost function, $\mathcal{C}(\Theta)$, for the elastic alignedSENSE problem has been defined as follows:

$$\begin{aligned} \mathcal{C}(\Theta) &= \|\mathbf{A}\mathcal{F}\mathbf{S}\mathbf{m}(\mathbf{T}_\Theta) - \mathbf{y}\|^2 + \lambda \|\nabla_{\mathbf{x}}\mathbf{m}\|^2 + \mathcal{R}_3(\Theta) = \\ &= \|\mathbf{E}\mathbf{m}(\mathbf{T}_\Theta) - \mathbf{y}\|^2 + \lambda \|\nabla_{\mathbf{x}}\mathbf{m}\|^2 + \mathcal{R}_3(\Theta) = \\ &= \mathcal{V}(\Theta) + \lambda \|\nabla_{\mathbf{x}}\mathbf{m}\|^2 + \mathcal{R}_3(\Theta) \end{aligned} \quad (\text{C.1})$$

where $\mathbf{m}(\mathbf{T}_\Theta) \equiv \mathbf{m}(\mathbf{T}_\Theta(\mathbf{x}))$ and $\mathbf{x} \in \mathbb{R}^2$ represents the spatial coordinates in the space of each frame image. The parameters that define the transformation are $\Theta = \{\theta_1, \dots, \theta_N\}$, with each $\theta_n = \{\theta_{n_1}, \dots, \theta_{n_u}, \dots, \theta_{n_K}\}$, and $\theta_{n_u} = (\theta_{nu_1}, \theta_{nu_2})$, which corresponds to the parameters that characterize each node in the B-Spline FFD model described in Section 2.3.5.2, N is the number of frames and K is the number of control points. Furthermore, the calculation shown in this Appendix will be focused only on the derivative of the first term of Eq. (C.1), $\mathcal{V}(\Theta)$:

$$\begin{aligned} \frac{\partial \mathcal{V}(\Theta)}{\partial \theta_{nu_l}} &= \frac{\partial}{\partial \theta_{nu_l}} \left(\mathbf{m}^H(\mathbf{T}_\Theta) \mathbf{E}^H - \mathbf{y}^H \right) \left(\mathbf{E}\mathbf{m}(\mathbf{T}_\Theta) - \mathbf{y} \right) = \\ &= \frac{\partial}{\partial \theta_{nu_l}} \left(\mathbf{m}^H(\mathbf{T}_\Theta) \mathbf{E}^H \mathbf{E}\mathbf{m}(\mathbf{T}_\Theta) - \mathbf{m}^H(\mathbf{T}_\Theta) \mathbf{E}^H \mathbf{y} - \right. \\ &\quad \left. - \mathbf{y}^H \mathbf{E}\mathbf{m}(\mathbf{T}_\Theta) + \mathbf{y}^H \mathbf{y} \right) = \\ &= \frac{\partial \mathcal{V}_1(\Theta)}{\partial \theta_{nu_l}} - \frac{\partial \mathcal{V}_2(\Theta)}{\partial \theta_{nu_l}} - \frac{\partial \mathcal{V}_3(\Theta)}{\partial \theta_{nu_l}} + \frac{\partial \mathcal{V}_4(\Theta)}{\partial \theta_{nu_l}} \end{aligned} \quad (\text{C.2})$$

where the index u_l denotes the position of the control point within the whole set of control points Θ and n denotes the frame number.

If $\mathbf{x}' = \mathbf{T}_\Theta(\mathbf{x}) \in \mathbb{R}^2$, $[\mathbf{x}']_l$ ($1 \leq l \leq 2$) represents the l -component of the vector \mathbf{x}' and ‘ \odot ’ denotes the Hadamard product, we obtain

$$\frac{\partial \mathbf{m}(\mathbf{T}_\Theta)}{\partial \theta_{nu_l}} = \frac{\partial \mathbf{m}(\mathbf{x}')}{\partial [\mathbf{x}']_l} \odot \frac{\partial \mathbf{T}_\Theta(\mathbf{x})}{\partial \theta_{nu_l}} \equiv \frac{\partial \mathbf{m}}{\partial [\mathbf{x}']_l} \odot \frac{\partial \mathbf{T}_\Theta}{\partial \theta_{nu_l}} \quad (\text{C.3})$$

by applying the chain rule to each component of the vector $\mathbf{m}(\mathbf{T}_\Theta(\mathbf{x}))$ and taking into account that only the component $[\mathbf{x}']_l$ depends on the parameter θ_{nu_l} .

$$\begin{aligned} \frac{\partial \mathcal{V}_1(\Theta)}{\partial \theta_{nu_l}} &= \frac{\partial}{\partial \theta_{nu_l}} \left(\mathbf{m}^H(\mathbf{T}_\Theta) \mathbf{E}^H \mathbf{E} \mathbf{m}(\mathbf{T}_\Theta) \right) = \\ &= \left[\frac{\partial \mathbf{m}}{\partial [\mathbf{x}']_l} \odot \frac{\partial \mathbf{T}_\Theta}{\partial \theta_{nu_l}} \right]^H \mathbf{E}^H \mathbf{E} \mathbf{m}(\mathbf{T}_\Theta) + \\ &\quad + \mathbf{m}^H(\mathbf{T}_\Theta) \mathbf{E}^H \mathbf{E} \left[\frac{\partial \mathbf{m}}{\partial [\mathbf{x}']_l} \odot \frac{\partial \mathbf{T}_\Theta}{\partial \theta_{nu_l}} \right] = \\ &= \mathbf{z}_1^H + \mathbf{z}_1 \end{aligned} \tag{C.4a}$$

$$\begin{aligned} \frac{\partial \mathcal{V}_2(\Theta)}{\partial \theta_{nu_l}} &= \frac{\partial}{\partial \theta_{nu_l}} \left(\mathbf{m}^H(\mathbf{T}_\Theta) \mathbf{E}^H \mathbf{y} \right) = \left[\frac{\partial \mathbf{m}}{\partial [\mathbf{x}']_l} \odot \frac{\partial \mathbf{T}_\Theta}{\partial \theta_{nu_l}} \right]^H \mathbf{E}^H \mathbf{y} = \\ &= \mathbf{z}_2^H \end{aligned} \tag{C.4b}$$

$$\begin{aligned} \frac{\partial \mathcal{V}_3(\Theta)}{\partial \theta_{nu_l}} &= \frac{\partial}{\partial \theta_{nu_l}} \left(\mathbf{y}^H \mathbf{E} \mathbf{m}(\mathbf{T}_\Theta) \right) = \mathbf{y}^H \mathbf{E} \left[\frac{\partial \mathbf{m}}{\partial [\mathbf{x}']_l} \odot \frac{\partial \mathbf{T}_\Theta}{\partial \theta_{nu_l}} \right] = \\ &= \mathbf{z}_2 \end{aligned} \tag{C.4c}$$

$$\frac{\partial \mathcal{V}_4(\Theta)}{\partial \theta_{nu_l}} = \frac{\partial}{\partial \theta_{nu_l}} \left(\mathbf{y}^H \mathbf{y} \right) = \mathbf{0} \tag{C.4d}$$

Combining Eq. (C.2) and Eqs. (C.4), we obtain:

$$\begin{aligned} \frac{\partial \mathcal{V}(\Theta)}{\partial \theta_{nu_l}} &= \mathbf{z}_1^H + \mathbf{z}_1 - \mathbf{z}_2^H - \mathbf{z}_2 = (\mathbf{z}_1 - \mathbf{z}_2) + (\mathbf{z}_1 - \mathbf{z}_2)^H = \\ &= 2 \cdot \Re\{\mathbf{z}_1 - \mathbf{z}_2\} \end{aligned} \tag{C.5}$$

Depending on how \mathbf{z}_1 and \mathbf{z}_2 are chosen in Eqs. (C.4), two main possible

solutions arise:

$$\begin{aligned} \frac{\partial \mathcal{V}(\Theta)}{\partial \theta_{nu_l}} &= 2 \cdot \Re \left\{ \left[\frac{\partial \mathbf{m}}{\partial [\mathbf{x}'_l]} \odot \frac{\partial \mathbf{T}_\Theta}{\partial \theta_{nu_l}} \right]^H \mathbf{E}^H (\mathbf{E} \mathbf{m}(\mathbf{T}_\Theta) - \mathbf{y}) \right\} = \\ &= 2 \cdot \Re \left\{ \left[\frac{\partial \mathbf{m}}{\partial [\mathbf{x}'_l]} \odot \frac{\partial \mathbf{T}_\Theta}{\partial \theta_{nu_l}} \right]^H \mathbf{E}^H \mathbf{r} \right\} \end{aligned} \quad (\text{C.6a})$$

or,

$$\begin{aligned} \frac{\partial \mathcal{V}(\Theta)}{\partial \theta_{nu_l}} &= 2 \cdot \Re \left\{ (\mathbf{E} \mathbf{m}(\mathbf{T}_\Theta) - \mathbf{y})^H \mathbf{E} \left[\frac{\partial \mathbf{m}}{\partial [\mathbf{x}'_l]} \odot \frac{\partial \mathbf{T}_\Theta}{\partial \theta_{nu_l}} \right] \right\} = \\ &= 2 \cdot \Re \left\{ \mathbf{r}^H \mathbf{E} \left[\frac{\partial \mathbf{m}}{\partial [\mathbf{x}'_l]} \odot \frac{\partial \mathbf{T}_\Theta}{\partial \theta_{nu_l}} \right] \right\} \end{aligned} \quad (\text{C.6b})$$

As mentioned in Section 2.3.5.2, B-splines have compact support and so do their derivatives. Therefore, the derivative component of the previous group of Eqs. (C.6), $\frac{\partial \mathbf{T}_\Theta}{\partial \theta_{nu_l}}$, only depends of the position of the control points and the distance between them. Thus, this calculation can be efficiently made by means of convolution, as described in [106]. The Eq. (C.6a) allows to obtain the cost gradient by means of sucesive 1D convolutions in the image domain, where as in Eq. (C.6b), it is not posible, since components in both the image and k-space domains are mixed when convolution must be applied, so that other approaches that imply, for example, pixelwise iterations should be used instead.

Appendix *D*

RECOVERING A CARDIAC SYNCHRONISM SIGNAL FROM K-SPACE DATA IN CARDIAC CINE MRI

D.1 Introduction

Cardiac CINE MRI involves long examination times and elaborated setups. Specifically, additional hardware is required, such as ECG and respiratory belts. The ECG is used to synchronize the acquisition of MRI data with the cardiac beating and respiratory belts are used as respiration sensors to avoid artifacts produced by respiratory motion. However, these external devices increase the examination, preparation and acquisition times [107, 108]. Moreover, the ECG in high field MRI systems can be severely corrupted by induced electromagnetic signals and the magneto-hydro-dynamic effect [109].

In this Appendix an automatic method to recover the cardiac synchronization signal directly from the k-space data is proposed, so that the need of additional hardware in cardiac MRI examinations can be avoided. The procedure has been tested via numerical simulation and with real data, both in BH and FB acquisitions.

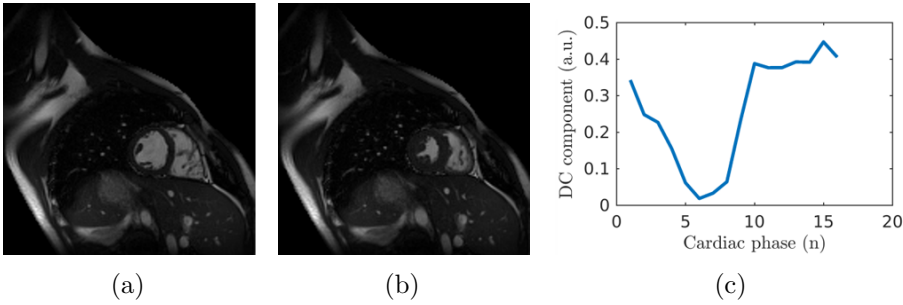


Figure D.1: Diastolic (a) and systolic (b) cardiac phases in a cardiac CINE exam. Evolution of the average intensity value along the cardiac cycle (c). Minimum corresponds to the systolic phase shown. “a.u.” stands for *arbitrary unit*.

D.2 Theory

In cardiac CINE MRI a set of images along the cardiac cycle are obtained enabling the visualization of the motion of the heart. In these images, blood typically appears bright, surrounded by darker regions (mainly myocardium, lungs, and liver). Therefore, a cardiac contraction will translate into a decrease on the average intensity value of each image (DC component) along the cardiac cycle (Figure D.1). Since the k -space data is related to the final images via the Fourier transform, the evolution of DC component of the images along time is contained in the central position of the k -space, which is more frequently sampled when radial trajectories are used. Consequently, the proposed methodology for the recovery of the cardiac synchronization information is based on the processing of the signal formed by the central samples of the k -space along time. In FB scenarios, the change of volume of the lungs will also affect the DC value of the images. Therefore, breathing dynamics will be present in the signal as well. As a preprocessing step, this signal is band-pass filtered between 0.1 Hz and 1.5 Hz, where most of the cardiac and respiratory activities are contained. A peak detection algorithm is then applied to identify cardiac cycles.

D.2.1 Coil selection

k-space data are usually acquired simultaneously with several coils, which are placed all over the chest. Given the spatial distribution of the antennas, some of them will provide, therefore, more useful information for the recovery of the cardiac signal than others (Figure D.2). A method to automatically select the best coil in these sense is a key component of the proposed method. Two different approaches are presented:

- Automatic selection based on spectral analysis: the ratio between the average of the spectrum of the signal in the [0.5-1.5 Hz] and [0.1-0.5 Hz] bands is calculated. Those spectral bands correspond to the frequencies of the cardiac cycle and respiratory cycle, respectively. The coil that provides the highest value of this ratio is selected. In this approach, only the information from one coil is used for signal recovery.
- PCA approach: by means of PCA, most of the common dynamic cardiac information that is *distributed* among the different coils may be concentrated in the first principal components of the multicoil DC signal.

D.3 Materials and Methods

Four healthy volunteers with ages ranging 24-29 were scanned with a 32-elements cardiac coil on a 1.5 T Philips scanner and a bSSFP sequence. The acquisitions were performed in three different scenarios:

D.3.1 Cartesian, breath-hold acquisition

A standard Cartesian acquisition in BH was performed. Relevant acquisition parameters include $TR/TE = 2.9 \text{ ms}/1.44 \text{ ms}$, flip angle of 60° , field of

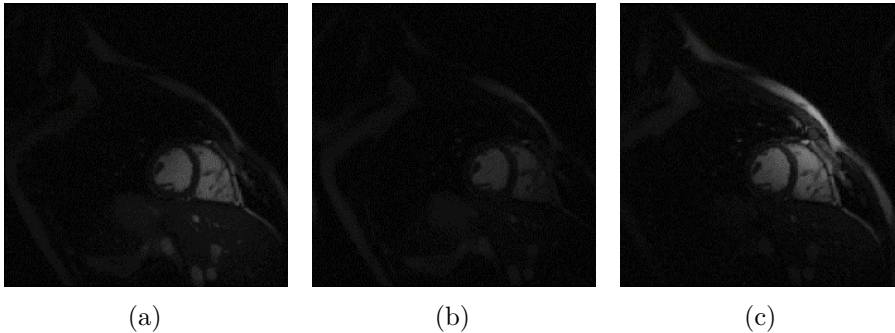


Figure D.2: Coil selection. The images obtained from three different coils are represented. The image in (b) is discarded because of its low brightness. The coil in (c) is more focused on the external area than the coil in (a), which is more focused on the heart. Therefore, the coil in (a) will be preferred.

view (FOV) = 320×320 mm², spatial resolution = 2×2 mm. 20 cardiac phases were reconstructed.

D.3.2 Golden-radial breath-hold acquisition

A golden-radial acquisition [24] was performed in BH with similar parameters than in the Cartesian case. Total acquisition time was approximately 12 seconds and a total number of 4000 projections were acquired. The first 400 projections were discarded in order to guarantee that the stationary state was reached.

Contrary to Cartesian, in a radial acquisition each line passes through the center of the k -space. The three central samples along each line were averaged in order to correct possible misalignments with respect to the center of the k -space, due to gradient errors and eddy currents, and considered as the DC component.

D.3.3 Golden-radial free breathing acquisition

An additional golden-radial acquisition was performed with similar parameters in FB to analyze the influence of the respiration in the recovery of

the cardiac signal.

In all the scenarios, an ECG signal was recorded simultaneously with the data and used as a ground truth. In order to validate the proposed methods in the different scenarios, the following error measure has been defined:

$$Error = \frac{RR_{ECG} - RR_{MRI}}{RR_{ECG}}$$

where RR_{ECG} is the RR interval obtained from the ECG signal of reference and RR_{MRI} is the interval acquired from the cardiac cycle signal obtained from the MRI data.

D.4 Results

Figure D.3 shows the cardiac cycle signals obtained from Cartesian real data in both BH and FB. Only the data from a single coil were manually selected. To select the coil, the images resulting from each coil were represented and visually inspected. The coil that provided an image that showed a better compromise between brightness and direction (that is, the coil that was more focused on the heart region) was selected (Figure D.2). In the plotted signal, cardiac dynamics are clearly appreciable, with an abrupt decrease of its value indicating ventricle contraction.

With respect to golden radial acquisitions, Figure D.4 shows the cardiac signal obtained from the golden radial data only for the FB case, for the sake of conciseness. Data from only one coil was automatically selected applying the automatic method described in Section D.2 based on spectral analysis. The peak detection algorithm was adapted to allow RR intervals between 0.5 and 1.2 seconds, corresponding to heart rates between 50 and 120 BPM. Then the obtained RR-intervals were compared with the RR-intervals obtained from the ECG signal of reference.

In the FB scenario, the band-pass filter to use is adapted to mitigate the influence of the respiratory component in the cardiac signal and a

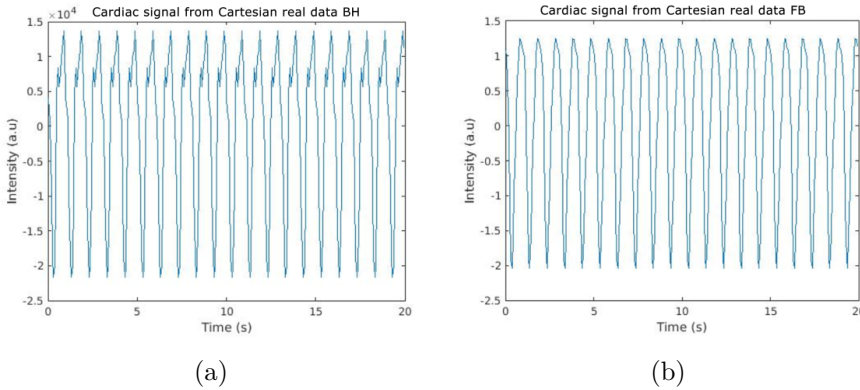


Figure D.3: Cardiac cycle signals obtained from Cartesian real data in a BH situation (a) and in a FB situation (b). “a.u.” stands for *arbitrary unit*.

higher cutoff frequency to collect additional harmonics of the cardiac cycle signal at higher frequencies. Its original spectrum, obtained by means of the FFT, and the signal obtained after filtering are also represented in Figure D.4.

An error of 2.0589% in BH situation is achieved, calculated using the metric defined above. Before adapting the filter as described, the error in the FB case was as high as 30.8826%. After readjusting the filter and inverting the signal to detect the minima of the resulting signal instead of the maxima, an error of 1.6271% is obtained.

Finally, the PCA approach was applied to the FB golden-radial data. In this scenario all the information provided by the 32 coils from the previous data set is used by applying a PCA approach. In a first step, the first PCA component is used to obtain the cardiac cycle signal. In order to test the hypothesis that the first principal component gathers most of the cardiac information, the automatic coil selection approach based on spectral analysis applied to all the PCA components is applied.

Results are summarized in Table D.1, which shows the error between manual and automatic selection of a single coil and for PCA based approach. The second column shows the error obtained when the coil was

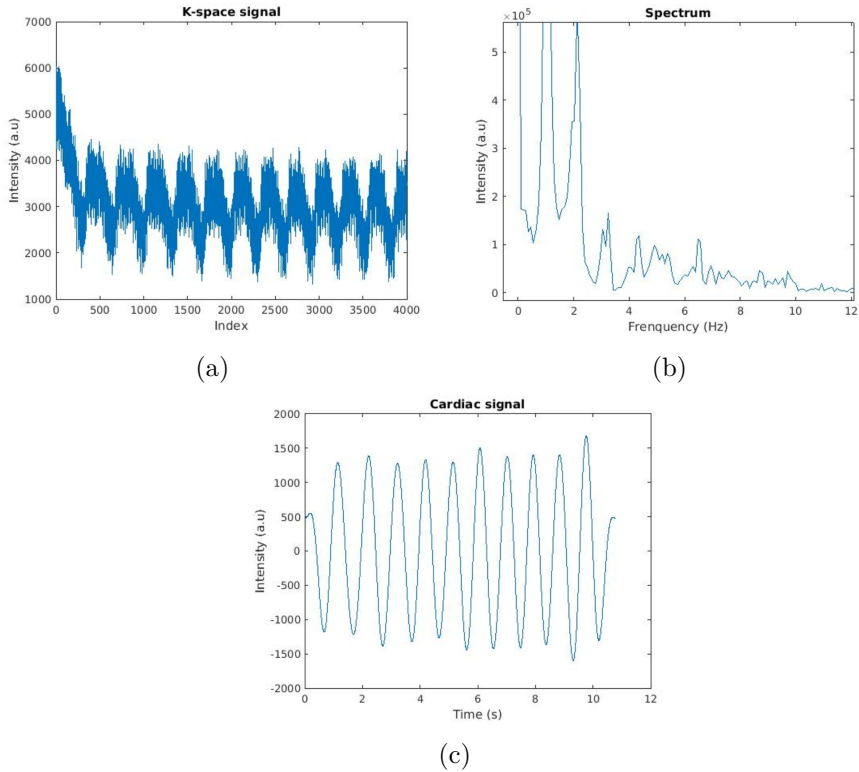


Figure D.4: Cardiac cycle signals recovered from golden radial real data. In (a) the signal obtained before filtering is represented (only the real part of the complex signal is considered); in (b) its spectrum, calculated by applying the FFT, is represented; and in (c), the cardiac cycle signal after filtering is shown in the time domain.

selected manually by visual inspection. The number preceded by the ‘#’ symbol represents the number of the selected coil. In the third column, the results from the method described in Section D.2 are shown. In the fourth column, the results obtained from the PCA approach are shown. The number preceded by a ‘C’ letter means the selected PCA component by the automatic method based on spectral analysis. The results from selecting the first PCA component (C1) are also shown for comparison. Finally, in the fifth column the results of the PCA approach with a previous

Table D.1: Error comparison (in percentage) between manual and automatic selection and between single or multi-coil methods. The ‘#’ symbol represents the number of the selected coil, whereas the ‘C’ letter means the selected PCA component.

Subject	Visual inspection	Automatic selection	PCA	PCA after filtering
1	#5: 1.63%	#13: 2.514%	C1: 3.04% C5: 2.34%	2.65 %
2	#12: 0.93%	#11: 0.984%	C1: 2.40% C4: 1.45%	1.37 %
3	#14: 1.40%	#13: 3.103%	C1: 4.39% C8: 1.97%	3.20 %
4	#4: 3.56%	#5: 3.731%	C1: 7.57% C2: 3.40%	3.88 %

filtering of the data and automatic selection of the PCA component are presented.

D.5 Discussion

In the first scenario with Cartesian data, the cardiac cycle signal can be easily obtained by extracting the zero frequency component along time in a BH situation. The RR-intervals were relatively constant due to the fact that influence of respiration is not included, although the intrinsic heart rate variability was present. However, in a FB situation the cardiac cycle signal was affected by the respiratory signal. A band pass filter (cutoff frequencies 1 and 2.5 Hz) was used to remove the respiratory signal. Since the results were not accurate enough, different band-pass filters with different cutoff frequencies were used until the desired accuracy was achieved.

For BH golden-radial acquisitions, the filtering method has shown good results and allows us to recover the RR intervals with enough accuracy. When switching to a FB scenario, and after applying the described modifications in the filtering procedure, the error between automatic selection

of one coil and filtering before the PCA approach look similar. It can be presumed, that if more subjects had participated, this slight difference may be included in the standard deviation. Concerning the resulting images from coils, it is really difficult to clearly detect differences between the optimal coil and the two other coils selected by an automatic approach. However, it seems that the best choice between these proposed methods is the PCA approach after filtering the data, since the information of all coils is combined. This also makes sense because some noise is removed, which can affect negatively to the resulting PCA directions.

Another important point in this discussion is that the recovered signals are not in the same cardiac phase when the image is reconstructed, since an offset is introduced between the peaks detected in the real ECG signal and the one recovered from the k-space data. This fact is not a big deal, as the information reside in the RR interval series.

Bibliography

- [1] F. Bloch. Nuclear induction. *Physical Review*, 70:460–474, 1946.
- [2] R. Damadian. Tumor detection by nuclear magnetic resonance. *Science*, 171(3976):1151–1153, 1971.
- [3] C. Constantine, K. Shan, S. D. Flamm, and M. U. Sivananthan. Role of MRI in clinical cardiology. *The Lancet*, 363(9427):2162–2171, 2004.
- [4] A. F. Frangi, W. J. Niessen, and M. A. Viergever. Three-dimensional modeling for functional analysis of cardiac images, a review. *IEEE Transactions on Medical Imaging*, 20(1):2–5, 2001.
- [5] J. Jeudy and C. S. White. Cardiac magnetic resonance imaging: Techniques and principles. *Seminars in Roentgenology*, 43(3):173–182, 2008.
- [6] H. Mojibian and H. Pouraliakbar. Chapter 8 - Cardiac magnetic resonance imaging. In *Practical Cardiology*, pages 159–166. Elsevier, 2018.
- [7] M. P. Pfeiffer and R. W. W. Biederman. Cardiac MRI: A general overview with emphasis on current use and indications. *Medical Clinics of North America*, 99(4):849–861, 2015.
- [8] L. Feng, M. B. Srichai, R. P. Lim, A. Harrison, W. King, G. Adluru, E. V. R. Dibella, D. K. Sodickson, R. Otazo, and D. Kim. Highly accelerated real-time cardiac CINE MRI using k-t SPARSE-SENSE. *Magnetic Resonance in Medicine*, 70(1):64–74, 2013.

- [9] A. D. Scott, J. Keegan, and D. N. Firmin. Motion in cardiovascular MR imaging. *Radiology*, 250(2):331–351, 2009.
- [10] C. Catana. Motion correction options in PET/MRI. *Seminars in Nuclear Medicine*, 45(3):212–223, 2015.
- [11] R. M. Menchón-Lara, J. Royuela-del Val, A. Godino-Moya, L. Cordero-Grande, F. Simmross-Wattenberg, M. Martín-Fernández, and C. Alberola-López. *An efficient multi-resolution reconstruction scheme with motion compensation for 5D free-breathing whole-heart MRI*, volume 10555 LNCS of *Lecture Notes in Computer Science*, pages 136–145. Springer Verlag, Germany, 2017.
- [12] W. P. Segars, G. Sturgeon, S. Mendonca, J. Grimes, and B. M. W. Tsui. 4D XCAT phantom for multimodality imaging research. *Medical Physics*, 37(9):4902–4915, 2010.
- [13] L. Wissmann, C. Santelli, W. Segars, and S. Kozerke. MRXCAT: Realistic numerical phantoms for cardiovascular magnetic resonance. *Journal of Cardiovascular Magnetic Resonance*, 16:63, 2014.
- [14] Z. P. Liang and P. C. Lauterbur. *Principles of magnetic resonance imaging: A signal processing perspective*. IEEE Press Series on Biomedical Engineering. Wiley, 1999.
- [15] L. G. Hanson. Is quantum mechanics necessary for understanding magnetic resonance? *Concepts in Magnetic Resonance Part A*, 32A(5):329–340, 2008.
- [16] L. Hanson. Introduction to magnetic resonance imaging techniques. *Education Matters*, pages 1–48, 2009.
- [17] G. Chavhan, P. Babyn, B. Thomas, M. Shroff, and M. Haacke. Principles, techniques, and applications of T2*-based MR imaging and its special applications. *Radiographics*, 29:1433–49, 2009.

- [18] P. C. Lauterbur. Image formation by induced local interactions: Examples employing nuclear magnetic resonance. *Nature*, 242(5394):190–191, 1973.
- [19] W. A. Edelstein, J. M. S. Hutchison, G. Johnson, and T. Redpath. Spin warp NMR imaging and applications to human whole-body imaging. *Physics in Medicine and Biology*, 25(4):751–756, 1980.
- [20] C. A. Baron, N. Dwork, J. M. Pauly, and D. G. Nishimura. Rapid compressed sensing reconstruction of 3D non-Cartesian MRI. *Magnetic Resonance in Medicine*, 79(5):2685–2692, 2018.
- [21] K. T. Block, H. Chandarana, S. Milla, M. Bruno, T. Mulholland, G. Fatterpekar, M. Hagiwara, R. Grimm, C. Geppert, B. Kiefer, and D. K. Sodickson. Towards routine clinical use of radial stack-of-stars 3D gradient-echo sequences for reducing motion sensitivity. *Journal of the Korean Society of Magnetic Resonance in Medicine*, 18(2):87–106, 2014.
- [22] M. K. Stehling, R. Turner, and P. Mansfield. Echo-planar imaging: Magnetic resonance imaging in a fraction of a second. *Science*, 254(5028):43–50, 1991.
- [23] M. Lauzon and B. Rutt. Effects of polar sampling in k-space. *Magnetic Resonance in Medicine*, 36:940–949, 1996.
- [24] S. Winkelmann, T. Schaeffter, T. Koehler, H. Eggers, and O. Doessel. An optimal radial profile order based on the golden ratio for time-resolved MRI. *IEEE Transactions on Medical Imaging*, 26(1):68–76, 2007.
- [25] C. B. Ahn, J. H. Kim, and Z. H. Cho. High-speed spiral-scan echo planar NMR Imaging–I. *IEEE Transactions on Medical Imaging*, 5(1):2–7, 1986.

- [26] E. Yudilevich and H. Stark. Spiral sampling in magnetic resonance imaging - the effect of inhomogeneities. *IEEE Transactions on Medical Imaging*, 6(4):337–345, 1987.
- [27] P. Irarrazabal and D. G. Nishimura. Fast three dimensional magnetic resonance imaging. *Magnetic Resonance in Medicine*, 33(5):656–662, 1995.
- [28] X. Feng, M. Salerno, C. M. Kramer, and C. H. Meyer. Non-Cartesian balanced steady-state free precession pulse sequences for real-time cardiac MRI. *Magnetic Resonance in Medicine*, 75(4):1546–1555, 2016.
- [29] H. Tan and C. H. Meyer. Estimation of k-space trajectories in spiral MRI. *Magnetic Resonance in Medicine*, 61(6):1396–1404, 2009.
- [30] M. O. Addy, H. H. Wu, and D. G. Nishimura. Simple method for MR gradient system characterization and k-space trajectory estimation. *Magnetic Resonance in Medicine*, 68(1):120–129, 2012.
- [31] A. E. Campbell-Washburn, H. Xue, R. J. Lederman, A. Z. Faranesh, and M. S. Hansen. Real-time distortion correction of spiral and echo planar images using the gradient system impulse response function. *Magnetic Resonance in Medicine*, 75(6):2278–2285, 2016.
- [32] D. Piccini, A. Littmann, S. Nielles-Vallespin, and M. O. Zenge. Spiral phyllotaxis: The natural way to construct a 3D radial trajectory in MRI. *Magnetic Resonance in Medicine*, 66(4):1049–1056, 2011.
- [33] F. Han, Z. Zhou, M. Cao, Y. Yang, K. Sheng, and P. Hu. Respiratory motion-resolved, self-gated 4D-MRI using rotating cartesian k-space (ROCK). *Medical Physics*, 44(4):1359–1368, 2017.
- [34] J. Y. Cheng, T. Zhang, N. Ruangwattanapaisarn, M. T. Alley, M. Uecker, J. M. Pauly, M. Lustig, and S. S. Vasanawala. Free-

- breathing pediatric MRI with nonrigid motion correction and acceleration. *Journal of Magnetic Resonance Imaging*, 42(2):407–420, 2015.
- [35] M. Lustig, D. Donoho, and J. M. Pauly. Sparse MRI: The application of compressed sensing for rapid MR imaging. *Magnetic Resonance in Medicine*, 58(6):1182–1195, 2007.
- [36] C. Prieto, M. Doneva, M. Usman, M. Henningsson, G. Greil, T. Schaeffter, and R. M. Botnar. Highly efficient respiratory motion compensated free-breathing coronary MRA using golden-step Cartesian acquisition. *Journal of Magnetic Resonance Imaging*, 41(3):738–746, 2015.
- [37] K. P. Pruessmann, M. Weiger, M. B. Scheidegger, and P. Boesiger. SENSE: Sensitivity encoding for fast MRI. *Magnetic Resonance in Medicine*, 42(5):952–962, 1999.
- [38] M. A. Griswold, P. M. Jakob, R. M. Heidemann, M. Nittka, V. Jellus, J. Wang, B. Kiefer, and A. Haase. Generalized autocalibrating partially parallel acquisitions (GRAPPA). *Magnetic Resonance in Medicine*, 47(6):1202–1210, 2002.
- [39] P. B. Roemer, W. A. Edelstein, C. E. Hayes, S. P. Souza, and O. M. Mueller. The NMR phased array. *Magnetic Resonance in Medicine*, 16(2):192–225, 1990.
- [40] C. D. Constantinides, E. Atalar, and E. R. McVeigh. Signal-to-noise measurements in magnitude images from NMR phased arrays. *Magnetic Resonance in Medicine*, 38(5):852–857, 1997.
- [41] M. Hutchinson and U. Raff. Fast MRI data acquisition using multiple detectors. *Magnetic Resonance in Medicine*, 6(1):87–91, 1988.

- [42] S. Foucart and H. Rauhut. *A mathematical introduction to compressive sensing*. Birkhäuser Basel, 2013.
- [43] E. J. Candes and M. B. Wakin. An introduction to compressive sampling. *IEEE Signal Processing Magazine*, 25:21–30, 2008.
- [44] R. Otazo, D. Kim, L. Axel, and D. K. Sodickson. Combination of compressed sensing and parallel imaging for highly accelerated first-pass cardiac perfusion MRI. *Magnetic Resonance in Medicine*, 64(3):767–776, 2010.
- [45] M. Lustig, J. M. Santos, and D. Donoho. k-t SPARSE: High frame rate dynamic MRI exploiting spatio-temporal sparsity. *Proceedings of the 13th ISMRM*, 50:2003–2003, 2006.
- [46] H. Jung and J. C. Ye. Motion estimated and compensated compressed sensing dynamic magnetic resonance imaging: What we can learn from video compression techniques. *International Journal of Imaging Systems and Technology*, 20(2):81–98, 2010.
- [47] M. S. Asif, L. Hamilton, M. Brummer, and J. Romberg. Motion-adaptive spatio-temporal regularization for accelerated dynamic MRI. *Magnetic Resonance in Medicine*, 70(3):800–812, 2013.
- [48] S. G. Lingala, E. DiBella, and M. Jacob. Deformation corrected compressed sensing (DC-CS): A novel framework for accelerated dynamic MRI. *IEEE Transactions on Medical Imaging*, 34(1):72–85, 2015.
- [49] M. Usman, D. Atkinson, E. Heathfield, G. Greil, T. Schaeffter, and C. Prieto. Whole left ventricular functional assessment from two minutes free breathing multi-slice CINE acquisition. *Physics in Medicine and Biology*, 60(7):N93–N107, 2015.

- [50] J. Royuela-del Val, L. Cordero-Grande, F. Simmross-Wattenberg, M. Martín-Fernández, and C. Alberola-López. Nonrigid groupwise registration for motion estimation and compensation in compressed sensing reconstruction of breath-hold cardiac CINE MRI. *Magnetic Resonance in Medicine*, 75(4):1525–1536, 2016.
- [51] J. Royuela-del Val, L. Cordero-Grande, Federico Simmross-Wattenberg, M. Martín-Fernández, and C. Alberola-López. Jacobian weighted temporal total variation for motion compensated compressed sensing reconstruction of dynamic MRI. *Magnetic Resonance in Medicine*, 77(3):1208–1215, 2017.
- [52] D. Rueckert, L. I. Sonoda, C. Hayes, D. L. G. Hill, M. O. Leach, and D. J. Hawkes. Nonrigid registration using free-form deformations: Application to breast MR images. *IEEE Transactions on Medical Imaging*, 18(8):712–721, 1999.
- [53] W. Crum, T. Hartkens, and D. Hill. Non-rigid image registration: Theory and practice. *The British Journal of Radiology*, 77 Spec No 2:S140–53, 2004.
- [54] W. Sun, W. J. Niessen, and S. Klein. Free-form deformation using lower-order B-spline for nonrigid image registration. In P. Golland, N. Hata, C. Barillot, J. Hornegger, and R. Howe, editors, *Medical Image Computing and Computer-Assisted Intervention – MICCAI 2014*, pages 194–201, Cham, 2014. Springer International Publishing.
- [55] C. De Boor. *A practical guide to splines*. Springer-Verlag New York, 1978.
- [56] B. Madore, G. H. Glover, and N. J. Pelc. Unaliasing by Fourier-encoding the overlaps using the temporal dimension (UNFOLD), applied to cardiac imaging and fMRI. *Magnetic Resonance in Medicine*, 42(5):813–828, 1999.

- [57] J. Tsao, P. Boesiger, and K. P. Pruessmann. k-t BLAST and k-t SENSE: Dynamic MRI with high frame rate exploiting spatiotemporal correlations. *Magnetic Resonance in Medicine*, 50(5):1031–1042, 2003.
- [58] F. Huang, J. Akao, S. Vijayakumar, G. R. Duensing, and M. Limkeman. k-t GRAPPA: A k-space implementation for dynamic MRI with high reduction factor. *Magnetic Resonance in Medicine*, 54(5):1172–1184, 2005.
- [59] H. Pedersen, S. Kozerke, S. Ringgaard, K. Nehrke, and W. Y. Kim. k-t PCA: Temporally constrained k-t BLAST reconstruction using principal component analysis. *Magnetic Resonance in Medicine*, 62(3):706–716, 2009.
- [60] M. S. Hansen, T. S. Sørensen, A. E. Arai, and P. Kellman. Retrospective reconstruction of high temporal resolution CINE images from real-time MRI using iterative motion correction. *Magnetic Resonance in Medicine*, 68(3):741–750, 2012.
- [61] M. Usman, D. Atkinson, F. Odille, C. Kolbitsch, G. Vaillant, T. Schaeffter, P. G. Batchelor, and C. Prieto. Motion corrected compressed sensing for free-breathing dynamic cardiac MRI. *Magnetic Resonance in Medicine*, 70(2):504–516, 2013.
- [62] C. Buerger, T. Schaeffter, and A.P. King. Hierarchical adaptive local affine registration for fast and robust respiratory motion estimation. *Medical Image Analysis*, 15(4):551–564, 2011.
- [63] H. Jung, K. Sung, K. S. Nayak, E. Y. Kim, and J. C. Ye. k-t FOCUSS: A general compressed sensing framework for high resolution dynamic MRI. *Magnetic Resonance in Medicine*, 61(1):103–116, 2009.
- [64] L. Wang, P. Clarysse, Z. Liu, B. Gao, W. Liu, P. Croisille, and P. Delachartre. A gradient-based optical-flow cardiac motion esti-

- mation method for CINE and tagged MR images. *Medical Image Analysis*, 57:136–148, 2019.
- [65] J. Royuela-del Val, M. Usman, L. Cordero-Grande, M. Martín-Fernández, F. Simmross-Wattenberg, C. Prieto, and C. Alberola-López. Whole-heart single breath-hold cardiac cine: A robust motion-compensated compressed sensing reconstruction method. In M. A. Zuluaga, K. Bhatia, B. Kainz, M. H. Moghari, and D. F. Pace, editors, *Reconstruction, Segmentation, and Analysis of Medical Images*, pages 58–69, Cham, 2017. Springer International Publishing.
- [66] R. Otazo, E. Candès, and D. K. Sodickson. Low-rank plus sparse matrix decomposition for accelerated dynamic MRI with separation of background and dynamic components. *Magnetic Resonance in Medicine*, 73(3):1125–1136, 2015.
- [67] A. Tolouee, J. Alirezaie, and P. Babyn. Nonrigid motion compensation in compressed sensing reconstruction of cardiac CINE MRI. *Magnetic Resonance Imaging*, 46:114–120, 2018.
- [68] F. Najeeb, M. Usman, I. Aslam, S. A. Qazi, and H. Omer. Respiratory motion-corrected, compressively sampled dynamic MR image reconstruction by exploiting multiple sparsity constraints and phase correlation-based data binning. *Magnetic Resonance Materials in Physics, Biology and Medicine*, 33(3):411–419, 2020.
- [69] T. Vercauteren, X. Pennec, A. Perchant, and N. Ayache. Diffeomorphic demons: Efficient non-parametric image registration. *NeuroImage*, 45(1, Supplement 1):S61–S72, 2009.
- [70] D. J. Kroon and C. H. Slump. MRI Modality transformation in demon registration. In *IEEE International Symposium on Biomedical Imaging: From Nano to Macro*, pages 963–966, 2009.

- [71] J. P. Thirion. Image matching as a diffusion process: An analogy with Maxwell's demons. *Medical Image Analysis*, 2(3):243–260, 1998.
- [72] F. Liu, D. Li, X. Jin, W. Qiu, Q. Xia, and B. Sun. Dynamic cardiac MRI reconstruction using motion aligned locally low rank tensor (MALLRT). *Magnetic Resonance Imaging*, 66:104–115, 2020.
- [73] L. Cayton. Algorithms for manifold learning. Technical Report No CS2008-0923, University of California at San Diego, 2005.
- [74] S. Poddar and M. Jacob. Dynamic MRI using smoothness regularization on manifolds (SToRM). *IEEE Transactions on Medical Imaging*, 35(4):1106–1115, 2015.
- [75] G. N. Shetty, K. Slavakis, U. Nakarmi, G. Scutari, and L. Ying. Kernel bi-Linear modeling for reconstructing data on manifolds: The dynamic-MRI case. In *28th European Signal Processing Conference*, pages 1482–1486, 2020.
- [76] S. Abdullah, O. Arif, M. Bilal Arif, and T. Mahmood. MRI reconstruction from sparse k-space data using low dimensional manifold model. *IEEE Access*, 7:88072–88081, 2019.
- [77] Z. Chen, C. Huang, and S. Lin. A new sparse representation framework for compressed sensing MRI. *Knowledge-Based Systems*, 188:104969, 2020.
- [78] L. Feng, R. Grimm, K. T. Block, H. Chandarana, S. Kim, J. Xu, L. Axel, D. K. Sodickson, and R. Otazo. Golden-angle radial sparse parallel MRI: Combination of compressed sensing, parallel imaging, and golden-angle radial sampling for fast and flexible dynamic volumetric MRI. *Magnetic Resonance in Medicine*, 72(3):707–717, 2014.

- [79] L. Feng, L. Axel, H. Chandarana, K. T. Block, D. K. Sodickson, and R. Otazo. XD-GRASP: Golden-angle radial MRI with reconstruction of extra motion-state dimensions using compressed sensing. *Magnetic Resonance in Medicine*, 75(2):775–788, 2016.
- [80] M. Usman, B. Ruijsink, M. S. Nazir, G. Cruz, and C. Prieto. Free breathing whole-heart 3D CINE MRI with self-gated Cartesian trajectory. *Magnetic Resonance Imaging*, 38:129–137, 2017.
- [81] S. Wundrak, J. Paul, J. Ulrici, E. Hell, M. A. Geibel, P. Bernhardt, W. Rottbauer, and V. Rasche. Golden ratio sparse MRI using tiny golden angles. *Magnetic Resonance in Medicine*, 75(6):2372–2378, 2016.
- [82] J. Schlemper, J. Caballero, J. V. Hajnal, A. N. Price, and D. Rueckert. A deep cascade of convolutional neural networks for dynamic MR image reconstruction. *IEEE Transactions on Medical Imaging*, 37(2):491–503, 2018.
- [83] H. K. Aggarwal, M. P. Mani, and M. Jacob. MoDL: Model-based deep learning architecture for inverse problems. *IEEE Transactions on Medical Imaging*, 38(2):394–405, 2019.
- [84] C. Qin, J. Schlemper, J. Caballero, A. N. Price, J. V. Hajnal, and D. Rueckert. Convolutional recurrent neural networks for dynamic MR Image reconstruction. *IEEE Transactions on Medical Imaging*, 38(1):280–290, 2019.
- [85] G. Yang, S. Yu, H. Dong, G. Slabaugh, P. L. Dragotti, X. Ye, F. Liu, S. Arridge, J. Keegan, Y. Guo, and D. Firmin. DAGAN: Deep de-aliasing generative adversarial networks for fast compressed sensing MRI Reconstruction. *IEEE Transactions on Medical Imaging*, 37(6):1310–1321, 2018.

- [86] O. Ronneberger, P. Fischer, and T. Brox. U-net: Convolutional networks for biomedical image segmentation.
- [87] R. M. Menchón-Lara, F. Simmross-Wattenberg, P. Casaseca-de-la Higuera, M. Martín-Fernández, and C. Alberola-López. Reconstruction techniques for cardiac CINE MRI. *Insights into Imaging*, 10(1):1–16, 2019.
- [88] U. Gamper, P. Boesiger, and S. Kozerke. Compressed sensing in dynamic MRI. *Magnetic resonance in medicine*, 59:365–73, 2008.
- [89] P. G. Batchelor, D. Atkinson, P. Irarrazaval, D. L. G. Hill, J. Hajnal, and D. Larkman. Matrix description of general motion correction applied to multishot images. *Magnetic Resonance in Medicine*, 54(5):1273–1280, 2005.
- [90] L. Cordero-Grande, R. P. Teixeira, E. Hughes, J. Hutter, A. Price, and J. Hajnal. Sensitivity encoding for aligned multishot magnetic resonance reconstruction. *IEEE Transactions on Computational Imaging*, 2(3):266–280, 2016.
- [91] M. Polfliet, S. Klein, W. Huizinga, M. M Paulides, W. J. Niessen, and J. Vandemeulebroucke. Intrasubject multimodal groupwise registration with the conditional template entropy. *Medical Image Analysis*, 46:15–25, 2018.
- [92] S. Becker, J. Bobin, and E. J. Candès. NESTA: A fast and accurate first-order method for sparse recovery. *SIAM Journal on Imaging Sciences*, 4(1):1–39, 2011.
- [93] J. Nocedal and S. J. Wright. *Numerical Optimization*. Springer, New York, NY, USA, 1999.

- [94] P. J. Beatty, D. G. Nishimura, and J. M. Pauly. Rapid gridding reconstruction with a minimal oversampling ratio. *IEEE Transactions on Medical Imaging*, 24(6):799–808, 2005.
- [95] F. Knoll, A. Schwarzl, C. Diwoky, and D. K. Sodickson. gpuNUFFT: An open source GPU library for 3D regridding with direct Matlab interface. In *International Society for Magnetic Resonance in Medicine*, page 4297, 2014.
- [96] G. Cruz, D. Atkinson, C. Buerger, T. Schaeffter, and C. Prieto. Accelerated motion corrected three-dimensional abdominal MRI using total variation regularized SENSE reconstruction. *Magnetic Resonance in Medicine*, 75(4):1484–1498, 2016.
- [97] T. Hastie, R. Tibshirani, and J. Friedman. *The elements of statistical learning*, volume 2. Springer New York Inc., New York, NY, USA, 2001.
- [98] Z. Wang, A. C. Bovik, H. R. Sheikh, and E. P. Simoncelli. Image quality assessment: From error visibility to structural similarity. *IEEE Transactions on Image Processing*, 13(4):600–612, 2004.
- [99] The Khronos Group Inc., OpenCL Overview, (<https://www.khronos.org/opencl>).
- [100] F. Simmross-Wattenberg, M. Rodríguez-Cayetano, J. Royuela-del Val, E. Martín-González, E. Moya-Sáez, M. Martín-Fernández, and C. Alberola-López. Opencliper: an opencl-based c++ framework for overhead-reduced medical image processing and reconstruction on heterogeneous devices. *IEEE Journal of Biomedical and Health Informatics*, 23(4):1702–1709, 2019.
- [101] E. Martín-González, E. Moya-Sáez, R. M. Menchón-Lara, J. Royuela-del Val, C. Palencia-de Lara, M. Rodríguez-Cayetano, F. Simmross-

- Wattenberg, and C. Alberola-López. A clinically viable vendor-independent and device-agnostic solution for accelerated cardiac MRI reconstruction. *Computer Methods and Programs in Biomedicine*, 207:106143, 2021.
- [102] B. Yaman, S. A. H. Hosseini, S. Moeller, J. Ellermann, K. Uğurbil, and M. Akçakaya. Self-supervised learning of physics-guided reconstruction neural networks without fully sampled reference data. *Magnetic Resonance in Medicine*, 84(6):3172–3191, 2020.
- [103] J. Liu, Y. Sun, C. Eldeniz, W. Gan, H. An, and U. S. Kamilov. RARE: image reconstruction using deep priors learned without groundtruth. *IEEE Journal of Selected Topics in Signal Processing*, 14(6):1088–1099, 2020.
- [104] E. Martín-González, T. Sevilla, A. Revilla-Orodea, P. Casaseca-de-la Higuera, and C. Alberola-López. Groupwise non-rigid registration with deep learning: an affordable solution applied to 2D cardiac CINE MRI reconstruction. *Entropy*, 22(6), 2020.
- [105] B. Adcock, A. Hansen, B. Roman, and G. Teschke. Generalized sampling: Stable reconstructions, inverse problems and compressed sensing over the continuum. 182:187–279, 2014.
- [106] R. M. Menchón-Lara, J. Royuela-del Val, F. Simmross-Wattenberg, P. Casaseca-de-la Higuera, M. Martín-Fernández, and C. Alberola-López. Fast 4D elastic group-wise image registration. Convolutional interpolation revisited. *Computer Methods and Programs in Biomedicine*, 200:105812, 2020.
- [107] H. J. Lamb, L. Van Schinkel, E. Kroner, P. J. van den Boogaard, M. J. Versluis, A. de Roos, A. Webb, and H. M. J. Siebelink. 7T clinical cardiovascular MR imaging: Initial experience. *Journal of Cardiovascular Magnetic Resonance*, 14(1):234, 2012.

-
- [108] M. Usman, D. Atkinson, C. Kolbitsch, T. Schaeffter, and C. Prieto. Manifold learning based ECG-free free-breathing cardiac CINE MRI. *Journal of Magnetic Resonance Imaging*, 41(6):1521–1527, 2015.
- [109] J. W. Krug, G. Rose, D. Stucht, G. Clifford, and J. Oster. Limitations of VCG based gating methods in ultra high field cardiac MRI. *Journal of Cardiovascular Magnetic Resonance*, 15(1):W19, 2013.



Universidad de Valladolid